PSFC/RR-09-9 **DOE/ET-54512-367**

Turbulence and Transport Studies with Phase Contrast Imaging in the Alcator C-Mod Tokamak and Comparisons with Gyrokinetic Simulations

Lin, L.

June 2009

Plasma Science and Fusion Center
Massachusetts Institute of Technology
Cambridge MA 02139 USA

This work was supported by the U.S. Department of Energy, Grant No. DE-FG02-94ER54235-APTE.

Turbulence and Transport Studies with Phase Contrast Imaging in the Alcator C-Mod Tokamak and Comparisons with Gyrokinetic Simulations

by

Liang Lin

B.S. (2002), Department of Modern Physics
University of Science and Technology of China

Submitted to the Department of Physics
in partial fulfillment of the requirements for the degree of

Doctor of Philosophy

at the

MASSACHUSETTS INSTITUTE OF TECHNOLOGY

June 2009

Author……………………………………………………………………………..
Department of Physics
March 9, 2009

Certified by…………………………………………………………………………..
Miklos Porkolab
Professor of Physics
Thesis Supervisor

Accepted by…………………………………………………………………...........
Thomas J. Greytak
Professor of Physics, Associate Department Head for Education

Turbulence and Transport Studies with Phase Contrast Imaging in the Alcator C-Mod Tokamak and Comparisons with Gyrokinetic Simulations

by

Liang Lin

Submitted to the Department of Physics
on March 9, 2009, in partial fulfillment of the
requirements for the degree of

Doctor of Philosophy

Abstract

An upgraded phase contrast imaging (PCI) diagnostic is used to study turbulence and transport in Alcator C-Mod. The upgraded PCI system is capable of measuring density fluctuations with high temporal (2 kHz-5 MHz) and wavenumber (0.5-55 cm^{-1}) resolution. An upgrade of the system has enabled PCI to localize the short wavelength turbulence in the electron temperature gradient (ETG) range and resolve the direction of propagation (i.e., electron vs. ion diamagnetic direction) of the longer wavelength turbulence in the ion temperature gradient (ITG) and trapped electron mode (TEM) range. Nonlinear GYRO simulations have also been performed and the predicted fluctuation is compared against experimental measurements through a synthetic PCI diagnostic method. Both L-Mode and H-Mode plasmas are examined through these numerical and experimental methods.

The L-Mode experiments were carried out over the range of densities covering the "neo-Alcator" (linear confinement time scaling with density, electron transport dominates) to the "saturated ohmic" regime. The key role played by the ITG turbulence has been verified. In the saturated ohmic regime, the simulated ion and electron thermal diffusivities also agree with experiments after varying the ion temperature gradient within experimental uncertainty. However, in the linear ohmic regime, GYRO does not agree well with experiments, showing significantly larger ion thermal transport and smaller electron thermal transport. Our study shows that although the short wavelength turbulence in the ETG range is unstable in the linear ohmic regime, the nonlinear simulation with $k_\theta\rho_s$ up to 4 does not raise the electron thermal diffusivity to the experimental level, where k_θ is the poloidal wavenumber and ρ_s is the ion-sound Larmor radius.

The H-Mode studies focus on plasmas before and during internal transport barrier formation in an enhanced D_α H-Mode plasma. The simulated fluctuations from GYRO agree with experimental measurements in the ITG regime. GYRO also shows good agreement in transport predictions with experimental measurements after reducing the ion temperature gradient (~15%) and adding E×B shear suppression, all within the experimental uncertainty.

Thesis Supervisor: Miklos Porkolab
Title: Professor of Physics

Acknowledgments

First and foremost, I am in a great debt to my thesis supervisor, Prof. Miklos Porkolab, for inspiring me with his foresight, physics intuition, and integrity, for his encouragement and guidance throughout of all phase of this thesis work, and for his kind supervision during my years at MIT.

Many teachers in plasma physics at MIT have inspired me, especially Profs. Ian Hutchison, Ron Parker, Jeffery Freiberg, Kim Molvig, and Dr. Peter Catto. Special thanks to my thesis readers, Profs. Bruno Coppi and Jan Egedal for many useful comments and suggestions.

I would like to thank Dr. Chris Rost for providing the synthetic diagnostic analysis package. Many thanks go to Dr. Darin Ernst for the tutorial on the GS2 code and Dr. David Mikkelsen at PPPL for the help with the GYRO code. Thanks are also due to the developers of the GYRO code, Drs. Jeff Candy and Ron Waltz at General Atomics, for enlightening discussions and help with the GYRO simulations. I also wish to thank Mr. Ted Baker and Drs. Darin Ernst and John Wright for implementing and maintaining the Loki cluster which is supported by the US SCIDAC theory program.

I want to thank Dr. Martin Greenwald for his support on the dedicated run days and the tutorial on running the TRANSP code. I want to thank Drs. Steve Wukitch and Yijun Lin for enlightening discussions in many aspects in plasma physics and their help during my early days at MIT. I want to thank Dr. Catherine Fiore for her support in the studies of the internal transport barriers. I want to thank Dr. Earl Marmar, as the head of Alcator C-Mod, providing financial support for my thesis research. I also want to thank many other research scientists in the Alcator C-Mod group for their contributions and support: Drs. Paul Bonoli, Bob Granetz, Amanda Hubbard, Jerry Hughes, John Rice, Joe Snipe, Jim Terry, Brian LaBombard, Bruce Lipschultz, and Steve Wolfe.

I am grateful to the hard-working engineers and technicians in the Alcator C-Mod group and their help in hardware, software, and electronics, especially to Joe Bosco, Dave Bellofatto, Willy

Burke, Ed Fitzgerald, Tom Fredian, Rick Murray, Yuri Rokhman, Bill Parkin, Josh Stillerman, and Tom Toland.

I want to thank Eric Edlund for six-year enjoyable and fruitful collaboration on the phase contrast imaging project. I also want to thank Brock Bose of many interesting discussions on gyrokinetic theory and the GYRO code. I am also grateful to all current and former graduate students at the Plasmas Science and Fusion Center: Alexander Boxer, Arturo Dominguez, James Dorris, Marco Ferrara, Will Fox, Jinseok Ko, John Liptac, Yunxing Ma, Ken Marr, Rachael McDermott, Alex Parisot, Matt Reinke, Andrea Schmidt, Noah Smick, Vincent Tang, Naoto Tsujii, Balint Veto, Greg Wallace, Peng Xu, Jing Zhou, and Kirill Zhurovich.

And finally, I extend personal thanks to my parents for their support, encouragement, and understanding.

This research utilized parallel computational clusters at MIT Plasma Science and Fusion Center (Loki) and Princeton Plasma Physics Laboratory (Kestrel). This work is supported by U. S. DOE under DE-FG02-94-ER54235 and DE-FC02-99-ER54512.

Contents

Chapter 1

Introduction

1.1 Fusion: Energy of Our Future[1]

Nuclear fusion has potential advantages as a safe, sustainable, and environmentally attractive source of energy. It has long been seen as the ultimate energy source of the future. A number of reactions are possible fusion candidates:

$$\mathrm{D{+}T} \rightarrow \mathrm{He}^4\left(3.52\ \mathrm{MeV}\right) + \mathrm{n}\left(14.06\ \mathrm{MeV}\right), \tag{1.1}$$

$$\mathrm{D{+}D} \rightarrow \mathrm{T}\left(1.01\ \mathrm{MeV}\right) + \mathrm{H}^1\left(3.03\ \mathrm{MeV}\right), \tag{1.2}$$

$$\mathrm{D{+}D} \rightarrow \mathrm{He}^3\left(0.82\ \mathrm{MeV}\right) + \mathrm{n}\left(2.45\ \mathrm{MeV}\right), \tag{1.3}$$

$$\mathrm{D{+}He}^3 \rightarrow \mathrm{He}^4\left(3.67\ \mathrm{MeV}\right) + \mathrm{p}\left(14.67\ \mathrm{MeV}\right), \tag{1.4}$$

where D and T stand for two hydrogen isotopes: deuterium and tritium. By far, the D-T reaction is the most favorable for the near term development in fusion, because it has the largest cross section $<\sigma>$ and reaction rate factor $<\sigma \mathrm{v}>$ at a relatively lower temperature ($\sim 10\ \mathrm{keV}$, about 100 million degree K). In the D-T reaction, the nuclei of deuterium and tritium to produce an alpha particle He and a neutron n. This nuclear reaction happens only when the distance between the two nuclei is in the order of the strong interaction scale (10^{-14} m). However, the two nuclei, both having positive charges, tend to repel rather than attract each other. Consequently, a tremendous amount of energy is required to bring the two charged nuclei close enough for fusion processes. For this reason, D-T fusion reactions generally occur at a temperature of at least 5 keV (about 50 million degree K). Under such conditions, both deuterium and tritium are completely ionized and the medium become plasma.

Since no known material can survive such extremely high temperatures. The confinement of hot plasmas has proven to be the greatest challenge in fusion research. One approach to containment is to use magnetic fields. Since fusion fuel is composed of electrically charged particles, it responds to electromagnetic force. In a magnetic field, charged particles are closely bonded to the field line. Therefore, with an appropriate configuration of magnetic fields in a chamber, the fusion fuel can remain trapped in a magnetic bottle. The magnetic fields keep the hot fuel from immediately striking the material walls of the chamber. The most promising magnetic confinement device in the reactor scale is “tokamak”.

1.2 Tokamak[2]

The word “tokamak” is derived from the Russian words, meaning “toroidal chamber” and “magnetic coil”. The generic design of a tokamak is shown in Fig. 1-1. In a tokamak, the principal magnetic field is the toroidal field, which is produced by current in the toroidal field coil. However, the toroidal field by itself does not confine a plasma. In order to achieve a steady confinement, an additional poloidal magnetic field is also necessary. In a tokamak, this poloidal field is produced by current in the plasma itself. This plasma current flows in the toroidal direction. The combination of the toroidal and poloidal magnetic fields results in magnetic field lines as shown in Fig. 1-1. They have helical trajectories around the torus. In present experiments, the plasma current is primarily driven by a toroidal electric field induced by a transformer action.

The transformer coil in the center of the torus serves as the primary winding, which drives a time-varying magnetic flux through the torus. While the plasma represents the second winding, the induced toroidal electric field will drive plasma current.

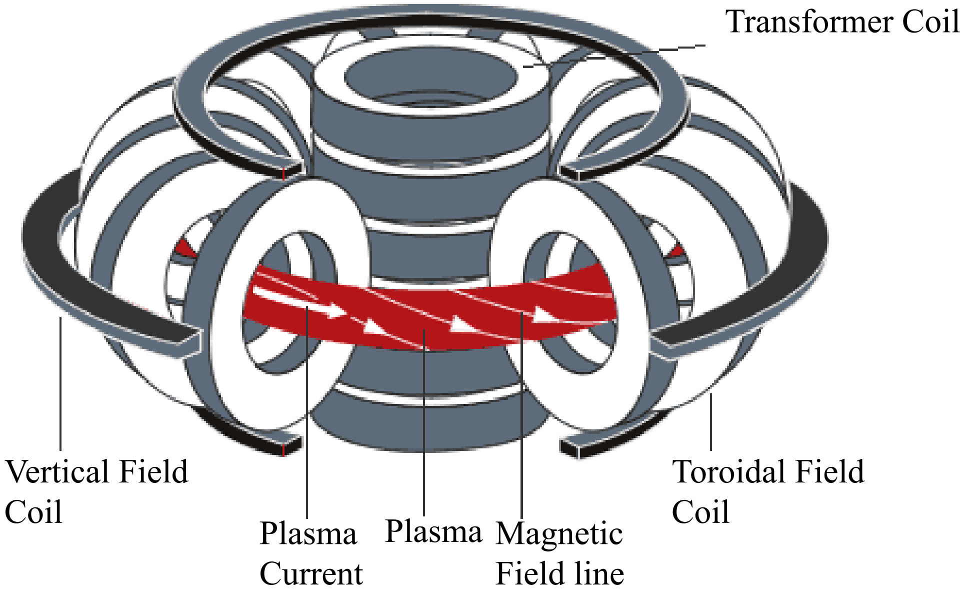

Figure 1-1: Schematic of principle components of a tokamak (figure from Ref.3)

The performance of a tokamak is typically evaluated by the Lawson criterion.[2] For the D-T reaction, the criterion for the "breakeven" condition, when the fusion power produced matches the external heating, takes the form of[2]

$$n_i \tau_E T_i \geq 8 \times 10^{20}\,\mathrm{m}^{-3}\mathrm{keVs}\ , \tag{1.5}$$

where n_i is the ion density, τ_E is the energy confinement time, and T_i is the ion temperature. The criterion for the "ignition" condition, under which the plasma can be maintained by fusion reactions without any external energy input, takes the form of[2]

$$n_i \tau_E T_i \geq 3 \times 10^{21}\,\mathrm{m}^{-3}\mathrm{keVs}\ . \tag{1.6}$$

As shown in Fig. 1-2, over the last ~40 years, fusion yield ($n_i \tau_E T_i$) has increased by about a factor of 10^7, which corresponds to a doubling time of about 1.5 years. To reach the ignition state, we have to improve the performance by another factor of 10^2, which is expected to be achieved in ITER[4]. The construction of ITER[4] has started, and the first plasma is expected by 2018. ITER should achieve a fusion gian of 10 and possibly demonstrate the scientific and technological feasibility of fusion energy.

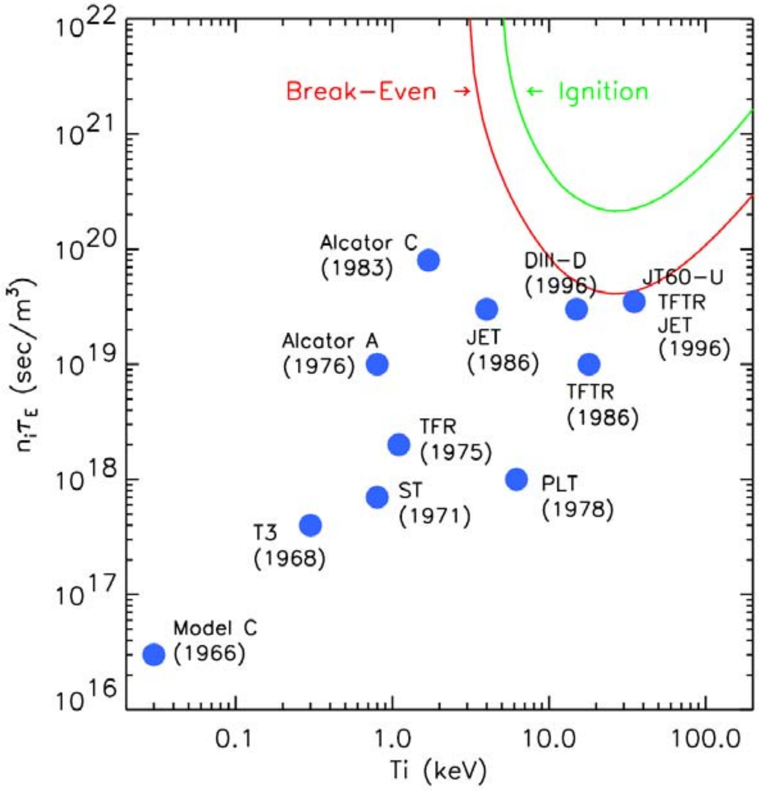

Figure 1-2: Performance of the Tokamaks around the world.

1.3 Motivation

In spite of the enormous progresses, many challenges remain to be solved to make fusion commercially available. One of the major challenges is to understand and control transport, which refers to the energy and particle losses of the plasma. The conventional transport study in fusion plasmas was limited to empirical analysis, which attempts to determine the relationships between the transport properties of plasma and characteristic operation parameters. These relationships have been used to predict the performance of new tokamaks, including ITER and DEMO[5], although they may not be reliable for reactor design and operation.[6]

Numerous transport models have been proposed, attempting to predict the transport in fusion plasmas. It has been known for many years that "classical transport" theory, based on particle collisions, under-predicts energy, momentum, and particle losses in a toroidal device.[7] The unexplained transport is generally referred to as the "anomalous" transport and has been generally attributed to nonlinear plasma turbulence evolved from the drift-wave instabilities. Recently, comprehensive theoretical models and simulations have been developed to the stage of being able to quantitatively predict turbulence and associated transport in the plasma core. However, detailed experimental comparisons and validations remain a challenge and in general are not available. [8,9]

In this thesis, a phase contrast imaging diagnostic (PCI) is used to measure the electron density fluctuations in the Alcator C-Mod tokamak.[10] Nonlinear gyrokinetic simulations have also been performed and the predicted fluctuations are directly and quantitatively compared against experimental measurements through a synthetic diagnostic method. In addition to turbulence, the simulated thermal diffusivities with gyrokinetics are also compared with the experimental measurements.

1.4 Alcator C-Mod

Alcator C-Mod[10] is a compact diverted tokamak that operates at high density and high magnetic field. It has been operating at MIT Plasma Science and Fusion Center since 1993. The major operating parameters are given in Table 1-1. The magnetic coils in Alcator C-Mod are fabricated of conventional copper and are cooled cryogenically, and require a great amount of power, which is provided by a flywheel alternator. Therefore, it only can operate in pulses. The frequency and length of pulses is determined by the necessary time to cool the coils and charge the flywheel alternator. The primary auxiliary heating in Alcator C-Mod is ion cyclotron range of frequencies (ICRF) waves launched by three antennas mounted on the wall.[11] Recently, a lower-hybrid (LH) microwave source was installed, which drives auxiliary current and provides a substantial amount of heating power.[11]

Table 1-1: Major operating parameters of Alcator C-Mod

Nominal major radius	0.66 m
Nominal minor radius	0.22 m
Toroidal magnetic field (B_T)	2.0-8.0 T
Input power (Ohmic + ICRF)	0.25-5 MW
Averaged electron density $\overline{n}_e$	0.24-6 [10^{20}m^{-3}]
Elongation κ	0.94-1.95
Triangularity	0.0-0.85

Based on the transport and confinement conditions, there are two operation regimes in Alcator C-Mod. The first regime is the low-confinement mode (L-Mode) due to its poor confinement. The second regime is the high-confinement mode (H-Mode), where both the particle and energy confinements are typically improved by a factor of 2 compared with the L-Mode plasma. Both L-Mode and H-Mode plasmas are studied in this thesis, where the L-Mode plasmas are purely ohmic heated and the H-mode plasmas are obtained with the auxiliary heating from the ICRF waves.

Turbulence and transport is probably the least understood area in the study of plasma physics. Plasma diagnostics play a crucial role in carrying out experimental studies. In Alcator C-Mod, a number of diagnostics are routinely available with respect to transport and turbulence studies. Table 1-2 lists the diagnostics used in this thesis.

Table 1-2: Key diagnostics for turbulence and transport studies

Diagnostic	**Measurements**
Thomson scattering (TS)	$T_e(r,t)$, $n_e(r,t)$
Electron Cyclotron Emission (ECE)	$T_e(r,t)$
X-Ray spectroscopy	$T_i(r,t)$, $E_r(r,t)$
Two-color interferometer (TCI)	$\int n_e dl$
Neutron detectors	T_{i0}, R_{DD}
Phase contrast imaging (PCI)	$\int \tilde{n}_e dl$

1.5 Thesis Outline

This thesis is divided into eight chapters:

- Chapter 1 introduces the basic conception of plasma fusion and magnetic confinement. The motivation of this thesis research is also described.
- Chapter 2 reviews the basics of transport and turbulence. First, the basics of transport and turbulence-drive transport are described. Then, a heuristic derivation of the drift waves in a simplified geometry is given. Last, the current status of transport and turbulence is briefly discussed.
- Chapter 3 starts with a brief introduction of the phase contrast imaging (PCI) technique. Then, the implementation of this technique on the Alcator C-Mod tokamak is reviewed. Finally, the localizing upgrade, which takes advantage of the magnetic pitch angle variation along the laser beam, is discussed.
- Chapter 4 starts with a brief introduction of gyrokinetics and its simulation. Then, the synthetic PCI method is described.
- Chapter 5 covers the studies of turbulence and transport in purely ohmic heated plasmas.
- Chapter 6 discusses the studies of turbulence and transport in H-Mode plasmas before and after the internal transport barrier (ITB) formation.
- Chapter 7 presents new features of the previously studied quasi-coherent (QC) mode observed by the upgraded PCI diagnostic.
- Chapter 8 summarizes the results of this thesis research. A few suggestions for further PCI hardware upgrades are given. A few possible research topics for future turbulence and transport studies in Alcator C-Mode are also proposed.

Chapter 2

Transport and Turbulence

A fundamental issue in fusion plasmas is to understand transport phenomena. It has been known for many years that the transport of energy and particles across the confining magnetic field of a toroidal device is larger than that predicted by the neoclassical transport theory[7], which is based on the classical binary-collision theory in combination with particle orbit properties in the toroidal magnetic geometry. The unexplained transport is generally referred to as the "anomalous" transport and has been generally attributed to nonlinear plasma turbulence, which can cause fluctuations in the particle velocities and positions, thereby causing particle and energy transport in plasmas. Turbulence, evolved from the drift-wave instabilities, has long been considered the mostly likely cause of anomalous transport in fusion plasmas.

Although the drift-wave turbulence is not as catastrophic as macroscopic magnetohydrodymic turbulence which can disrupt the plasma, it can significantly degrade the confinement performance by enhancing the diffusion of energy and particles across magnetic surfaces. Therefore, understanding the underlying drive mechanism of plasma microturbulence and how to suppress it is essential in developing more efficient fusion reactors.

This chapter is arranged as follows: Section 1 describes transport basics; Section 2 gives a heuristic description of the dispersion relation of drift-waves: ion temperature gradient (ITG) mode, trapped electron mode (TEM), and electron temperature gradient (ETG) mode; Section 3 reviews the current status of the studies of transport and turbulence in fusion plasmas.

2.1 Transport

2.1.1 Transport Basics

The simplest and most frequently used parameter to describe the transport phenomena is the global energy confinement time τ_E, which is calculated from the global energy conservation equation

$$\frac{\partial W}{\partial t} = P_{net} - \frac{W}{\tau_E}, \tag{2.1}$$

where P_{net} is the net heating power supplied to the plasma and W is the total stored energy. The heating power comes from ohmic heating and other auxiliary heating, such as neutral beam or RF heating, while the energy losses characterized by τ_E are mainly due to radiation, ionization, charge exchange with the neutral particles, and transport by collisions and turbulence. The total energy W includes the contributions from both electrons and ions and is obtained by integrating the energy density over the plasma volume

$$W = \frac{3}{2} \int \Sigma_j n_j T_j d^3 r, \tag{2.2}$$

where n_j is the density, T_j is the temperature, the subindex j indicates the particle species, and $d^3 r$ is the unit volume.

There are two methods to experimentally determine the energy confinement time τ_E. One method is by using the stationary phase of the plasma discharge where $\partial W / \partial t = 0$, so that τ_E in Eq. (2.1) can be expressed as

$$\tau_E = \frac{W}{P_{net}}. \tag{2.3}$$

The other method is using the transient phase in a discharge where the heating power is switched off, so that τ_E in Eq. (2.1) can be expressed as

$$\left| \tau_E = W \middle/ \frac{\partial W}{\partial t} \right|. \tag{2.4}$$

Because of the lack of a first-principles theory to deduce the energy confinement time, historically the experimental studies were limited to extract an empirical scaling law from the existing confinement data. In an empirical scaling, the confinement time τ_E is expressed in the form of a product of powers of various operational and engineering parameters, such as the plasma current and density. The scaling studies usually involve a huge database consisting of thousands of plasma discharges from multiple fusion devices. The obtained scaling expression allows for the prediction of the confinement performance to some extent. Different scaling expressions are found in different confinement regimes. As an example, the well established ITER89-P scaling for the L-Mode plasmas is shown as follows:[12]

$$\tau_E^{ITER89-P} = 0.048 \frac{I^{0.85} R^{1.2} a^{0.3} \kappa^{0.5} n^{0.1} B^{0.2} A^{0.5}}{P^{0.5}}, \tag{2.5}$$

where τ_E is the confinement time in sec, I is the plasma current in MA, R is the major radius in m, a is the minor radius in m, κ is the plasma elongation, n is the plasma density in

10^{20} m^{-3}, B is the magnetic field in T, A is the atomic mass of the ion species, and P is the applied power in MW. The scaling expressions in different types of H-Mode plasmas are established subsequently and take different forms. A summary of the scaling results in different confinement regimes can be found in Ref. 2.

2.1.2 Diffusion Coefficients

The physics mechanism determining the global confinement is described by the local particle and energy balance equations,[2]

$$\frac{\partial n_j}{\partial t} = -\frac{1}{r}\frac{\partial}{\partial r}\left(r\Gamma_j\right) + S_j, \tag{2.6}$$

$$\frac{3}{2}n_j\frac{\partial T_j}{\partial t} = -\frac{1}{r}\frac{\partial}{\partial r}\left(r\left(Q_j + \frac{5}{2}\Gamma_j T_j\right)\right) + P_j, \tag{2.7}$$

where Γ_j is the particle flux and Q_j is the particle (energy) flux. S_j and P_j represent the source, sink, and transfer terms for particles and energy, resepectively. All the dynamics of the transport process are contained in the flux terms, Γ_j and Q_j. Since there is no general form for the turbulent-driven transport, these fluxes have been parameterized by an analogy to the neoclassical theory where[2]

$$\Gamma_j = -D_j\frac{\partial n_j}{\partial r} + n_j\upsilon_j, \tag{2.8}$$

$$Q_j = -n_j\chi_j\frac{\partial T_j}{\partial r}. \tag{2.9}$$

Here D_j is the diffusion coefficient and χ_j is the thermal diffusivity, υ_j is a convection velocity and $n_j\upsilon_j$ represents the non-diffusive contribution to the particle transport. In general, it is not possible to directly measure the particle diffusivity D_j and thermal diffusivity χ_j. The particle and power balance equations are usually used to determine the experimental level of D_j and χ_j.

Transport theory aims to predict the local particle diffusivity D_j and the thermal diffusivity χ_j. A few transport theories have been developed. Classical transport theory deals with the transport due to binary collisions in a straight magnetic field. Neoclassical transport theory includes the complex magnetic geometry in fusion devices. However, the experimentally observed thermal diffusivity is at least an order of magnitude larger than that predicted by either the classical or the neoclassical transport theory.[7] This unaccounted anomalous transport has been generally attributed to nonlinear plasma turbulence.

2.1.3 Fluctuation-Driven Transport

Because of their collective behavior and electromagnetic properties, plasmas can support many different types of waves. Such plasma waves can grow unstable and modify the plasma in which they propagate. This is a nonlinear interaction, which leads to the development of turbulence. The resulting turbulence induces particle and energy transport. Both magnetic fluctuation $\tilde{\mathbf{B}}$ and electrostatic fluctuation $\tilde{\mathbf{E}} = -\nabla\tilde{\phi}$ contribute to transport. The total particle and energy fluxes are typically expressed as

$$\Gamma_j^f = \Gamma_j^{f,E} + \Gamma_j^{f,B}, \tag{2.10}$$

$$Q_j^f = Q_j^{f,E} + Q_j^{f,B}. \tag{2.11}$$

Here, the superscript f stands for fluctuation-driven fluxes. The superscripts E and B denote the flux driven by the electrostatic and magnetic fluctuation, respectively. The fluctuation-driven particle fluxes take the form of[13]

$$\Gamma_j^{f,E} = \frac{\left\langle \tilde{n}_j \tilde{E}_\theta \right\rangle}{B_\phi}, \tag{2.12}$$

$$\Gamma_j^{f,B} = \frac{\left\langle \tilde{j}_{//} \tilde{B}_r \right\rangle}{q_j B_\phi}, \tag{2.13}$$

where the $\tilde{E}_\theta$ is the fluctuating electric field along the poloidal direction, $\tilde{n}_j$ is the density fluctuation, $\tilde{j}_{//}$ is the current density along the magnetic field line, $\tilde{B}_r$ is the fluctuating magnetic field along the radial direction, q_j is the charge of the species j, B_ϕ is the equilibrium magnetic field along the toroidal direction, and $\left\langle \cdots \right\rangle$ denotes an ensemble average. Similarly, the fluctuation-driven energy fluxes take the form of

$$Q_j^{f,E} = \frac{3}{2} n_j \frac{\left\langle \tilde{E}_\theta \tilde{T}_j \right\rangle}{B_\phi} + \frac{3}{2} T_j \frac{\left\langle \tilde{E}_\theta \tilde{n}_j \right\rangle}{B_\phi}, \tag{2.14}$$

$$Q_j^{f,B} = g_j \frac{\tilde{B}_r}{B_\phi} \frac{\partial T_j}{\partial r}, \tag{2.15}$$

where $\tilde{T}_j$ is the temperature fluctuation and g_j is a parameter depending on the exact plasma parameters[14]. From Eqs. (2.12)-(2.15), the particle and energy transport cannot be deduced from the amplitude of the fluctuation quantities alone, since the correlations between different fluctuation quantities are also important.

If density fluctuation $\tilde{n}$, electron field fluctuation $\tilde{E}$, temperature fluctuation $\tilde{T}$, and their correlations could be measured simultaneously, the particle and energy flux driven by electrostatic fluctuations could be experimentally determined. One example is using the heavy ion beam probe (HIBP) [15], which can measure the density and potential fluctuations simultaneously. If the measurement can be performed at a few different points in space, the wavenumber of the measured fluctuation can also be extracted and the particle flux caused by the electrostatic turbulence can be ambiguously determined. For example, the frequency spectrum of the electrostatic particle flux $\Gamma^{f,E}$ in Eq. (2.12) can be rewritten as[16]

$$\Gamma^{f,E}(\omega) = \frac{k_\theta \tilde{n}_{rms}(\omega)\tilde{\phi}_{rms}(\omega)\left|\gamma_{n\phi}(\omega)\right|\sin\alpha_{\tilde{n}_j,\tilde{\phi}}}{B_\phi}, \tag{2.16}$$

where $\tilde{E}_\theta$ is expressed in terms of the potential fluctuation $\tilde{\phi}$, k_θ is the poloidal wavenumber of fluctuations, $\tilde{n}_{rms}$ and $\tilde{\phi}_{rms}$ is the root-mean-square (RMS) of $\tilde{n}$ and $\tilde{\phi}$. $\gamma_{n\phi}$ is the coherence between $\tilde{n}$ and $\tilde{\phi}$, and $\alpha_{\tilde{n}_j,\tilde{\phi}}$ is the phase between $\tilde{n}$ and $\tilde{\phi}$. According to Eq. (2.16), even if the fluctuation amplitude is large, the induced transport could be small if the coherence $\gamma_{n\phi}$ is small or $\sin\alpha_{\tilde{n}_j,\tilde{\phi}} \simeq 0$. Unfortunately, HIBP is not available at most fusion devices, which makes supplementary numerical simulations very essential.

2.2 Linear Theory of Drift Waves

It is generally believed that the responsible turbulence for anomalous transport is due to the lower-frequency drift-wave instabilities. These instabilities become unstable by tapping the free energy stored in temperature and/or density gradients. The history of drift-wave instability can be tracked back to the 1960s. The earliest studies of the ITG mode were performed in a simplified magnetic geometry. In the slab geometry, the ITG mode is essentially an ion acoustic wave driven unstable by the ion temperature gradient. Rudakov and Sagdeev derived the ITG mode in an unsheared slab[17], and Coppi examined the shear stabilization of the mode.[18] Porkolab derived the dispersion relation with arbitrary parallel phase velocities and temperature anisotropy included and also showed some experimental evidence of the ITG instabilities.[19-21] Later studies in more realistic toroidal geometry by Coppi[22] and Horton[23] showed that the ITG mode can be strongly destabilized by the ∇B and curvature drift. The destabilized mode is also known as toroidal ITG mode or η_i mode. Impurities can also affect the ITG mode. Coppi showed the strong destabilizing effect of inverted impurity profiles.[24] Thus, the radial variation of Z_{eff} is potentially important. Another important fact is the non-adiabatic electron response from the trapped electrons, which can drive another type of instability known as the trapped electron mode (TEM). The TEM in the short wavelength ($k_\theta \rho_i \gtrsim 1$) regime was found by Coppi and is generally referred to as the "ubiquitous mode". [22,25]

It is important to understand some of basic physics of the drift-wave instability through analyzing the dispersion relation in the simple slab geometry. This analysis reveals some important features of the threshold of instabilities.

2.2.1 Ion temperature Gradient Mode and Trapped Electron Mode

In this section, we give a simplified description of the process involved in excitation of the ITG and TEM turbulence. Our derivation follows a similar method as in Refs. [26-29]. Here, a one-dimensional plane geometry is assumed to simplify the derivation. The magnetic curvature drift is accounted for by introducing an effective gravity g in the x direction. The effect of the trapped electrons is included by splitting the electrons into two species: the circulating electrons and the trapped electrons.

In the derivation, all equilibrium quantities are assumed only as functions of x and the magnetic field is in the z direction. Low-β limit is considered, i.e.

$$\beta = \frac{n_i T_i + n_e T_e}{B^2 / 2\mu_0} << 1 . \tag{2.17}$$

Thus, the contribution from the magnetic fluctuations is ignored and the derivation is in an electrostatic approximation. The fluctuating electric field $\tilde{\mathbf{E}}$ is expressed in terms of the fluctuating potential $\tilde{\phi}$, i.e. $\tilde{\mathbf{E}} = -\nabla\tilde{\phi}$, where $\tilde{\phi}$ takes the form of

$$\tilde{\phi} = \tilde{\phi}(x)\exp\left(-i\omega t + ik_y y + ik_\parallel z\right), \tag{2.18}$$

where $k_\parallel \geq 2\pi / L$ and L is the relevant length scale of the system along the magnetic field. To further simplify the derivation, the local approximation is also assumed where the fluctuating potential $\tilde{\phi}$ is assumed to be localized around $x = x_0$, i.e. $d\ln\tilde{\phi}(x)/dx \ll k_y$, so that $\tilde{\phi}(x) \approx \tilde{\phi}(x_0)$. Here the characteristic frequency of the interested instabilities is specified in the range as follows,

$$\upsilon_{thi} \ll \upsilon_{the\parallel}^{T} \ll \frac{\omega}{k_\parallel} \ll \upsilon_{the}^{C}, \tag{2.19}$$

where υ_{thi} is the thermal velocity of ions, υ_{the}^{C} is the thermal velocity of circulating electrons, and $\upsilon_{the\parallel}^{T}$ is the effective parallel thermal velocity of the trapped electrons.

After combining the assumptions of $\omega \gg k_\parallel \upsilon_{thi}$ and $k_\parallel \geq 2\pi / L$, it can be seen that the considered mode frequency ω is also larger than the averaged ion transit frequency $<\omega_{ti}> \sim 2\pi\upsilon_{thi}/L$. This allows us to neglect the effect of trapped ions and to treat ions only as a single species. The perturbed ion density response can be solved from the Vlasov equation using the standard method of characteristics[30],

$$\frac{\tilde{n}_i}{n} = -\frac{e\tilde{\phi}}{T_i}\left\{\frac{\omega_{*i} - \omega_{Di}}{\omega} + \frac{\omega_{*i}(1+\eta_i)\omega_{Di}}{\omega^2} + \left(b_i - \frac{k_\parallel^2 \upsilon_{thi}^2}{\omega^2}\right)\left(1 - \frac{\omega_{*i}(1+\eta_i)}{\omega}\right)\right\}, \tag{2.20}$$

where $\omega_{*i} = (k_y T_i / eB)(d\ln n / dx)$ is the ion diamagnetic frequency, $\omega_{Di} = -k_y g_i / \Omega_i$ is the emulated magnetic drift frequency through the effective gravity $g_i \approx \upsilon_{thi}^2 / R$, Ω_i is the ion cyclotron frequency, $b_i = k_y^2 \upsilon_{thi}^2 / \Omega_i^2$ is the finite ion gyroradius parameter, and $\eta_i = d\ln T_i / d\ln n_i$.

For the electron species, the phase velocity $\omega / k_\|$ of considered instability lies between the thermal velocity of circulating electrons υ_{the}^C and the thermal velocity of the trapped electrons $\mathrm{v}_{the\|}^T$, i.e. $\upsilon_{the\|}^T \ll \omega / k_\| \ll \upsilon_{the}^C$. Thus, the non-adiabatic dynamics from the trapped electron cannot be neglected. This non-adiabatic dynamics is accounted for by simply expressing the perturbed electron density response $\tilde{n}_e$ in sum of the perturbed circulating electron density response $\tilde{n}_{eC}$ and the perturbed trapped electron density response $\tilde{n}_{eT}$, i.e.

$$\tilde{n}_e = \tilde{n}_{eC} + \tilde{n}_{eT}. \tag{2.21}$$

The circulating electrons simply have an adiabatic response since $\omega \ll k_\| \upsilon_{the}^C$. Thus, the perturbed circulating electron response takes the form of

$$\tilde{n}_{eC} = \frac{e\tilde{\phi}}{T_e} n_{eC}. \tag{2.22}$$

The trapped electrons are treated as a separate species with $\omega \gg k_\| \upsilon_{the\|}^T$. The perturbed density response of the trapped electrons, $\tilde{n}_{eT}$, is derived from the perturbed form of the mass conservation equation

$$\frac{\partial \tilde{n}_{eT}}{\partial t} + \nabla \cdot \left(n_{eT} \tilde{\mathbf{V}}_{eT} + \mathbf{V}_{eT} \tilde{n}_{eT} \right) = 0, \tag{2.23}$$

where $\mathbf{V}_{eT} = \left(-g_{eT} / \Omega_e \right) \hat{\mathbf{e}}_y$ is the drift velocity from the effective gravity $g_{eT} = \upsilon_{the}^2 / R$ and $\tilde{\mathbf{V}}_{eT} = \left(-ik_y \tilde{\phi} / B \right) \hat{\mathbf{e}}_x$ is from the $\tilde{\mathbf{E}} \times \mathbf{B}$ drift. Solving Eq. (2.23), we have

$$\frac{\tilde{n}_{eT}}{n_{eT}} = \frac{\omega_{*e}}{\omega - \omega_{De}} \frac{e\tilde{\phi}}{T_e}, \tag{2.24}$$

where $\omega_{*e} = -\left(T_e / T_i\right)\omega_{*i} = -(k_y T_e / eB)(d \ln n / dx)$ is the electron diamagnetic frequency and $\omega_{De} = -(T_i / T_e)\omega_{Di} = -k_y g_{eT} / \Omega_e$ is the curvature drift frequency for the trapped electrons.

The trapped electron response in Eq. (2.24) can be further improved with the approximate kinetic theory.[29, 31] The improved $\tilde{n}_{eT}$ takes the form of

$$\frac{\tilde{n}_{eT}}{n_{eT}} = \frac{e\tilde{\phi}}{T_e}\left(1 - \frac{2}{\sqrt{\pi}} \int_0^{\infty} \frac{\omega - \omega_{*e}\left[1 + \eta_e\left(E / T_e - 3/2\right)\right]}{\omega - \omega_{De} + i\nu_{eff}} \sqrt{E} e^{-E} dE\right), \tag{2.25}$$

where $\eta_e = d \ln T_e / d \ln n_e$, ν_{eff} is the trapped particle effective collision frequency, and the integral is from zero to infinity with respect to the particle energy $E = mv^2 / 2$. This improved response of the trapped electrons also includes the effect from collisions. When the effective collision frequency is comparable to the frequency of the considered perturbation, the collisions play an important role since the pitch angle scatterings can scatter the trapped particles into the passing domain and vice versa. The effect from collisions is included through the trapped particle effective collision frequency ν_{eff}. With the simplest model for the trapped particle effective collision frequency, we have $\nu_{eff} \approx \nu_e v_{the}^3 / \varepsilon v^3$ with its energy dependence included, where ν_e is the electron collisional frequency and ε is the inverse aspect ratio in a toroidal device.[32]

After obtaining the density response of the ions, the circulating electrons, and the trapped electrons, we can impose quasi-neutrality,

$$\tilde{n}_i \approx \tilde{n}_{eC} + \tilde{n}_{eT}, \tag{2.26}$$

to link Eqs. (2.20), (2.22), and (2.25) and obtain the dispersion relation as

$$
\begin{aligned}
&\frac{\omega_{*i}-\omega_{Di}}{\omega}+\frac{\omega_{*i}\left(1+\eta_i\right)\omega_{Di}}{\omega^2} \\
&\qquad +\left(b_i-\frac{k_\parallel^2\upsilon_{thi}^2}{\omega^2}\right)\left(1-\frac{\omega_{*i}\left(1+\eta_i\right)}{\omega}\right) \\
&\qquad\qquad +\frac{1}{\tau}-\frac{1}{\tau}\frac{n_{eT}}{n}\frac{2}{\sqrt{\pi}}\int_0^\infty\frac{\omega-\omega_{*e}\left[1+\eta_e\left(E/T_e-3/2\right)\right]}{\omega-\omega_{De}+i\nu_{eff}}\sqrt{E}e^{-E}dE=0
\end{aligned}
\quad , (2.27)
$$

where $\tau\equiv T_e/T_i$. The dispersion relation, Eq. (2.27), contains two resonant modes and one non-resonant fluid mode. We discuss them in detail.

1. Fluid ITG/TEM

Under the approximation of $\omega\gg\omega_{De}\gg\nu_{eff}$ and $b_i\gg k_\parallel^2\upsilon_{thi}^2/\omega^2$, the integrand in Eq. (2.27) can be expanded as

$$
\begin{aligned}
&\frac{\omega-\omega_{*e}\left[1+\eta_e\left(E/T_e-3/2\right)\right]}{\omega-\omega_{De}} \\
&\qquad\approx\left(1-\left[1+\eta_e\left(\frac{E}{T_e}-3/2\right)\right]\frac{\omega_{*e}}{\omega}\right)\left(1+\frac{\omega_{De}}{\omega}\right)
\end{aligned}
. \quad (2.28)
$$

The integration in Eq. (2.27) can be integrated analytically over the the particle energy E after the expansion in Eq. (2.28). After the integration, we have the dispersion relation,

$$
\begin{aligned}
&\frac{\omega_{*e}^2}{\omega^2}\left\{\frac{n_{eT}}{n_e}\frac{L_n}{R}\left(1+\eta_e\right)+b_i\left(1+\eta_i\right)+\left(1+\eta_i\right)\tau\frac{L_n}{R}\right\} \\
&\qquad+\frac{\omega_{*e}}{\omega}\left\{\frac{n_{eT}}{n_e}\left(1+\eta_e\right)+\frac{L_n}{R}\left(1-\frac{n_{eT}}{n_e}\right)+b_i\left(1+\eta_i\right)-1\right\}+\left\{1-\frac{n_{eT}}{n_e}+\frac{1}{\tau}b_i\right\}=0
\end{aligned}
. \quad (2.29)
$$

where $L_n = -(d\ln n/dx)^{-1}$ and $\omega \gg k_{\|}\upsilon_{thi}$ is assumed. Considering purely growing modes with $\omega_R = 0$, we have the growth rate as

$$\gamma \approx \omega_{*e}\sqrt{\frac{(L_n/R)(1+\eta_e)n_{eT}/n_e + b_i(1+\eta_i) + (1+\eta_i)(L_n/R)\tau}{1-n_{eT}/n_e+\tau b_i}}\,. \tag{2.30}$$

After neglecting the finite ion gyroradius effects $b_i \simeq 0$ and assuming $\tau = 1$, Eq. (2.30) can be further simplified as

$$\gamma \approx \omega_{*e}\sqrt{\frac{L_n}{R}}\sqrt{\frac{(1+\eta_e)n_{eT}/n_e+(1+\eta_i)}{1-n_{eT}/n_e}}\,. \tag{2.31}$$

This dispersion relation under the fluid approximation contains two branches. First, after ignoring the effect of the trapped electrons and assuming $\eta_i \gg 1$, Eq. (2.31) takes the form of

$$\gamma \approx \omega_{*e}\sqrt{\frac{L_n\eta_i}{R}}. \tag{2.32}$$

After substituting ω_{*e}, we have the growth rate of the ion temperature gradient (ITG) mode as

$$\gamma_{ITG} \sim k_y\rho_i\sqrt{\frac{\eta_i g_i}{L_n}}, \tag{2.33}$$

which is driven by the ion temperature gradient η_i and the magnetic curvature effect g_i. The second branch of Eq. (2.31) is the trapped electron mode with the growth rate,

$$\gamma_{TEM} \sim k_y\rho_i\sqrt{\frac{n_{eT}}{n}\frac{g_i}{L_n}}. \tag{2.34}$$

This TEM instability is also known as the "ubiquitous mode", which is destabilized by the ∇B drift in a toroidal geometry and was first found by Coppi[22].

2. Collisionless TEM

Under the approximation of $\omega \gg \omega_{Di}$, $\nu_{eff} \simeq 0$, $\omega \gg k_{\parallel} \mathrm{v}_{thi}$, $\nu_{eff} \simeq 0$, $b_i \simeq 0$, and $\tau = 1$, Eq. (2.27) can be simplified as

$$\frac{\omega_{*e}}{\omega} = 1 - \sqrt{2\varepsilon}\,\frac{2}{\sqrt{\pi}} \int_0^{\infty} \frac{\omega - \omega_{*e}\left[1 + \eta_e \left(E/T_e - 3/2\right)\right]}{\omega - \omega_{De}} \sqrt{E} e^{-E} dE\,. \tag{2.35}$$

Here the fraction of the trapped particles n_{eT}/n is approximated by $\sqrt{2\varepsilon}$ [33], where ε is the inverse aspect ratio in a toroidal device. The growth rate of the unstable mode can be solved analytically as

$$\gamma_{CTEM} \propto \omega_{*e} \sqrt{2\varepsilon}\, \eta_e \left(\frac{R}{L_n}\right)^{3/2} \left(\frac{R}{L_n} - \frac{3}{2}\right) \exp\left(-\frac{R}{L_n}\right). \tag{2.36}$$

This mode is known as collisionless trapped electron mode (CTEM), which is destabilized by the inverse electron-Landau damping and instability occurs when the density profile peaks, i.e., $R/L_n > 1.5$ according to the simplified derivation.

3. Dissipative TEM

In the collisional regime, assuming $\omega \gg \omega_{De}$, , $\omega \gg \omega_{Di}$, $\omega \gg k_{\parallel} \mathrm{v}_{thi}$, $\nu_{eff} \gg \omega$, $b_i \simeq 0$, and $\tau = 1$, Eq. (2.27) can be simplified as

$$\frac{\omega_{*e}}{\omega} = 1 - \sqrt{2\varepsilon}\,\frac{2}{\sqrt{\pi}} \int_0^{\infty} \frac{\omega - \omega_{*e}\left[1 + \eta_e \left(E/T_e - 3/2\right)\right]}{\omega + i\nu_{eff}} \sqrt{E} e^{-E} dE\,. \tag{2.37}$$

Here we have replaced ω_{*i} with $-\omega_{*e}/\tau$ and ignored the effect of curvature drift frequency ω_{Di} and ω_{De}. The integral term of Eq. (2.37) is assumed to be small. Thus, we have $\omega \simeq \omega_{*e}$. In the high collision-frequency regime, i.e. $\nu_{eff} \gg \omega$, the growth rate can be simplified as

$$\gamma = \sqrt{2\varepsilon}\omega_{*e}^2 \frac{2}{\sqrt{\pi}} \int_0^\infty \frac{e\left(E/T_e - 3/2\right)}{\nu_{eff}} \sqrt{E} e^{-E} dE . \tag{2.38}$$

Eq. (2.38) can integrated analytically and the growth rate takes the form of

$$\gamma_{DTEM} \sim \varepsilon^{3/2} \frac{\omega_{*e}^2}{\nu_e} \eta_e . \tag{2.39}$$

Here we have derived the growth rate of the dissipative trapped electron mode (DTEM)[34], which is driven by the combined effects of the collisional dissipation ν_e and the positive electron temperature gradient $\eta_e > 0$. However, as ν_e increases, γ_{DTEM} suffers collisional damping and decreases.

2.2.2 Electron Temperature Gradient Mode

The electron temperature gradient (ETG) mode is similar to the ITG mode with electrons and ions interchanged. The electron response under the fluid limit takes the form of[35]

$$\frac{\tilde{n}_e}{n} = \frac{e\tilde{\phi}}{T_e} \left\{ \frac{\omega_{*e} - \omega_{De}}{\omega} + \frac{\omega_{*e}\left(1+\eta_e\right)\omega_{De}}{\omega^2} + \left(b_e - \frac{k_\parallel^2 \upsilon_{the}^2}{\omega^2}\right)\left(1 - \frac{\omega_{*e}\left(1+\eta_e\right)}{\omega}\right) \right\} . \tag{2.40}$$

where $\omega_{*e} = -(k_y T_e / eB)(d \ln n / dx)$ is the electron diamagnetic frequency, $\omega_{De} = -k_y g_e / \Omega_e$ is the emulated magnetic drift frequency through the effective gravity $g_e \approx \upsilon_{the}^2 / R$, Ω_e is the electron cyclotron frequency, $b_e = k_y^2 \upsilon_{the}^2 / \Omega_e^2$ is the finite electron gyroradius parameter, and $\eta_e = d \ln T_e / d \ln n_e$. Equation (2.40) is similar to Eq. (2.20), but where the roles of the ions and electrons are reversed. Since $k_y\rho_e \sim 1$ for the ETG mode, $k_y\rho_i \gg 1$. Therefore, the ions simply have an adiabatic response, i.e.

$$\frac{\tilde{n}_i}{n} = -\frac{e\tilde{\phi}}{T_i} \tag{2.41}$$

After imposing quasi-neutrality ($\tilde{n}_i \simeq \tilde{n}_e$) to link Eqs. (2.40) and (2.41), the dispersion relation is obtained as

$$\frac{\omega_{*e}^2}{\omega^2}\left(1+\eta_e\right)\frac{L_n}{R} - \frac{\omega_{*e}}{\omega}\left(\frac{L_n}{R} - 1 + b_e\left(1+\eta_e\right)\right) + b_e + \tau = 0\,. \tag{2.42}$$

Here, $\omega \gg k_{\parallel}\upsilon_{the}$ is assumed. Considering the purely growing modes, we have the growth rate as

$$\gamma = \omega_{*e}\sqrt{\frac{1+\eta_e}{b_e+\tau}\frac{L_n}{R}}\,. \tag{2.43}$$

After neglecting the finite electron gyroradius effects $b_e \simeq 0$ and assuming $\tau = 1$ and $\eta_e \gg 1$, Eq. (2.43) can be further simplified as

$$\gamma = \omega_{*e}\sqrt{\eta_e\frac{L_n}{R}}\,. \tag{2.44}$$

After substituting ω_{*e}, we have the growth rate of the ion temperature gradient (ETG) mode as

$$\gamma_{ETG} = k_y\rho_e\sqrt{\eta_e\frac{g_e}{L_n}}\,. \tag{2.45}$$

Even though the ETG mode can have larger growth rates than the ITG mode ($\gamma_{ETG}/\gamma_{ITG} \sim \sqrt{m_i/m_e}$), its wavenumber is much larger than the ITG mode ($k_{ETG}/k_{ITG} \sim \sqrt{m_i/m_e}$). Using the mixing length estimate for the thermal diffusivity χ where $\chi \sim \gamma/k^2$,[2]

$$\frac{\chi_{ETG}^{(ML)}}{\chi_{ITG}^{(ML)}} \sim \frac{\gamma_{ETG}/k_{ETG}^2}{\gamma_{ITG}/k_{ITG}^2} \sim \sqrt{\frac{m_e}{m_i}} \sim \frac{1}{60}\,. \tag{2.46}$$

The thermal diffusivity caused by the ETG turbulence is expected to be much smaller (1/60) than that from the ITG turbulence. The reason why the ETG mode is believed to play a role in electron transport is that it may produce large scale eddies when one considers nonlinear interactions. Despite the relative small mixing length estimate, for large shear $\hat{s}$ and small normalized-β gradient α, radial ETG streamers have been observed by Jenko and Dorland in gyrokinetic simulations of ETG turbulence with adiabatic ions, giving experimentally relevant transport levels.[36] Because of the small scales of the ETG turbulence, the ions were treated adiabatically in the early simulations by Jenko and Dorland. Recent simulations of the ETG turbulence with kinetic ions, by Candy and Waltz, shows that 10-20% of the total electron transport can arise from the ETG scale turbulence where the ion-scale instabilities are not suppressed.[37] They also showed that if the ion-scale instabilities are suppressed, by removal of the ion free energy or by the presence of ExB shear suppression, this fraction can increase significantly. This result was also confirmed by Goerler and Jenko.[38] However, since most C-Mod plasmas we are considering have significant ITG drive, it seems unlikely that the ETG scale turbulence can significantly contribute the electron thermal transport. At present, the role of the ETG turbulence in the electron thermal transport under typical experimental conditions remains problematic expect in cases where strong ExB shear might stabilize the long-wavelength ITG/TEM modes.

2.2.3 Micro-Reconnecting Mode

The above derivation of the ETG mode is under the electrostatic approximation. Coppi and Crabtree found that the electron temperature gradient can drive a type of electromagnetic instability.[39, 40] This instability is named as the micro-reconnecting mode (MRM)[41] and does not involve electron gyroradius effect as the usual electrostatic ETG mode. The derivation was performed in a sheared slab geometry where the equilibrium magnetic field is

$$\mathbf{B} = B_0\left(\mathbf{e}_z + \frac{x}{L_s}\mathbf{e}_y\right). \tag{2.47}$$

The electromagnetic effect is considered by including the perturbed parallel magnetic vector potential $\tilde{A}_\parallel = \tilde{A}_\parallel(x)\exp(-i\omega t + ik_y y + ik_z z)$, since the perpendicular magnetic vector potential $\tilde{\mathbf{A}}_\perp$ is negligible in the low-β limit. With the addition of $\tilde{A}_\parallel$, the fluctuation electric field ($\tilde{\mathbf{E}}$) and the fluctuation magnetic electric field ($\tilde{\mathbf{B}}$) are $\tilde{\mathbf{E}} = -\nabla\tilde{\phi} - \partial\tilde{A}_\parallel/\partial t$ and $\tilde{\mathbf{B}}_\perp = \nabla\tilde{A}_\parallel \times \mathbf{B}/B$, respectively. In the fluid limit, where $\omega < \omega_{*Te}$ and $\omega^2 > k_\parallel^2 \upsilon_{the}^2$, the dispersion relation for MRM takes the forms of

$$\left[\omega^3\left(1+\frac{T_e}{T_i}\frac{\omega_{*e}}{\omega}\right) + k_\parallel^2 c_{se}^2 \omega_{*Te}\right] d_e^2\left(\frac{d^2}{dx^2} - k_y^2\right)\tilde{A}_\parallel \simeq -\omega^2\omega_{*Te}\left(1+\frac{T_e}{T_i}\frac{\omega_{*e}}{\omega}\right)\tilde{A}_\parallel, \tag{2.48}$$

where $\omega_{*Te} = -(k_y/eB)dT_e/dx$ is the frequency representing the mode driving factor, $\omega_{*e} = -(k_y T_e/eB)d\ln n/dx$ is the electron diamagnetic frequency, $c_{se} = (T_i/m_e)^{1/2}$ is the electron sound velocity, and $d_e \sim c/\omega_{pe}$ is the plasma skin depth. The detailed derivation of Eq. (2.48) can be found in Refs. 39 and 41. Coppi and Crabtree examined the fluid theory through numerical procedures and asymptotic analysis and found that, when the temperature gradient is larger than the density gradient, the modes satisfies $k_y d_e \gtrsim 1$ and the growth rate is[42]

$$\gamma \sim \frac{c_{se}}{L_s}\left(\frac{2k_y d_e}{\beta_e}\right)^{1/3}\left(\frac{T_i}{T_e}\right)^{1/3}\left(\frac{L_{Te}}{L_s}\right)^{2/3}. \tag{2.49}$$

In the quasi-linear limit, the relevant effective thermal diffusion (χ_{MRM}) of the MRM is[43]

$$\chi_{MRM} \sim \frac{d_e \rho_e \upsilon_{the}}{L_{Te}}. \tag{2.50}$$

Comparing χ_{MRM} with χ_{ETG} of the electrostatic ETG mode ($\chi_{ETG} \sim \rho_e^2 \upsilon_{the} / L_{Te}$) from the mixing length estimate

$$\frac{\chi_{MRM}}{\chi_{ETG}} \sim \frac{d_e}{\rho_e}. \tag{2.51}$$

When $d_e \gg \rho_e$, the MRM instability can cause much larger thermal transport than the electrostatic ETG mode. For typical C-Mod plasmas, $55 \gtrsim d_e / \rho_e \gtrsim 25$; thus, the MRM may play a more important role than the electrostatic ETG instability mode. We would also expect large density fluctuions in the wavenumber regime of $k_y d_e \gtrsim 1$.

In general, while the ITG turbulence is believed to be the primary drive for turbulent ion thermal transport in the core region of a tokamak, and the trapped electron mode explains part of the observed electron thermal transport, the search for additional drive mechanisms to explain electron thermal transport remains an area of active research. Both experimental and numerical approaches are important in understanding transport physics. Experimental measurements will provide direct validation of numerical codes, while numerical simulation will assist the understanding of experimental measurements.

2.3 Current Status of Transport and Turbulence Studies

To understand the underlying physics of transport driven by turbulence, many theories have been developed in the past fifty years. Gyrokinetics is one of the most comprehensive theories based on the first-principles and can quantitatively describe the nonlinear form of drift-wave turbulence.[72] Furthermore, recent advances in gyrokinetic code development with the advent of powerful high-performance computers allow for the "full physics" simulations to accurately and quantitatively predict turbulence and associated transport. A detailed description of gyrokinetics and its simulation is given in Chapter 4. To meet the validation requirement, the numerical codes must be tested against the experimental measurements at two levels: fluctuation dynamics and associated transport. Therefore, developing the advanced plasma diagnostics to characterize turbulence is essential. Various diagnostics have been developed to measure turbulence in fusion plasmas around the world. In Alcator C-Mod, a phase contrast imaging (PCI) diagnostic has been developed to directly measure electron density fluctuations.[56] A detailed description the PCI diagnostic and its implementation will be conducted in the next chapter.

Chapter 3

Phase Contrast Imaging Diagnostic

The phase contrast imaging (PCI) method was invented by the Dutch physicist Franz Zernike in the 1930s.[44,45] This method allows one to measure small phase shifts in light waves after passing through a dielectric type of media. Franz Zernike was awarded the Nobel Prize in physics in 1953. This method was mainly used in the field of biology and medicine.

In the 1980s Henri Weisen first employed the PCI method in fusion plasmas[46] to study turbulence and driven Alfvèn waves in the TCA tokamak[47]. Since then, the PCI method has been used on many plasma fusion devices, including the DIII-D tokamak at General Atomics[48] and the Alcator C-Mod tokamak at MIT[49] in the United States, the TCV tokamak in Switzerland[50], and the Large Helical Device (LHD) in Japan[51]. The investigated topics include plasma turbulence, MHD fluctuations, and externally launched radio-frequency waves.

In this chapter, we will discuss this imaging technique and its implementation on the Alcator C-Mod Tokamak. The remainder of this chapter is organized as follows: Section 3.1 reviews the basic principles of the PCI technique; Section 3.2 describes the PCI system in Alcator C-Mod; Section 3.3 discusses the localizing upgrade by taking advantage of the variation of the magnetic pitch angle. Finally, section 3.4 is a summary.

3.1 Phase Contrast Imaging

3.1.1 Principles of Phase Contrast Imaging

The interaction of electromagnetic waves with plasmas is essentially a scattering process, where the incident wave is scattered by a collection of charged particles. For most cases in plasmas, the scattering is from free electrons. Because of the collective behavior of the plasma, electrons interact with each other and the characteristic distance of this interaction is the Debye length

$$\lambda_D = \sqrt{\frac{\varepsilon_0 T_e}{e^2 n_e}} = 7.43\times 10^3 \sqrt{\frac{T_e}{n_e}}\ [\mathrm{m}], \tag{3.1}$$

where T_e is the electron temperature in eV and n_e is the electron density in m^{-3}, ε_0 is the dielectric constant. For C-Mod plasmas, typically $\lambda_D \sim 0.4 - 15\times 10^{-6}\ \mathrm{m}$.

Whether the collective behavior is important depends on the magnitude of $k\lambda_D$. Here k is the magnitude of the differential scattering wave-vector defined as $\mathbf{k} = \mathbf{k}_s - \mathbf{k}_i$, where $\mathbf{k}_s$ is the wave-vector of the scattered wave and the $\mathbf{k}_i$ is the wave-vector of the incident wave. When $k\lambda_D \gg 1$, the scattering only depends on the random motion of electrons and is known as incoherent scattering. When $k\lambda_D \ll 1$, the scattering also depends on the phase relations and spatial distributions of electrons, which is known as coherent scattering. The scattering process considered in the remainder of this thesis has $k\lambda_D \ll 1$, which belongs to the coherent scattering.

In the case of the coherent scattering, the plasma can be simply treated as a continuous medium characterized by its dielectric properties. When a laser beam is diffracted by the refractive perturbation, the resulted phase disturbance $\tilde{\Phi}$ takes the form of[52]

$$\tilde{\Phi} = k_0 \int (N-1)\, dl, \tag{3.2}$$

where k_0 is the wavenumber of the probing laser beam, $N=(1-\omega_{pe}^2/\omega_0^2)^{1/2}$ is the plasma refractive index, $\omega_{pe}=(n_e e^2/\varepsilon_0 m_e)^{1/2}$ is the plasma frequency, where $\omega_0 \simeq k_0 c$ is the radial frequency of the probing beam, c is the speed of light, m_e is the electron mass, e is the electron charge.

When $\omega_0 \gg \omega_{pe}$, the plasma refractive index can be expanded as

$$N \simeq 1-\frac{\omega_{pe}^2}{2\omega_0^2} \tag{3.3}$$

and Φ can be rewritten as

$$\Phi=-\lambda_0 r_e \int n_e dl\,, \tag{3.4}$$

where $\lambda_0 = 2\pi/k_0$ is the wavelength of the probing beam and $r_e = e^2/(4\pi\varepsilon_0 m_e c^2)$ $=2.8179\times10^{-15}$ m is the classical electron radius. Assuming a purely sinusoidal density fluctuation in the plasma,

$$n=n_0+\tilde{n}_e\cos(k_p x)\,, \tag{3.5}$$

where x is the propagating direction of the density fluctuation, assumed to be perpendicular to the beam propagating direction z, and k_p is the wavenumber of the density fluctuation. Both the phase and intensity of the beam will be modulated by this density fluctuation. As shown in Fig. 3-1, after passing through the plasma the laser beam is decomposed into three parts: the unscattered beam (red), and the left and the right scattered beams (blue) propagating at the scattering angle θ. Here the density fluctuation is assumed to be a thin phase object and the Bragg relation is satisfied, i.e.

$$\sin\frac{\theta}{2}=\pm\frac{k_p}{2k_0} \quad \text{or} \quad \theta \simeq \frac{k_p}{k_0}\,. \tag{3.6}$$

Just after passing through the density fluctuation, the wave field of the laser beam takes the form of

$$E = E_0\left(1 \text{-} \frac{\Delta^2}{2}\right) + E_0\frac{i\Delta}{2}e^{ik_p x} + E_0\frac{i\Delta}{2}e^{-ik_p x}\,, \tag{3.7}$$

where E_0 is the electric field of the incident waves, $\Delta = -\lambda_0 r_e \int \tilde{n}_e dl \ll 1$ is the phase variation introduced by the density fluctuation, the first term corresponds to the unscattered beam, and the second and third terms correspond to the scattered beams (left and right). The intensity of the laser beam is

$$I = \frac{\left|E^2\right|}{2\mu_0 c} \simeq I_0\left(1+\Delta^2\cos^2 k_p x\right), \tag{3.8}$$

where $I_0 = \mid E_0^2 \mid / 2\mu_0 c$ is the beam intensity before encountering the density fluctuation. The change of the beam intensity due the density fluctuation is only to the second order of Δ. Since $\Delta \ll 1$, this change in the beam intensity is difficult to measure.

Because of the different incident angles, the three beams will be focused on three individual spots and thus spatially separated on the focal plane after an imaging lens or parabolic mirror, as shown in Fig. 3-1. By placing a phase plate with a central groove on the focal plate after the parabolic mirror, the unscattered beam focused inside the groove travels an extra distance. Setting the groove depth to be $\lambda_0 / 8$ allows the phase plate to additionally phase shift only the electric field of the unscattered beam by $\pi / 2$. After this extra phase shift of the unscattered beam, the wave field of the laser beam takes the forms of

$$E_{PCI} = i \times E_0\left(1 \text{-} \frac{\Delta^2}{2}\right) + E_0\frac{i\Delta}{2}e^{ik_p x} + E_0\frac{i\Delta}{2}e^{-ik_p x}\,, \tag{3.9}$$

The unscattered beam is in phase with the scattered beams and the resulting beam intensity is

$$I_{PCI} \propto \frac{\left|E_{PCI}\right|^2}{2\mu_0 c} = I_0\left(1+2\Delta\cos k_p x\right). \tag{3.10}$$

The phase shift variations $\Delta = -\lambda_0 r_e \int \tilde{n}_e dl$ are linearly proportional to the beam intensity variations. The wave propagating pattern of the density fluctuation also remains in the beam intensity. In some sense, the beam intensity is a snapshot of the density wave propagating perpendicular to the beam. This beam intensity can be easily detected through a photovoltaic or photoconductive detector array. Assuming $\tilde{n}_e / n_e \sim 0.01$ and $\int dl \sim 0.1\ \text{m}$, $\Delta \sim 0.003\ \text{rad}$ for typical C-Mod plasmas with $n_e \sim 1\times10^{20}\ \text{m}^{-3}$.

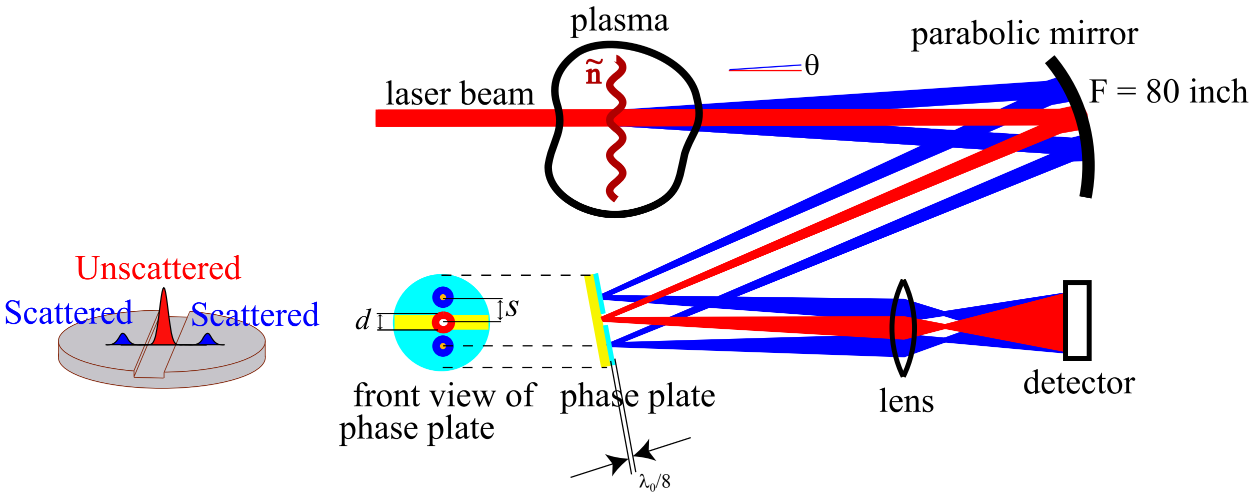

Figure 3-1: Principle of the PCI technique. In the diagram, the red beam corresponds to the unscattered beam, while the blue beams correspond to the scattered beams due to the density fluctuations.

3.1.2 System Response of Phase Contrast Imaging

The limit of the system response of PCI is mainly in the wavenumber space. To have proper phase contrast, the scattered beam must be focused outside the groove of the phase plate, while the unscattered beam must also be included inside the groove. The distance between the scattered beam spot and unscattered beam on the phase plate is

$$s = F_0 \frac{k_p}{k_0}, \tag{3.11}$$

where $F_0 = 2.03\ \mathrm{m}$ is the focal length of the parabolic mirror before the phase plate. The proper phase contrast requires s to be larger than the half of the groove width (d) on the phase plate

$$s > \frac{d}{2} \quad . \tag{3.12}$$

This requirement imposes a minimum detectable wavenumber,

$$k_{\min} = \frac{d}{2F_0} k_0 . \tag{3.13}$$

Phase plates with different groove widths ($d = 0.3, 0.4, 1.1, 2.7, 4.0\ \mathrm{mm}$) are available in the Alcator C-Mod PCI system, which gives different $k_{\min}$. In this thesis, the PCI measurements are obtained with the groove width $d = 0.3$ and 0.4 mm and the corresponding $k_{\min}$ is $0.44\ \mathrm{cm}^{-1}$ and $0.58\ \mathrm{cm}^{-1}$.

The limit of the maximum detectable wavenumber $k_{\max}$ from the physical apertures and optics sizes is above $60\ \mathrm{cm}^{-1}$ and out of concern in the C-Mod PCI system. Therefore, the maximum detectable wavenumber $k_{\max}$ is only set by the optical configuration and spacing of the detector elements, i.e. the Nyquist wavenumber[53].

With all these limits in the wavenumber space, the PCI technique is sensitive to the fluctuation spectra with finite $\mathbf{k}_\perp$ (perpendicular to the probe beam) and small $\mathbf{k}_\parallel$ (parallel to the probe beam). An example of wavenumber response is shown in Fig. 3-2. The decrease of system response at larger wavenumbers is caused by the finite area of the detector, since the sufficiently short wavelength signal will be averaged out.

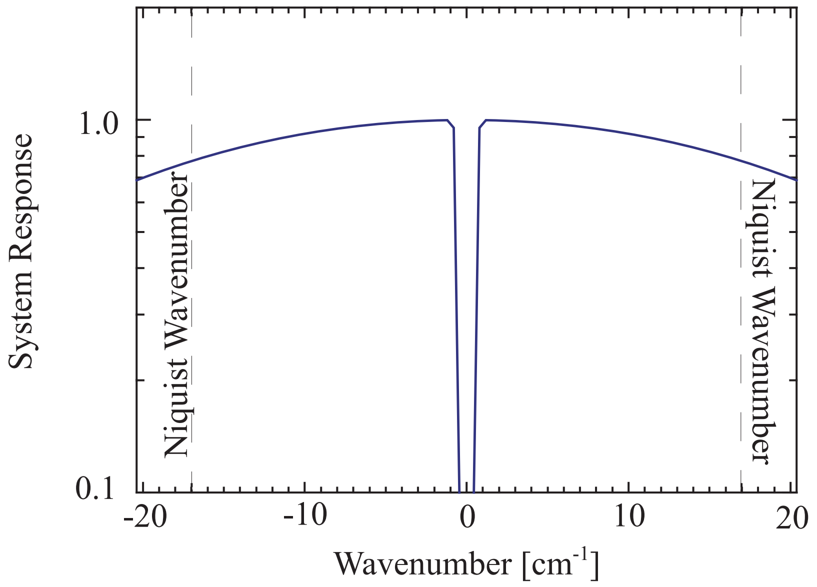

Figure 3-2: An example of wavenumber response of the PCI technique

3.2. PCI System in Alcator C-Mod

The PCI system in the Alcator C-Mod tokamak was first implemented in 1998 by Alexander Mazurenko[49] and was primarily used to study long wavelength ($k \leq 8\ \text{cm}^{-1}$) coherent fluctuations and radio-frequency (RF) waves[54 - 57]. To enhance the system performance in measuring broadband turbulence, a series of upgrades in optics and electronics have been carried out since 2003.

The geometry of the PCI diagnostic in Alcator C-Mod is shown in Fig. 3-3. The beam expansion and imaging optics are separated and located below and above the machine. Since neither of them is directly attached to the machine, the PCI system is not greatly sensitive to the mechanical vibrations during plasma pulses. Between the beam expansion and imaging optics, the collimated laser beams is steered with the upper and lower steering mirrors and vertically passes through the plasmas. In the remainder of this section, each component of the C-Mod PCI diagnostic will be described.

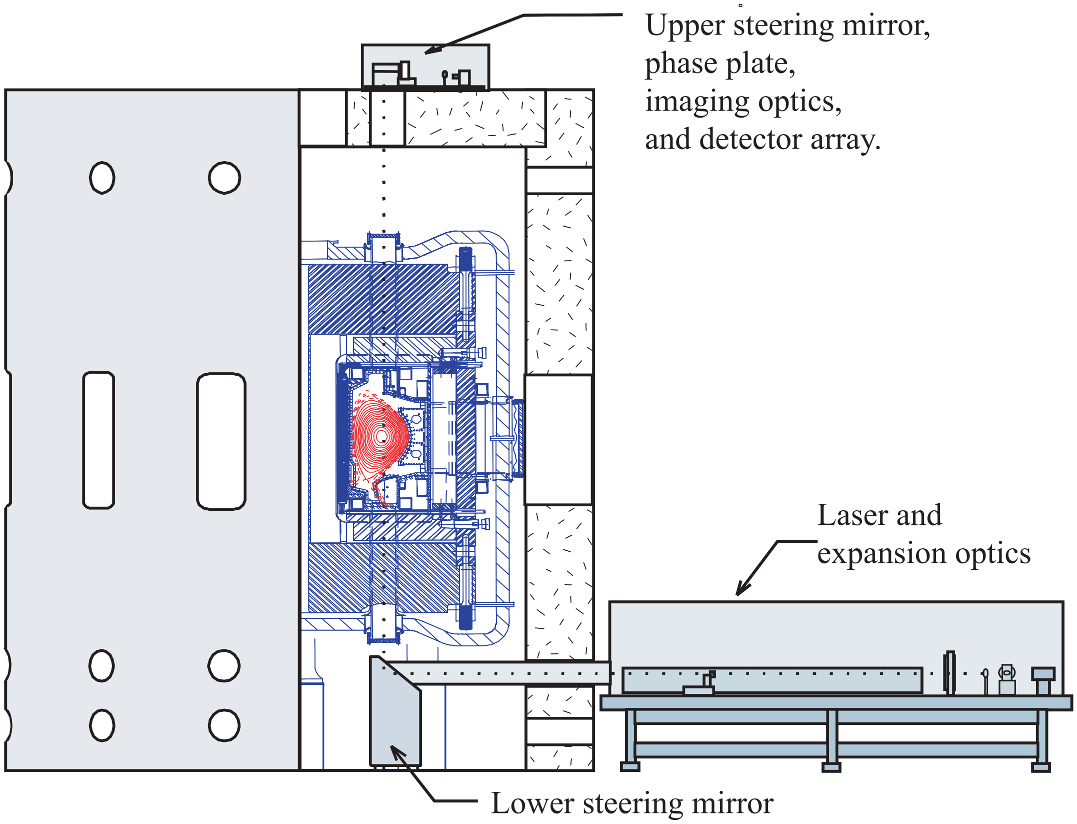

Figure 3-3: The PCI diagnostic in the Alcator C-Mod tokamak, adapted from Ref. 49.

3.2.1 Laser

Because of its coherence in spectrum and steadiness in power, the CO_2 laser is very popular in laser aided plasma diagnostics. A TEM00 mode CO_2 laser (FireStar t60 SYNRAD, Inc) is used in the Alcator C-Mod PCI system, which provides a 60-Watt continuous laser beam to probe the plasma. To eliminate the laser intensity fluctuations due to the temperature variation in the cell, a chiller (M75 Thermo NESLAB) with a temperature control was connected to the laser. Both the laser and chiller are remotely controllable through a programmable logic controller (PLC), which is connected to a PC in the C-Mod control room. Previously, for safety reasons and protection of optics from overheating, the PCI laser was only switched on before the plasma pulse. However, the laser intensity is not stable during the startup phase and this degrades the diagnostic performance. To eliminate this problem, as shown in Fig. 3-4, we have installed a laser safety shutter (Hass Laser Technologies, Inc) in front of the laser, which shares the same chilling water circuit as the laser. With the additional protection from the shutter, the laser is left on during the whole C-Mod run day.

Figure 3-4: Picture of the laser and shutter in the C-Mod PCI system, where the shutter is attached to the laser front.

2.2.2 Transmitting and Imaging Optics

Figure 3-5 shows the beam expansion optics used in the C-Mod PCI system. The output of the CO_2 laser is an invisible beam that can be dangerous. To make the alignment easier, a HeNe laser at 632nm is used and its output beam is overlapped with the CO_2 laser after the beam splitter (BS2) for the purpose of the alignment. The combination of the lens L1 $(F = 40\ \text{in})$, the concave mirror L2 $(F = 1\ \text{in},\ 2\ \text{in, or}\ 6\ \text{in})$, and the parabolic mirror L3 $(F = 80\ \text{in})$ serves as a beam expander and provides a collimated beam to probe the plasma. Since the object width is fixed at the width of the detector array, the expanded beam size should be comparable to the object width divided by the traverse magnification of the imaging optics so that the laser beam power can be used efficiently to enhance the signal level. To accommodate different imaging optics configurations, three options for the focal length of the concave mirror L2 provide a collimated beam with three different widths $(4,\ 11,\ 20\ \text{cm})$.

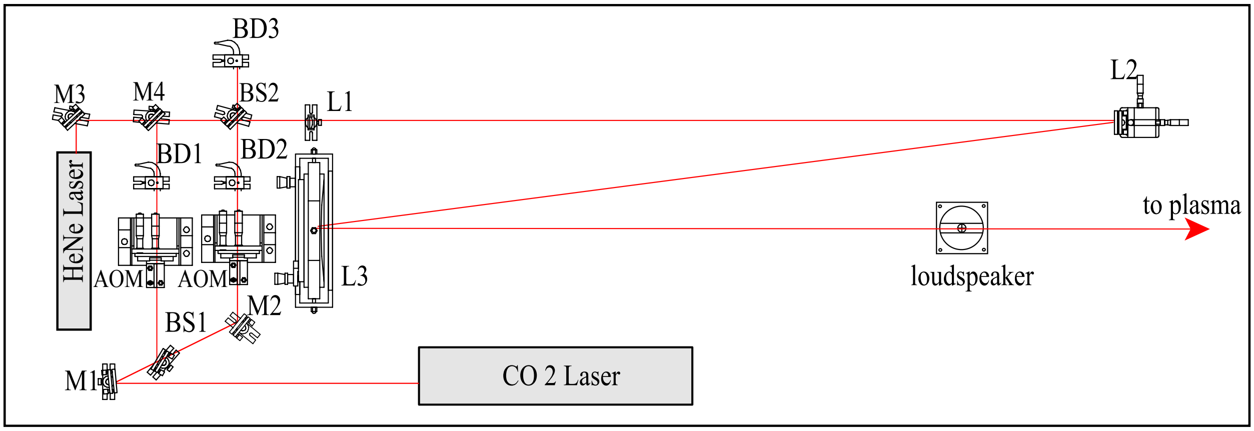

Figure 3-5: Optical arrangement of the transmitting table in the C-Mod PCI system , adapted from Ref. 49.

Previously, the C-Mod PCI diagnostic was mainly used for measuring the longer-wavelength RF waves and fluctuations in the wavenumber range of 2-8 cm^{-1}. The imaging optics configuration was not sufficient to study even longer wavelength MHD waves with wavenumbers below 1 cm^{-1} and short wavelength electron temperature gradient (ETG) modes with wavenumbers above 10 cm^{-1}. Therefore, we have implemented a new imaging optics system consisting of two lenses, L5 with focal length $F = 10 \text{ in}$ and L6 with focal length $F = 2.5 \text{ in}$, as shown in Fig. 3-6. Together with the parabolic mirror L4 ($F = 80 \text{ in}$), the imaging optics work as a telescope and provide an adjustable traverse magnification M in the range of [0.2, 0.8]. The mirrors (M5-M9) on the receiving table are used to make the PCI receiving table compact and take less room.

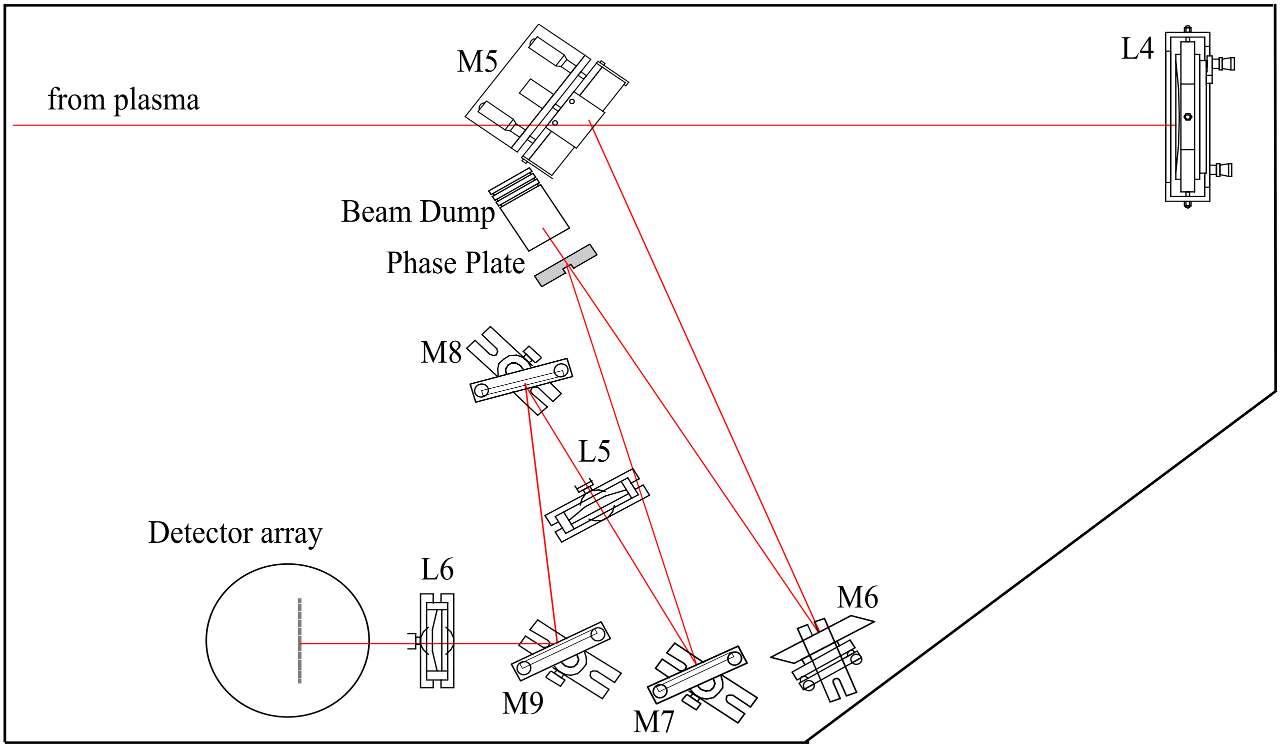

Figure 3-6: Optical arrangement of the PCI receiving optics. The position of parabolic mirror L4 ($F = 80 \text{ in}$) is fixed in the system. The magnification is adjustable by change the positions of lens L5 ($F = 10 \text{ in}$) and L6 ($F = 2.5 \text{ in}$).

3.2.3 Detector and Data Acquisition System

A 32-element HgCdTe photoconductive detector array is used to detect the intensity fluctuations of the laser beam. Each detector element has a height of 1 mm, width of 0.75 mm and is evenly spaced with a separation of 0.1 mm. The whole detector array is located inside a Dewar filled with liquid nitrogen to eliminate thermal noise and improve the system sensitivity. The liquid nitrogen also keeps the detector array from being burnt.

As shown in Fig. 3-7, each detector element is connected with a preamplifier which supplies the needed bias current ~10 mA and provides an additional gain of ~200. The bias current is tunable by adjusting the resistor R_L so that each combination of the detector element and the preamplifier has a similar combined gain. After the preampliers, the analog signals are sent into a 16-bit D-tacq digitizer. The sample rate of the digitizer is set at 10 MHz with all 32 channels, which can be adjustable to 40 MHz with fewer channels. The picture of the digitizer is shown in Fig. 3-8. Finally, these data are stored into the C-Mod MDSPlus data server.

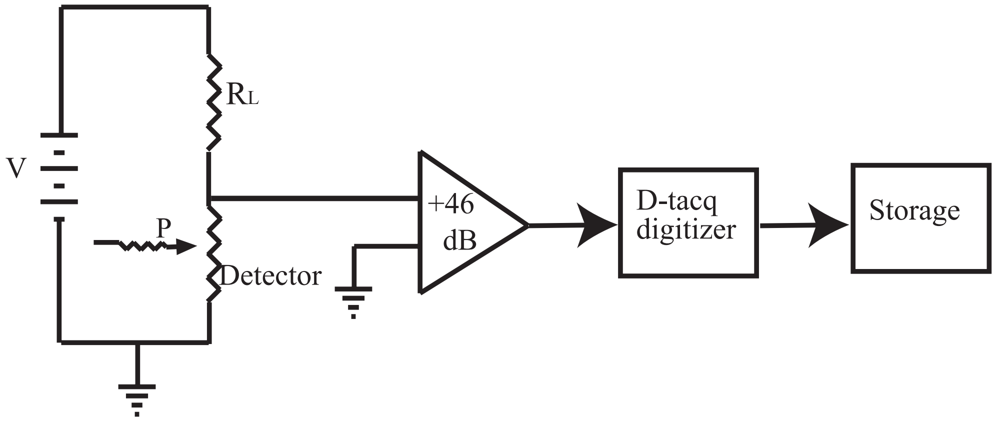

Figure 3-7: Detector and data acquisition system.

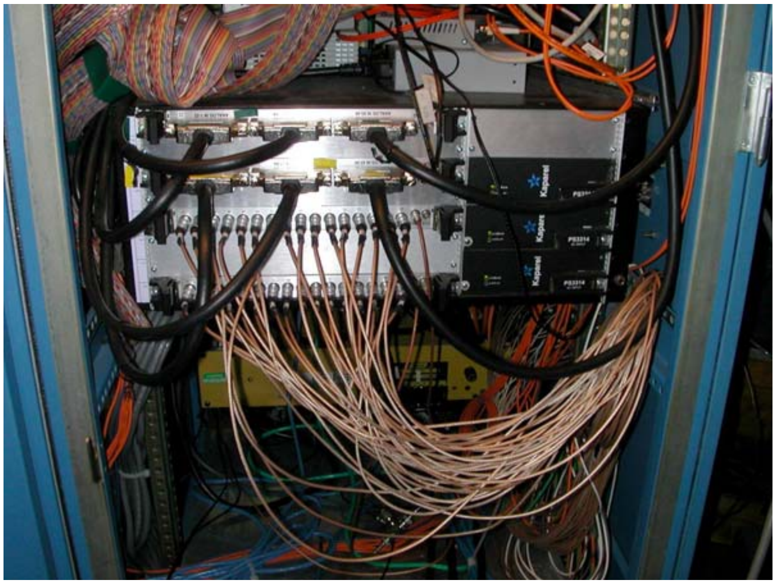

Figure 3-8: Picture of the D-tacq digitizers used in the PCI diagnostic

3.2.4 Absolute Calibration

The response of the PCI system can be gauged using sound waves. A sound wave generates the pressure variation in the air, which causes the phase shift of the laser beam in the same way as turbulent waves in plasmas. Since the inception of the PCI system on Alcator C-Mod, a 15 kHz sound wave from a loudspeaker has been used to provide means for relative calibration across 32 channels. As shown in Fig. 3-9, the loudspeaker speaker is mounted on the PCI transmitting table ~10 cm below the center of the expanded laser beam and launches a sound wave propagating across the laser beam.

The induced pressure oscillations $\tilde{p}$ in the air are measured with a calibrated microphone. The relative phase is also calculated by measuring the time delay between the input signals to the loudspeaker and the output signal from the microphone. After knowing the exact phase variation caused by the launched sound waves, the introduced phase perturbation is[49]

$$\tilde{\Phi} = -\frac{2\pi\left(N_0 - 1\right)}{\lambda_0}\int \frac{\tilde{p}}{\gamma p_0} dl\,, \tag{3.14}$$

where $(N_0 - 1) = 2.72613\times10^{-4}$, $p_0 = 1.01325\times10^{5}$ Pa , $\lambda_0 = 1.06\times10^{-5}$ m and $\gamma = 1.403$ is the ratio of the specific heat, c_p / c_v. This phase perturbation can be converted to the scale of line-integrated density with Eq. (3.4). Absolute calibration is obtained by using the PCI diagnostic to measure these sound waves. Figure 3-10 shows the calibration results by using the 15 kHz sound waves.

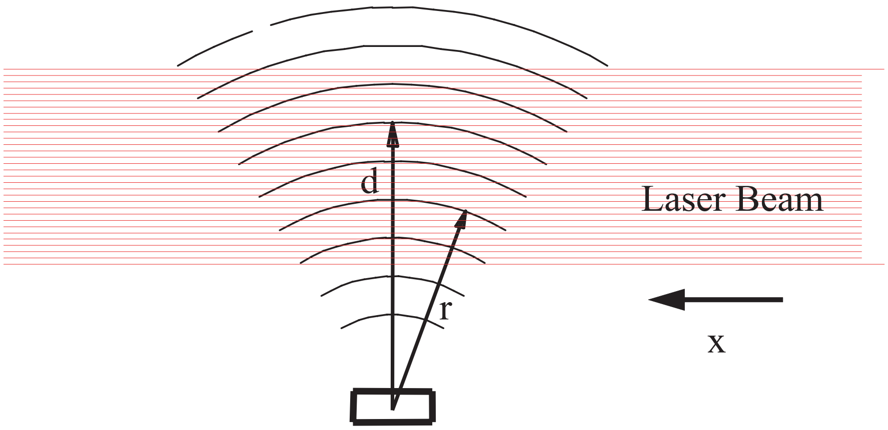

Figure 3-9: Sound waves launched by a loudspeaker

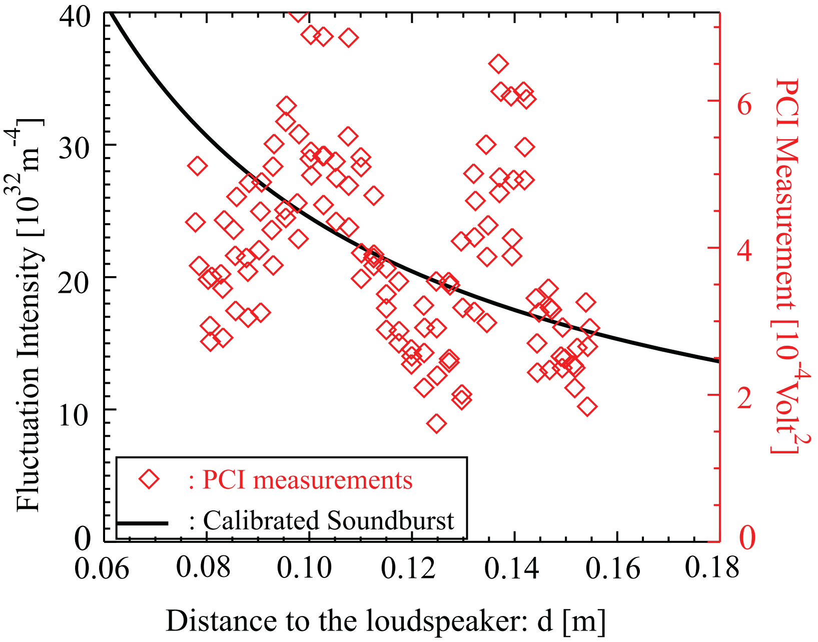

Figure 3-10: Absolute calibration of the PCI system with a 15 kHz sound wave. The black line is the intensity of the sound wave calculated through a spherical wave approximation in the unit of $10^{34}\ \text{m}^{-4}$. The red diamonds are the intensity of PCI measurement of the sound wave in the unit of $10^{-4}\ \text{V}^2$.

Recently, a set of high-frequency transducers[58], with frequencies ranging from 30 kHz to 200 kHz, has been installed, which enables us to test the system's ability of measuring short wavelength fluctuations by measuring shorter wavelength sound waves. Figure 3-11 shows the measurements of 200 kHz sound waves. The strong peak at $k = 37\ \text{cm}^{-1}$ and $f = 200\ \text{kHz}$ corresponds to the sound wave. The measured signal intensity is about two orders higher than the background noise. This measurement verifies the ability of the PCI diagnostic to measure short wavelength turbulent waves.

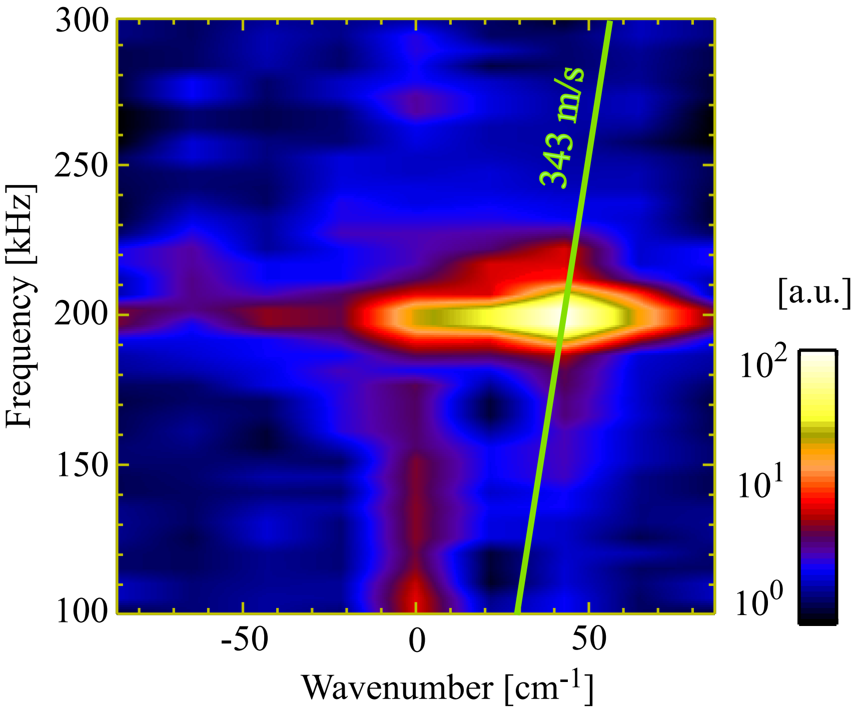

Figure 3-11: PCI measurement of 200 kHz ultrasonic wave in frequency-wavenumber space.

In summary, the extensive upgrades in optics and electronics have enabled the C-Mod PCI diagnostic to measure turbulent density fluctuations in the wavenumber range of 0.5-55 cm^{-1} and in the frequency range of 2 kHz to 5 MHz. The diagnostic performance improvements are summarized in Table 3-1.

Table 3-1: System performance improvement after the upgrade

	Before	Improvement	After
Laser	20 W	×3	60 W
f_{max}	0.5 MHz	×10	5 MHz
k_{max}	8.3 cm^{-1}	×6.6	55 cm^{-1}
$\Delta k/k$	12	×2.7	32

3.3. Vertical Localization

As shown in Fig. 3-12, the conventional PCI setup measures line-integrated electron density fluctuations. In general, the lack of localization is a major drawback of the PCI system. Furthermore, the laser beam is scattered by turbulence waves propagating in electron or ion diamagnetic directions into the opposite directions at the plasma top and bottom when passing through plasmas. Since the conventional PCI setup integrates electron density fluctuations equivalently along the vertical chord, it cannot distinguish the contribution to the measured turbulence from the plasma top and bottom. Consequently, it cannot resolve the direction of propagation of fluctuations. A recent localizing upgrade has partially resolved the above drawback of the conventional setup.

3.3.1 Principle of Vertical Localization

Under certain assumptions, some information on the spatial localization can be retrieved. In a tokamak (or stellarator) geometry, the main component of the magnetic field is the toroidal magnetic field. The presence of a poloidal magnetic field component allows some localization of the shorter wavelength fluctuations.[59-62] The method relies on the fact that the magnetic pitch angle,

$$\beta = \arctan(\frac{B_R}{B_\phi}) , \tag{3.15}$$

changes along a vertical chord passing through the plasma as shown in Fig. 3-13, where B_R is the magnetic field component along the major radius and B_ϕ is the toroidal magnetic field. Since the wave-vectors of the drift-wave turbulence are mainly perpendicular to the field lines[63], i.e. $\mathbf{k} \cdot \mathbf{B} \approx 0$, they also rotate from the bottom to the top of the plasma as the field pitch angle rotates. This rotation is imaged onto the phase plate used in the PCI system. Therefore, by partially masking that phase plate, we can select a vertical region of interest. Figure 3-13 shows the physics behind the principle of localization by means of the magnetic pitch angle variation.

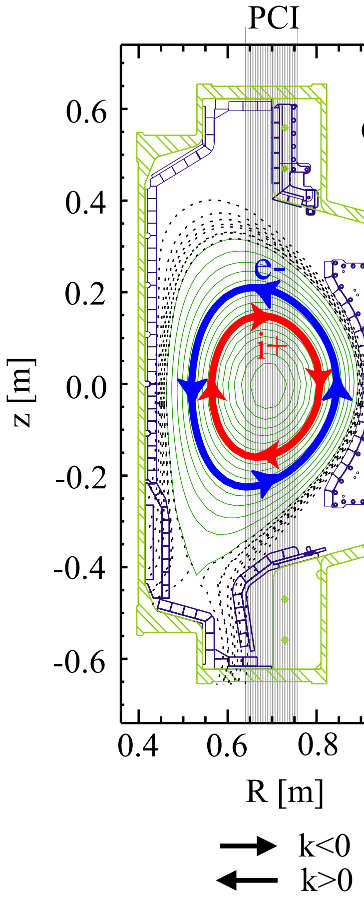

Figure 3-12. Laser beam path of the Alcator C-Mod PCI diagnostic, where the turbulence waves propagating in the electron (blue) and ion diamagnetic direction (red) are also labeled. The sign convention of the wavenumber used in this thesis is also indicated. The positive wavenumber corresponds to the waves propagating toward high field side (HFS), while the negative wavenumber corresponds to the waves propagating toward the low field side (LFS).

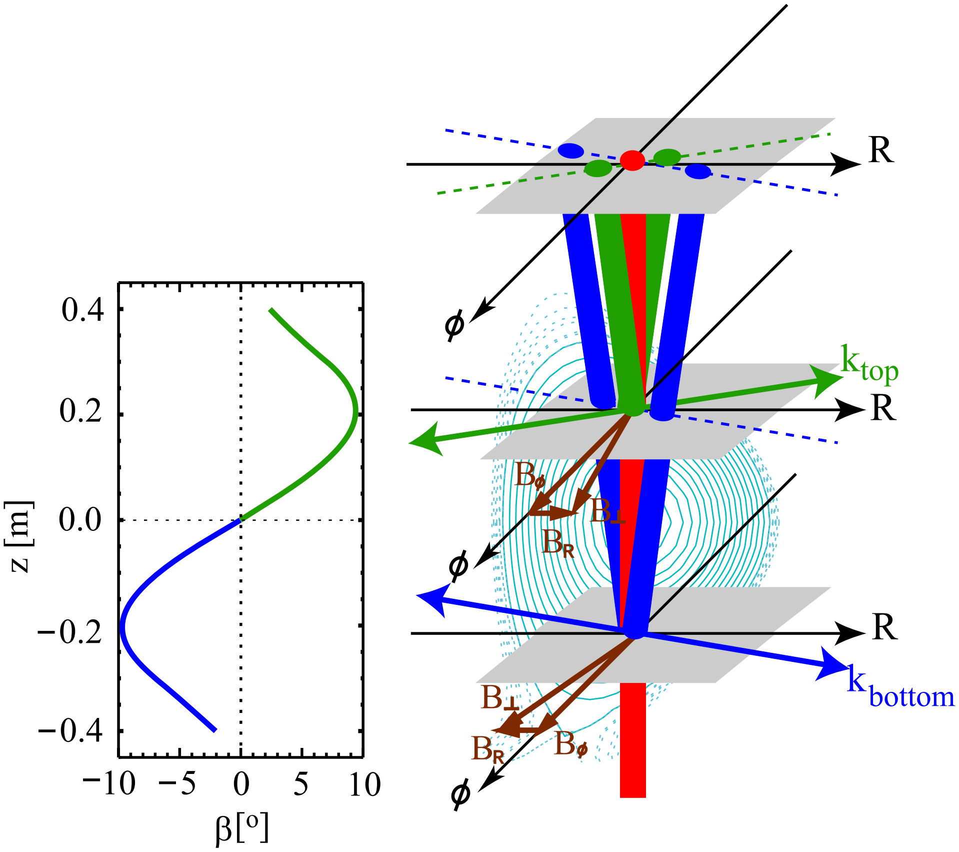

Figure 3-13. Left: Vertical coordinate z vs. magnetic pitch angle β. Right: principle of vertical localization by taking advantage of the variation of the magnetic pitch angles along the probing beam. In the diagram, the red beam corresponds to the unscattered beam, the blue beams correspond to the scattered beam due to the turbulence waves localized at the plasma bottom ($z<0$; $\beta<0$), and the green beams correspond to scattered beams due the turbulence waves localized at the plasma top ($z>0$; $\beta>0$).

3.3.2 Estimation of Localization Performance

The injected laser beam is scattered by density fluctuations along its propagation. All the scattered beams are focused on the phase plate. The performance of localization depends on the spatial separation s of scattered beams. As shown in Fig. 3-14, for two scattered beams due to density fluctuation at z_1 and z_2, the spatial separation of the focused spots on the phase plate is

$$S \simeq (2\pi\lambda_0 F_0)\,|\sin\beta_1 - \sin\beta_2\,|\,k\,, \tag{3.16}$$

where $\lambda_0 = 1.06\times10^{-3}\,\mathrm{cm}$ is the wavelength of CO$_2$ laser, $F_0 = 203\ \mathrm{cm}$ is the focal length of the parabolic mirror in PCI, and β_1 (β_2) is the magnetic pitch in degrees at z_1 (z_2). For typical plasmas in Alcator C-Mod, $|\beta|\leq 10^{\mathrm{o}}$, thus $\sin\beta \simeq \pi\beta/180$. We can rewrite S as

$$S \simeq \frac{k\pi^2\lambda_0 F_0}{90}\,|\,\beta_1 - \beta_2\,| \propto k\Delta\beta\,. \tag{3.17}$$

For the short wavelength fluctuations, such as the electron temperature gradient (ETG) modes, the distance between the two scattered beams from z_1 and z_2 are larger than the beam diameter (w_p), i.e. $S > w_p$. These two scattered beams are completely separated; thus, by adding a mask on the top of the phase plate, we can view one beam but filter the other one completely, thereby obtaining localized turbulence measurements.

For the longer wavelength turbulence, such as the ion temperature gradient (ITG) modes and the trapped electron modes (TEMs), $S \lesssim w_p$, we cannot obtain the well localized measurement. However, the added masking can be set to view one beam preferentially. For an example, when $z_1 \simeq -z_2$, the density fluctuation comes from the same magnetic flux but top or bottom part of plasma. By configuring the mask to view one beam preferentially, the PCI diagnostic can be set to preferentially view the turbulence from the top or bottom of plasma. Thus, the contribution to the line-integration in the PCI measurements from the plasma top and bottom can be differentiated. As shown in Fig.3-14, by viewing the top or bottom plasma preferentially, PCI can resolve the dominant mode propagating direction.

(a) Conventional phase plate

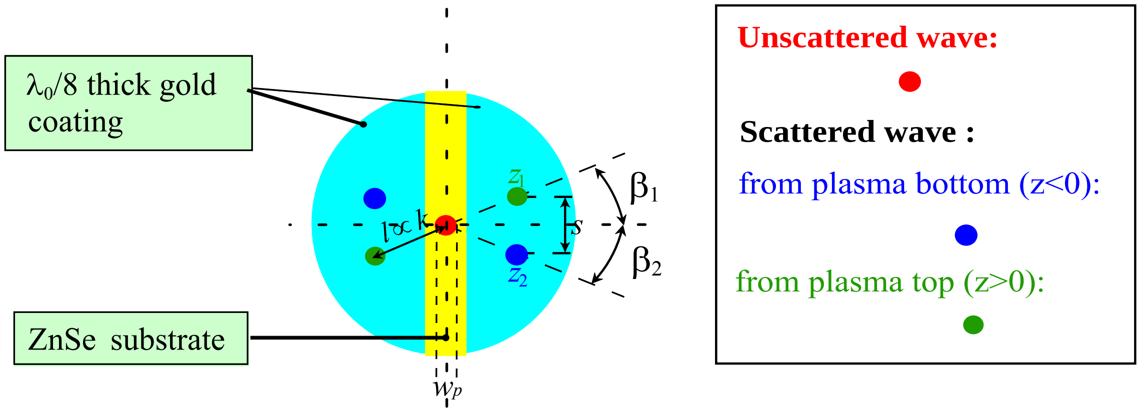

(b) Combination of phase plate and mask

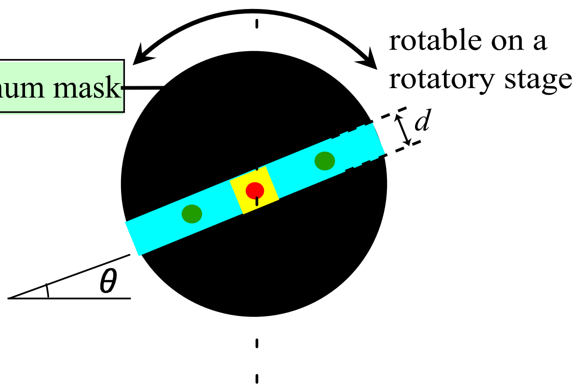

Figure 3-14: Localization hardware setup: (a) the diagram of the conventional phase plate, where the scattered beams due to turbulence waves from the whole plasma column is collected; (b) the diagram of combination of a phase and mask, where only the scattered beam due to the turbulent waves from the plasma top $z>0$ is collected.

3.3.3 Localization Hardware

In the Alcator C-Mod PCI system, a mask is placed on the top of the phase plate for the localized measurement. To remotely rotate the phase plate and select different regions along the beam, the phase plate and the mask are mounted on a motorized rotary stage (SGSP-60YAW OptoSigma Corp.). Table 2 lists the general specifications of the rotary stage. The motor is driven with an SG-55M compact micro-driver. This driver is controllable through a programmable logic controller (PLC), which is connected to a PC in the C-Mod control room. This remote control allows for rotating the mask and selecting a vertical region of interest. The maximum traveling speed of the rotary stage is 30 degrees per second, which allows one scan of the whole plasma column in a second. Currently, the angle of the rotary stage is fixed during a single discharge and the adjustment is only performed between the discharges.

Table 3-1.SGSP-60YAQ rotory stage specifications

Model	SGSP-60YAW
Motor	TS3664N4 (0.66A/phase)
Travel per pulse (degrees)	0.005/0.0025
Positional Repeatability (degrees)	0.02 or less
Lost Motion (degrees)	0.05 or less
Face runout angle (mm)	0.02 or less
Material	Aluminum Alloy
Load capacity (kg)	4
Maximum traveling speed (degree/sec)	30

The rotary stage is attached on a 3-D translational stage, as shown in Fig. 3-15. Two of three stage movements are controlled by DC motors, and the third one is controlled manually. The motors are also connected to the PLC, which allows for remotely adjusting the phase plate to center the unscattered beam on the phase plate and maximize the phase contrast between the scattered and unscattered beams. The laser beam drifts slightly during one C-Mod run day and this remote alignment also ensures the diagnostic performance. At last, the 3D translation stage is fixed on the top of a 2-axis tilt platform for the purpose of the optics alignment after the phase plate.

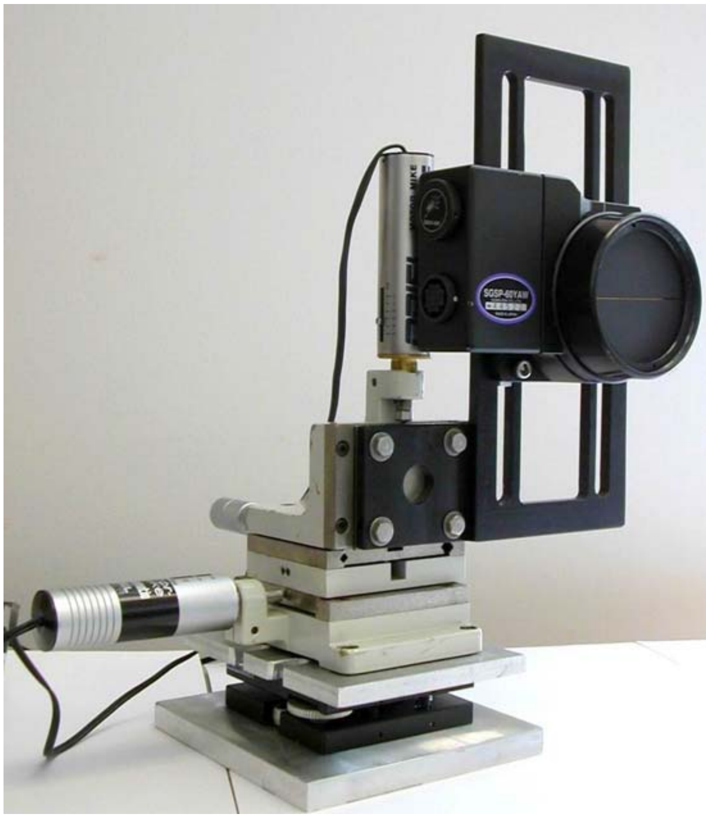

Figure 3-15: Photography of the assembly of the masked phase plate.

3.4.4 Experimental Test of Localization

The quasicoherent (QC) mode[54] localized around the plasma edge and propagating in the electron diamagnetic direction has been used as a candidate to test the localization capability of our system. Since the wave number of the QC mode is relatively low ($k \sim 5\ \mathrm{cm}^{-1}$), the system can only differentiate between the top and the bottom localization in the plasma cross section. Figure 3-16 shows the two-dimensional Fourier transform spectra of the experimental measurements. In Fig. 3-16(a), the masking plate was set up primarily to view the bottom of the plasma column, and we see that the positive wave number QC ($f \sim 100\ \mathrm{kHz}$; $\mathrm{k}{\sim}5\ \mathrm{cm}^{-1}$) dominates. In Fig. 3-16(b), the masking plate was set up mainly to view the top of the plasma column, and it is seen that the negative wave number QC mode dominates. This measurement agrees with the fact that the QC mode propagates in the electron diamagnetic direction. We note that in the frequency range of [160, 350] kHz, turbulence propagating in the ion diamagnetic direction dominates, and this possibly corresponds to the ion temperature gradient (ITG) mode. Since the top/bottom differentiation is better than for the QC modes, this broadband turbulence has to be localized further radially inward, where the top/bottom magnetic pitch angle difference is large (see Fig. 3-13). More detailed comparisons with nonlinear gyrokinetic simulations in Chapter 6 confirm that this broadband turbulence corresponds to the ITG turbulence.

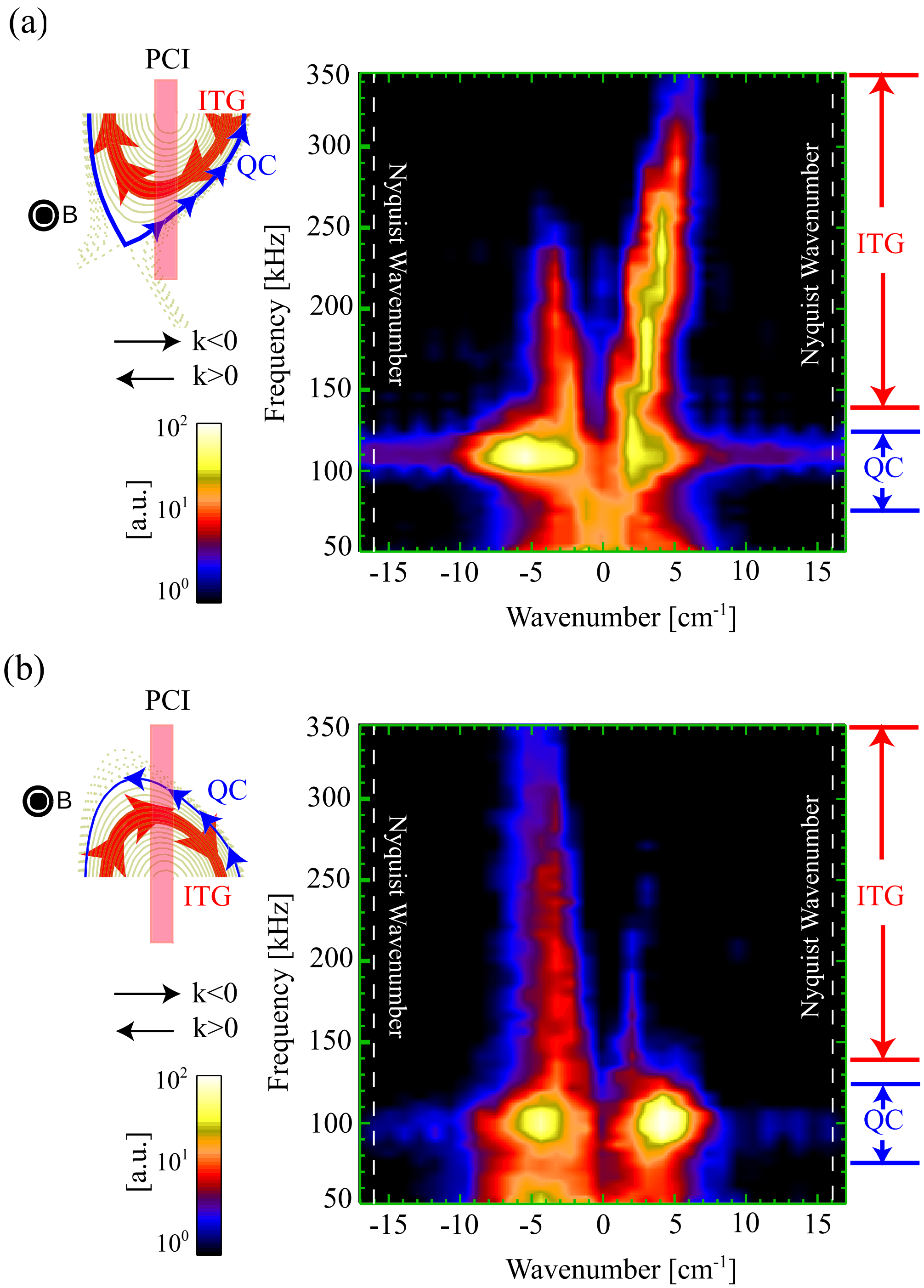

Figure 3-16: Comparison of the frequency wavenumber spectra measured by the localizing PCI setup: (a) the top plasma view; (b) the bottom plasma view. The line view of each diagnostic configuration is plotted on the left. The Niquist wavenumber of the used optics configuration is also labeled on the spectra.

3.4 Summary

In this chapter, we have discussed the PCI technique and its implementation in Alcator C-Mod. PCI is a sensitive technique to study various fluctuations with a broad range in both wavenumbers and frequencies. The PCI diagnostic in Alcator C-Mod is capable of measuring density fluctuations with temporal (10 kHz-5 MHz) and wavenumber (0.5-55 cm^{-1}) resolution. Recent upgrades have also enabled the PCI system to localize the short wavelength turbulence in the ETG range and resolve the direction of propagation (i.e., electron vs. ion diamagnetic direction) of even the longer wavelength turbulence in the ITG/TEM range. In the next few chapters, we will discuss turbulence and transport studies in various plasmas in Alcator C-Mod using the PCI diagnostic.

Chapter 4

Gyrokinetics

To quantitatively model turbulence and anomalous transport in plasmas, it is necessary to simultaneously address the source of turbulence, characteristics of the fluctuating quantities, and the resulting transport. Analytic analysis of drift waves, such as described in Chapter 2, is of limited value, so it is important to perform "first-principle" numerical simulations of plasma turbulence that results from the nonlinear interactions of drift waves and particles. The gyrokinetic equation provides a theoretical and first-principles based foundation for simulating nonlinear drift-wave turbulence and the cross-field transport of particles and energy. Recent advances in gyrokinetic code development with the advent of powerful high-performance computers allow for the "full physics" simulations to accurately and quantitatively predict turbulence and associated transport in fusion plasmas. However, to use these numerical codes to predict and optimize relevant fusion plasma performance with confidence, it is crucial to validate these codes against experimental measurements at multiple levels, including both turbulence and transport.

In this chapter, we will describe the gyrokinetic equation and its numerical simulation. We will also describe a synthetic phase contrast imaging (PCI) diagnostic method, which allows for direct and quantitative comparisons between numerical predictions and experimental fluctuation measurements.

4.1 The Gyrokinetic Equations

The development of the gyrokinetic equation was motivated by the need of a general theory to describe a wide range of plasma phenomena with low frequencies (compared to the cyclotron frequency) . The linear gyrokinetic theory was derived by Rutherford and Frieman in 1968[64] and the nonlinear gyrokinetic theory was developed by Frieman and Chen in 1982[65]. Many alternative derivations and extensions appeared after these early works[66-71]. A general review of the gyrokinetic theory can be found in Refs. 72 and 73. In this section, we outline the major steps in deriving the gyrokinetic equation to introduce the gyrokinetic approximation in a simple and physical way. Our derivation follows a similar approach as in Refs. 74 and 75 and starts from the Boltzmann equation,

$$\frac{\partial f}{\partial t}+\mathbf{v}\cdot\nabla f+\frac{q}{m}\left(\mathbf{E}+\mathbf{v}\times\mathbf{B}\right)\cdot\frac{\partial f}{\partial \mathbf{v}}=C(f,f)\,, \tag{4.1}$$

where $f(\mathbf{x},\mathbf{v},t)$ is a distribution function depending on phase-space coordinates $(\mathbf{x},\mathbf{v})$ and time t. The term $C(f,f)$ on the right-hand side of Eq. (4.1) describes the collision effect, which occurs through the cumulative contribution of many small angle scatterings. Equation (4.1) is essentially nonlinear, since the electromagnetic fields $\mathbf{E}$ and $\mathbf{B}$ also depend on the distribution function f through Maxwell equations. Computationally solving Eq. (4.1) directly is impossible since it requires enormous amount of computer resources; thus, approximations based on the characteristics of drift waves are necessary.

In typical low-β tokamak plasmas where the plasma pressure is much smaller than the magnetic pressure, drift waves are low frequency modes that exist in inhomgeneous plasmas and are destabilized by the density and temperature inhomogeneities, and magnetic effects. Their characteristics are low frequencies (compared with the cyclotron frequency) and small spatial scale (compared to the equilibrium scale length). These basic properties result in the gyrokinetic ordering,

$$\frac{\tilde{f}}{F_0} \sim \frac{e\tilde{\phi}}{T_0} \sim \frac{A_\parallel}{B_0\rho} \sim \frac{\tilde{B}}{B_0} \sim \frac{\omega}{\Omega} \sim \frac{\rho}{L} \sim \varepsilon, \tag{4.2}$$

$$k_\parallel L \sim k_\perp \rho \sim O(1), \tag{4.3}$$

where $\tilde{f}$ is the perturbed distribution function and F_0 is the equilibrium distribution function, $\tilde{\phi}$ and $\tilde{B}$ are perturbed potential and magnetic field, respectively, $A_\parallel$ is the component along the equilibrium magnetic field of the perturbed magnetic vector potential $\mathbf{A}$, B_0 is the magnitude of the equilibrium magnetic field, L is the equilibrium scale length, $\rho = \upsilon_t / \Omega$ is the thermal gyroradius of a given particle species with the thermal velocity $\upsilon_t = \sqrt{T/m}$ and cyclotron frequency $\Omega = qB_0/m$, and m is the mass and q is the charge.

The gyrokinetic ordering in Eqs. (4.2) and (4.3) is the key to split the distribution function and electromagnetic fields in Eq. (4.1) into the slowly-varying equilibrium and the fast-varying fluctuating quantities. The ordering contains two basic length scales (the macroscopic length L and the microscopic length ρ) and three basic frequency scales (the fast cyclone frequency Ω, the medium frequency $\omega \sim \varepsilon\Omega$, and the slow transport rate $\varepsilon^2\Omega$).

The motion of a charge particle in a magnetic field can be decomposed into the fast gyration with the characteristic frequency Ω and the slowly drifting motion of the gyro-center $\mathbf{R}$ with the characteristic frequency $\varepsilon\Omega$. The position of the particle can be expressed as

$$\mathbf{x} = \mathbf{R} - \frac{\mathbf{v} \times \mathbf{b}_0}{\Omega}, \tag{4.4}$$

where $\mathbf{b}_0 \equiv \mathbf{B}_0 / B_0$. To further extract the smooth drift-kinetic-like behavior in the medium frequency scale ($\varepsilon\Omega$), a gyro-average operator is used, which is defined on $a(\mathbf{r}, \mathbf{v}, t)$ as

$$\left\langle a(\mathbf{r}, \mathbf{v}, t) \right\rangle_{\mathbf{R}} = \frac{1}{2\pi} \int_0^{2\pi} a\left(\mathbf{R} - \frac{\mathbf{v} \times \mathbf{b}_0}{\Omega}, \mathbf{v}, t \right) d\xi . \tag{4.5}$$

This gyro-averaging is essentially an integral over a full gyro-period of the gyro-phase ξ while keeping the gyro-center $\mathbf{R}$ and the velocity $\mathbf{v}$ fixed. It reduces the dimensionality of Eq. (4.1) from 6-D to 5-D by eliminating the gyro-phase ξ. This 5-D space include the gyro-center position $\mathbf{R}$ and two velocity components $(\upsilon_\parallel, \upsilon_\perp)$. In some other places, the magnetic moment $\mu = m\upsilon_\perp^2 /(2B)$ is used instead of $\upsilon_\perp$. This removal of the gyro-phase coordinate allows for a more effective computation of the low-frequency drift waves. Based on the gyrokinetic ordering, the Boltzmann equation can be expanded as:

$$\begin{aligned}
&\underbrace{\frac{\partial F_0}{\partial t}}_{\varepsilon^2} + \underbrace{\frac{\partial \tilde{f}}{\partial t}}_{\varepsilon} + \underbrace{\mathbf{v}_\perp \cdot \nabla \tilde{f}}_{1} + \underbrace{\mathbf{v}_\parallel \cdot \nabla \tilde{f}}_{\varepsilon} \\
&\underbrace{-\frac{q}{m} \nabla \tilde{\phi} \cdot \frac{\partial F_0}{\partial \mathbf{v}}}_{1} \underbrace{- \frac{q}{m} \frac{\partial \mathbf{A}}{\partial t} \cdot \frac{\partial F_0}{\partial \mathbf{v}}}_{\varepsilon} + \underbrace{\frac{q}{m} \left(\mathbf{v} \times \tilde{\mathbf{B}} \right) \cdot \frac{\partial F_0}{\partial \mathbf{v}}}_{1} + \underbrace{\frac{q}{m} \left(\mathbf{v} \times \mathbf{B}_0 \right) \cdot \frac{\partial F_0}{\partial \mathbf{v}}}_{\varepsilon^{-1}} \\
&\underbrace{-\frac{q}{m} \nabla \tilde{\phi} \cdot \frac{\partial \tilde{f}}{\partial \mathbf{v}}}_{\varepsilon} \underbrace{- \frac{q}{m} \frac{\partial \mathbf{A}}{\partial t} \cdot \frac{\partial \tilde{f}}{\partial \mathbf{v}}}_{\varepsilon^2} + \underbrace{\frac{q}{m} \left(\mathbf{v} \times \tilde{\mathbf{B}} \right) \cdot \frac{\partial \tilde{f}}{\partial \mathbf{v}}}_{\varepsilon} + \underbrace{\frac{q}{m} \left(\mathbf{v} \times \mathbf{B}_0 \right) \cdot \frac{\partial \tilde{f}}{\partial \mathbf{v}}}_{1} \\
&= \underbrace{C(F_0, F_0)}_{1} + \underbrace{C(F_0, \tilde{f})}_{\varepsilon} + \underbrace{C(\tilde{f}, F_0)}_{\varepsilon} + \underbrace{C(\tilde{f}, \tilde{f})}_{\varepsilon^2}
\end{aligned} \quad , \tag{4.6}$$

where the electric field $\mathbf{E}$ has been expressed in terms of the scalar potential $\tilde{\phi}$ and the vector potential $\mathbf{A}$

$$\mathbf{E} = -\nabla \tilde{\phi} - \frac{\partial \mathbf{A}}{\partial t}, \tag{4.7}$$

and the order of each term relative to $F_0 \upsilon / L$ is labeled below.

At the $O(\varepsilon^{-1})$ order,

$$\frac{q}{m}\left(\mathbf{v}\times\mathbf{B}_0\right)\cdot\frac{\partial F_0}{\partial\mathbf{v}}=-\Omega\left(\frac{\partial F_0}{\partial\xi}\right)=0, \tag{4.8}$$

which shows the equilibrium distribution function F_0 has no dependence on gyrophase angle ξ. After imposing the gyro-phase average and solving the hierarchical equations up to $O(\varepsilon)$, the total distribution function f is

$$f=F_0\exp\left(-\frac{q\tilde{\phi}}{T_0}\right)+h(\mathbf{R},\upsilon_{\|},\upsilon_{\perp},t)+O\left(\varepsilon^2\right). \tag{4.9}$$

The detailed derivation of Eq. (4.9) can be found in Refs. 76 and 77. The first term on the RHS of Eq. (4.9) is the equilibrium distribution function F_0 modified with the Boltzmann factor. The gyrokinetic equation for the second term on the RHS of $h(\mathbf{R},\upsilon_{\|},\upsilon_{\perp},t)$ is,

$$\begin{aligned}\frac{\partial h}{\partial t}&+\upsilon_{\|}\mathbf{b}_0\cdot\nabla h+\mathbf{v}_{\chi}\cdot\nabla h+\mathbf{v}_B\cdot\nabla h-\left\langle C\left(h\right)\right\rangle_{\mathbf{R}}\\&=q\frac{F_0}{T_0}\frac{\partial\left\langle\phi-\mathbf{v}\cdot\mathbf{A}\right\rangle_{\mathbf{R}}}{\partial t}-\mathbf{v}_{\chi}\cdot\nabla F_0,\end{aligned} \tag{4.10}$$

where

$$\mathbf{v}_B=\frac{\mathbf{b}_0}{\Omega}\left(\upsilon_{\|}^2\mathbf{b}_0\cdot\nabla\mathbf{b}_0+\frac{\upsilon_{\perp}^2}{2}\nabla\ln B_0\right), \tag{4.11}$$

$$\mathbf{v}_{\chi}=\frac{\mathbf{b}_0}{\Omega}\frac{q\left\langle\nabla\left(\phi-\mathbf{v}\cdot\mathbf{A}\right)\right\rangle_{\mathbf{R}}}{m}. \tag{4.12}$$

The gyrokinetic equation solves the non-adiabatic part of the perturbed distribution function $h(\mathbf{R},\upsilon_{\|},\upsilon_{\perp},t)$ along the trajectories of the guiding center for the given electromagnetic fields and equilibrium distribution function.

The perturbation of the electromagnetic fields due to the perturbed distribution function can be solved using quasi-neutrality and Ampere's Law as follows:

$$\sum_i \left\{ -\frac{n_i q_i^2 \tilde{\phi}}{T_i} + q_i \int d^3\mathbf{v} h_i \right\} = \frac{n_e e^2 \tilde{\phi}}{T_e} + e \int d^3\mathbf{v} h_e , \tag{4.13}$$

$$-\nabla^2 \mathbf{A} = \sum_i \left\{ \mu_0 q_i \int d^3\mathbf{v}\mathbf{v} h_i \right\} - \mu_0 e \int d^3\mathbf{v}\mathbf{v} h_e , \tag{4.14}$$

where the subscripts i and e represent the ion and electron species, respectively, and the summation is over all ion species. Overall, the gyrokinetic equations describe the evolution of the perturbed distribution function along the trajectories of the guiding center. After the nonlinear saturation level of the perturbed distribution function perturbation $\tilde{f}$ is obtained, its perturbation to the plasma equilibrium can be solved through the transport equation in the larger time scale. The closure of the gyrokinetic equations is shown in Fig. 4-1.

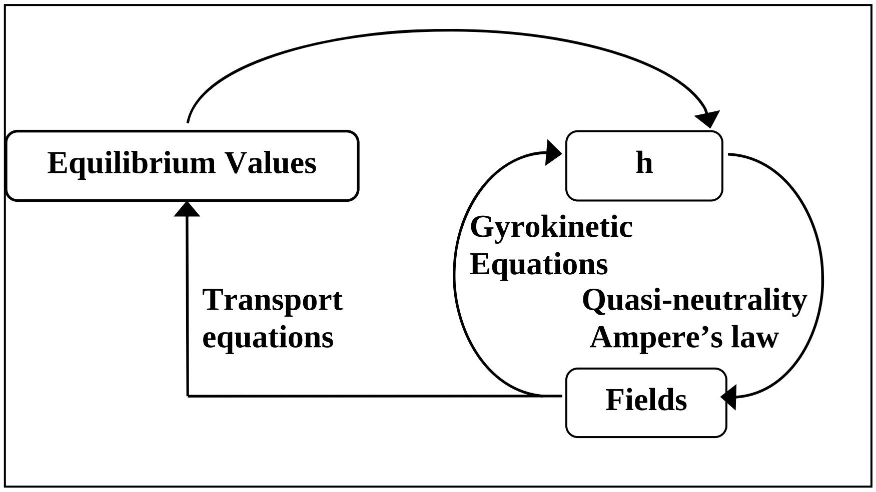

Figure 4-1: Closure of gyrokinetic equations, adapted from Ref. 75.

4.2 Gyrokinetic Simulation

Quantitatively solving the gyrokinetic equation for real plasmas in a complicated fusion device is only possible through numerical methods. The development of comprehensive gyrokinetic codes has been one of the triumphs of computational and theoretical plasma physics in the past ten years. In principle, gyrokinetic equations can be solved through two different numerical approaches: (1) Lagrangian or particle-in-cell (PIC) approach; (2) Eulerian or “continuum” approach. The PIC approach integrates the gyrokinetic equations of motion for millions of particles, while the continuum approach uses finite difference together with spectral methods on a discrete grid. A detailed discussion of each approach and its relative advantages is beyond the scope of this thesis and can be found in Refs. 78 and 79. It is useful to have both types of codes so that they can cross-check each other for the purpose of verification. To meet the requirement of the predictive modeling capability for ITER and future fusion reactors, many numerical codes have been developed. GTC[80] and GEM[81] are the major PIC codes, while GS2[82,83], GENE[84], and GYRO[85-86] are the major continuum-based gyrokinetic codes.

In this thesis, GYRO is used for both linear stability analysis and nonlinear simulations, because of its physical comprehensibility, availability, and great documentation.[87] GYRO is developed by Candy and Waltz at General Atomics and is generally believed to contain the “full physics” necessary for accurate core tokamak plasma simulations. This necessary physics includes the equilibrium E×B shear effect, trapped and passing electrons, and finite-β effect. Moreover, GYRO includes global effects, especially the effect from profile variations, which is crucial when comparing with non-local fluctuation measurements.

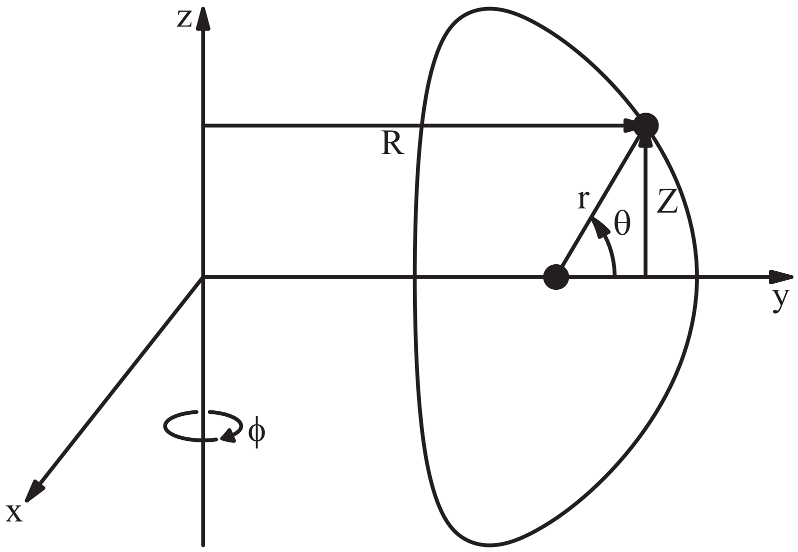

Figure 4-2: Conversion between various coordinate system.

Besides the familiar circular geometry, the GYRO simulation can also be performed in a Miller shaped geometry[88] to obtain a realistic treatment of plasma shape. In the Miller geometry, nine parameters are required to fully describe the noncircular equilibrium: aspect ratio $R_0(r)/a$, elongation κ, triangularity δ, magnetic shear $\hat{s}$, pressure gradient α, safety factor q, $\partial_r R_0$, $\partial_r \kappa$, and $\partial_r \delta$. The flux-surface as shown in Fig. 4-2 is parameterized through a standard formula for D-shaped plasmas:

$$R(r,\theta) = R_0(r) + r\cos\left(\theta + \sin^{-1}\left[\delta(r)\right]\sin\theta\right), \tag{4.15}$$

$$Z(r,\theta) = \kappa(r) r \sin\theta \qquad , \tag{4.16}$$

where θ refers to an angle in the poloidal plane.

4.2.1 Linear Stability Analysis

Linear GYRO uses an initial value approach since it can be more easily generalized to nonlinear simulation. However, the initial value approach is restricted to only resolve the fastest growing (or least damped) eigenmode. Essentially, the linear GYRO stability analysis calculates the real frequency (ω_n) and linear growth rate (γ_n) of the most unstable drift-wave mode with the toroidal mode number n by assuming that the perturbed potential $\tilde{\phi}_n$ takes the form of

$$\tilde{\phi}_n(r,\theta,t) = \hat{\phi}_n(r,\theta) e^{-i\omega_n t + \gamma_n t}. \tag{4.17}$$

The toroidal mode number n can also be related to the local poloidal wavenumber k_θ via

$$k_\theta = \frac{nq(r)}{r}, \tag{4.18}$$

where $q(r) = rB_\phi / RB_\theta$ is the safety factor, B_θ is the poloidal magnetic field, B_ϕ is the toroidal magnetic field, R is the major radius, and r is the minor radius. For the linear stability analysis, each mode is resolved independently and locally and there is no explicit dependence on r. Therefore, the linear stability analysis is actually solving a reduced 1-D equation in θ and the reduced equation is similar to the 1-D equation for typical MHD ballooning modes.

The GYRO code only takes an input file with certain format. In our linear stability analysis and nonlinear simulations, the input file is prepared from the output of TRANSP[89] using the data translator (TRGK) developed at PPPL. Figure 4-3 shows the processing flow structure of a GYRO simulation. First, the experimental data are sent to TRANSP for a local transport analysis, where the experimental particle and energy diffusivities are calculated, the measured profiles are smoothed, and unmeasured profiles necessary for the gyrokinetic simulation are also modeled. Second, TRGK reads the output of the TRANSP analysis and converts the profiles to the GYRO form. Third, the converted profiles are used for GYRO simulations. After a simulation is completed, a user can analyze the simulated and experimental results.

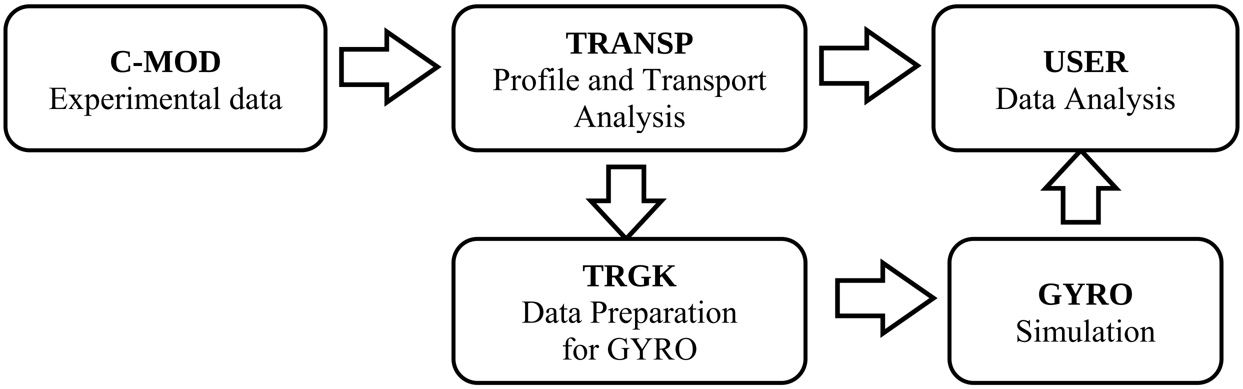

Figure 4-3: Processing flow structure of a GYRO simulation

For the purpose of verification, we have compared the growth rate and frequency spectra of the ion temperature gradient (ITG) turbulence calculated by GYRO and GS2 on the same C-Mod ohmic plasmas, where the input file for GS2 is prepared from the data translator (GS2_prep[90]) developed by Ernst at MIT. The key parameters prepared for GYRO and GS2 are listed in Table 4-1, where $a/L_{T_{e,i}} = -(a/T_{e,i})(\partial T_{e,i}/\partial r)$ and $a/L_{n_{e,i}} = -(a/n_{e,i})(\partial n_{e,i}/\partial r)$. The prepared parameters from these two data translators show a 5% difference because of the different smoothing methods after loading experimental data from TRANSP. The calculated growth rate and frequency spectra are shown in Fig. 4-4, where the discrepancies are less than 15%. Further analysis using the same input parameter for GYRO and GS2 shows that the discrepancies are reduced below 5%. Through this comparison, we conclude that the two data translators have similar performance and GYRO and GS2 agree with each other in the linear stability analysis.

Table 4-1: The key parameters prepared for GYRO with trgk and GS2 with GS2_prep from the same C-Mod ohmic plasma.

	GYRO (trgk)	**GS2 (gs2_prep)**
a/L_{Te}	3.446620	3.57882
a/L_{Ti}	3.604392	3.71603
a/L_{n_e}	0.849910	0.841439
a/L_{n_i}	0.849863	0.841445
T_i/T_e	0.385067	0.427924

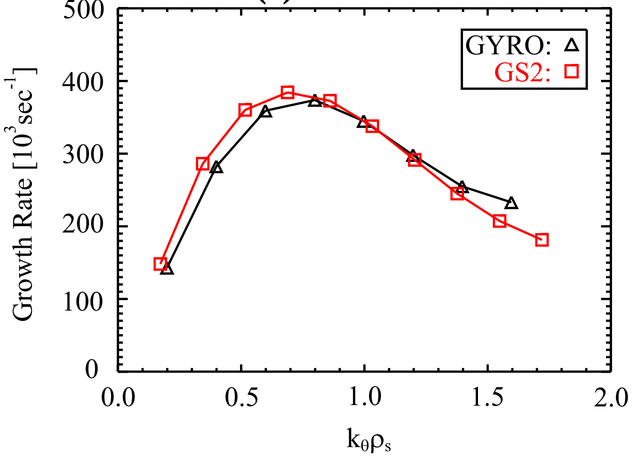
(a) Growth Rate

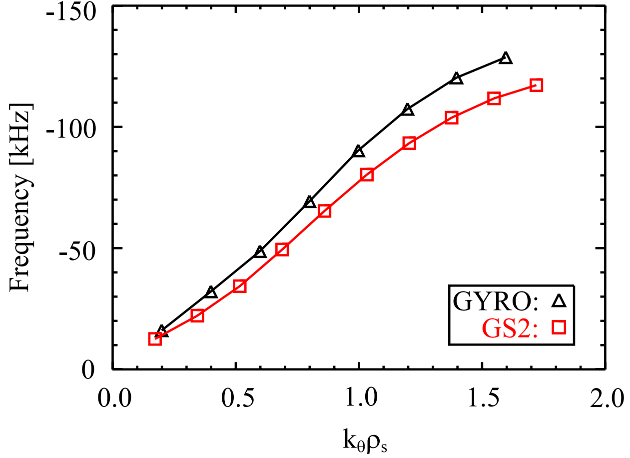
(b) Frequency

Figure 4-4: Comparison of linear stability analysis with GS2 and GYRO: (a) growth rate spectrum; (b) frequency spectrum.

4.2.2 Nonlinear Stability Simulation

There are two options for the nonlinear GYRO simulations: local and global modes. In a local simulation, each equilibrium profile and gradient is taken to have a fixed and independent value across the simulation box. This corresponds to the $\rho^* = \rho_s / a \rightarrow 0$ limit of global simulations and is similar to flux-tube simulations, where $\rho_s = c_s / \Omega_i$ is the ion-sound Larmor radius, $c_s = (T_e / m_i)^{1/2}$ is the ion sound speed, $\Omega_i = eB_\phi / m_i$ is the ion cyclotron frequency, and m_i is the ion mass. In a global simulation, GYRO uses spatially varying equilibrium profiles, which can be deduced from experimental or user-defined physical parameters.

A nonlinear GYRO uses N toroidal modes with separation Δn, e.g. $n = 0, 10, 20, 30, \cdots, 150$, which corresponds to simulate a wedge of $1/\Delta n$ of a tokamak. For example, the above example corresponds to simulating 1/10 of the torus, as shown in Fig. 4-5. In the local simulation, $q(r)/r$ is fixed, which gives an uniform coverage of k_θ. In a global simulation, $q(r)/r$ varies with radius, so the k_θ resolution also varies.

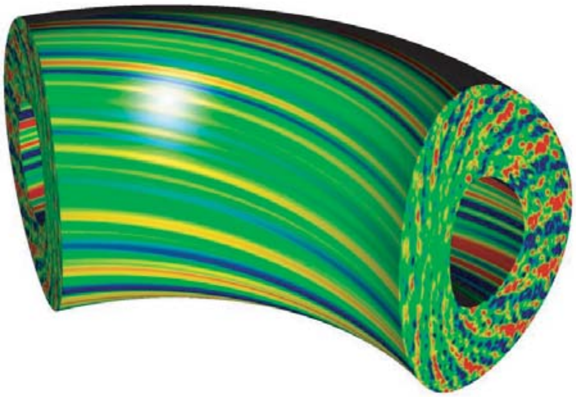

Figure 4-5: A wedge of tokamak in the nonlinear GYRO simulation.

The nonlinear GYRO simulation includes the proper nonlinear saturation mechanism and solves the gyro-averaged gyro-center distribution h. After h is resolved, the density fluctuation $\tilde{n}$, the temperature fluctuation $\tilde{T}$, and the potential fluctuation $\tilde{\phi}$ are calculated and recorded in the GYRO output. The thermal diffusivity χ is also calculated through the relationship,

$$\chi(r) = \left(-n\frac{dT}{dr}\right)^{-1} \int d^3 \upsilon \frac{m\upsilon^2}{2} \langle \tilde{\upsilon}_r \cdot h \rangle , \tag{4.19}$$

where $\tilde{\upsilon}_r$ is the fluctuating $\mathbf{E}\times\mathbf{B}$ drift velocity along the radial direction.

4.3 Synthetic Diagnostic

While comprehensive models and simulations have been developed to predict turbulence and transport in fusion plasmas, detailed experimental comparisons and validations remain as a challenge. This is partially caused by the limited diagnostic capability and access in fusion plasmas. For example, the phase contrast imaging (PCI) diagnostic in Alcator C-Mod[56] measures line-integrated electron density fluctuations with an instrumental limit primarily in the wavenumber space. To resolve this issue, a virtual diagnostic (known as the synthetic PCI diagnostic) originally developed for the DIII-D PCI diagnostic[91] has been adapted to the C-Mod PCI system. Essentially, the synthetic PCI diagnostic analyzes the electron density fluctuation output of a GYRO global nonlinear simulation and emulates the experimental PCI measurements. Therefore, it allows for direct comparisons between numerical simulations and experimental measurements.

GYRO outputs record the density fluctuation $\tilde{n}_j$ for each toroidal mode number n_j in a grid of (r,θ,t), which are combined to form physical quantities of density fluctuation $\tilde{n}$,

$$\tilde{n}(r,\theta,\phi,t) = \mathrm{Re}\sum_{j=0}^{N-1}\tilde{n}_j(r,\theta,t)\exp\left[-in_j\left(\phi+\nu\left(r,\theta\right)\right)\right]. \tag{4.20}$$

The synthetic PCI analyzes the GYRO output of electron density fluctuations and emulate the PCI measurement. It mainly consists of four steps:

- First, spacing chords over entire width of beam with several chords per detector channel and interpolating to calculate $\tilde{n}$ along the each chord. In the example shown in Fig. 4-6, 128 chords are spaced over the PCI beam, which corresponds to 4 chords per detector.
- Second, summing up $\tilde{n}$ along each chord to emulate the line-integration effect.
- Third, adding a high pass filter in the wavenumber space to model the PCI response.
- Last, combining chords over each detector channel to model the finite detector size effect.

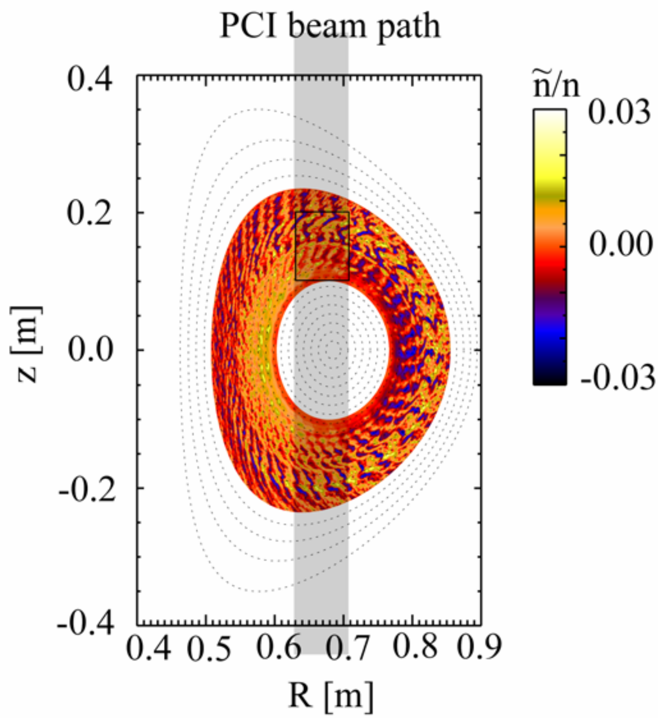

Figure 4-6: Implementation of the synthetic PCI diagnostic on the electron density fluctuations from a nonlinear GYRO simulation

After obtaining predicted PCI measurements, we can use the PCI data analysis routines to analyze them and compare results with experimental measurements. An example of synthetic PCI measurement is shown in Fig. 4-7. In this case, the unstable turbulence from GYRO is the ion temperature gradient (ITG) mode, which is propagating in the ion diamagnetic direction. As shown in Fig. 4-7(a), the probe laser beam lets of the PCI diagnostic are scattered by the turbulent waves at the top and bottom of the plasma column, where the turbulent wave propagates in opposite direction relative to the PCI beam, as shown in Fig. 4-7(a). The conventional PCI configuration measures the line-integrated density fluctuations and the measurement takes the form of

$$I_{\text{conventional PCI}} = \int \tilde{n}(z)\,dz\,. \tag{4.21}$$

Consequently, the synthetic spectra with the conventional PCI configuration are present in both positive and negative wavenumbers, as shown in Fig. 4-7(b). Therefore, the propagating direction of the measured turbulence waves cannot be resolved from the spectra. The localizing configuration described in Chapter 3 introduces a weighting function $w(z)$ in the line integration as,

$$I_{\text{Localizing PCI}} = \int w(z)\,\tilde{n}(z)\,dz\,. \tag{4.22}$$

In the longer wavelength regime in the ITG range, the localization is not as fine, but still allows for selection of the turbulence from the top or the bottom of the plasma, thereby resolving the direction of propagation. When adding the effect of the localizing configuration and setting the integration length to be only half of the column, only positive or negative wavenumber shows up on the synthetic PCI spectra. As shown in Fig. 4-7(c), the negative wavenumber dominates in the top-column integration ($z > 0$), while the positive wavenumber dominates in the bottom-column integration $z < 0$ (as shown in Fig. 4-7(d)). As we can see, the localizing system differentiates the contribution from the top and bottom to the PCI measurement, thereby resolving the dominant mode propagating direction. As we can see from this analysis, the synthetic PCI diagnostic not only helps validate numerical codes but also assists us to interpret turbulence measurements.

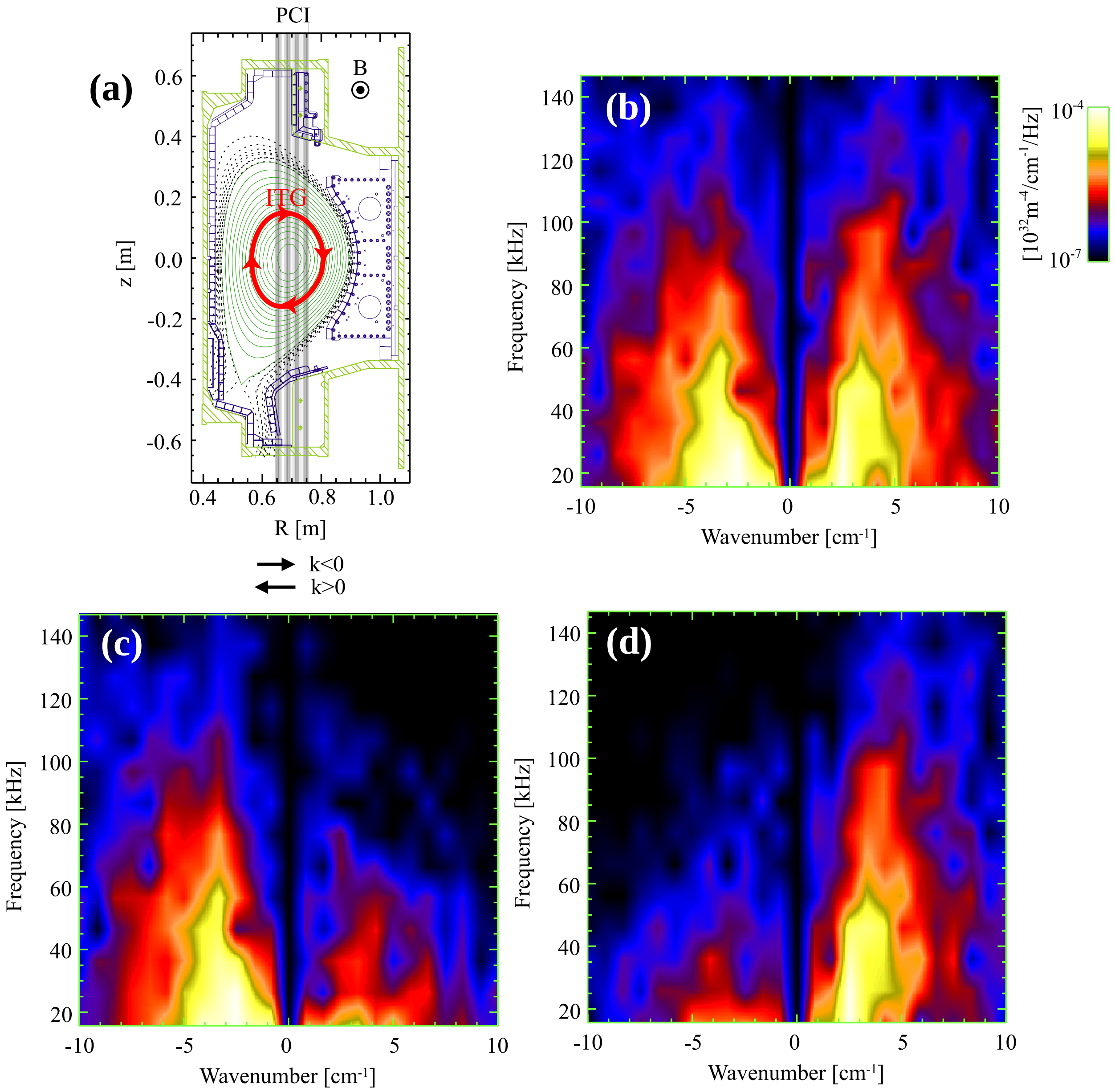

Figure 4-7: (a) The laser beam path of the Alcator C-Mod PCI diagnostics where the propagating direction of the ITG mode is also labeled. The sign convention of the wavenumber used in this thesis is also indicated. The positive wavenumber corresponds to the waves propagating toward high field side (HFS), while the negative wavenumber corresponds to the waves propagating toward the low field side (LHS); (b) The synthetic PCI spectra, where the line-integration is performed for all z; (c) The synthetic PCI spectra, where the line-integration is performed only for $z > 0$; (d) The synthetic PCI spectra, where the line-integration is performed only for $z < 0$.

4.4 Summary

Plasma turbulence and transport is a field which is necessarily linked to computational plasma physics. Better understanding of the underlying physics is closely connected to the development of better computational codes based on an improved theoretical framework and intensive validation against experiments. Owing to the two dimensional nature of turbulence and the non-localized aspects of nearly all diagnostics, a “synthetic” diagnostic technique must be implemented for any particular code if its predictions are to be compared to experimental measurements of turbulent fluctuations. Such a synthetic PCI diagnostic has been implemented in the GYRO code and is being used in the present studied. In the next two chapters, we will discuss the results of turbulence and transport studies with the phase contrast imaging diagnostic and will present comparisons with GYRO predictions.

Chapter 5

Turbulence and Transport Studies in Ohmic Plasmas

5.1. Introduction

Early experiments in the Alcator C tokamak observed the “neo-Alcator” scaling of confinement in ohmically heated plasmas, where the energy confinement time (τ_E) is proportional to the line-averaged electron density ($\overline{n}_e$).[92] This linear scaling has also been observed in many other plasmas devices.[93] As the density increases, τ_E saturates and shows a weak dependence on $\overline{n}_e$. This saturation of confinement was interpreted as evidence of the importance of unstable ion temperature gradient (ITG) turbulence when the ion and electron channels are coupled by collisions at higher densities.

Previous studies in the Texas Experimental Tokamak (TEXT) [94] and DIII-D [95] presented experimental evidence for the ITG turbulence in the saturated ohmic regime. Although some nonlinear turbulence calculations were based on the DIII-D conditions, there were no quantitative comparisons of simulated and measured turbulence. In addition, the physics of the neo-Alcator scaling in the linear ohmic regime, where the electron transport dominates, is still not well-understood. A few theoretical transport models based on the finite-β_e universal-mode turbulence[96], the principle of profile consistency[97], or the extreme dissipative trapped electron

(DTE) transport scaling [98-100] show a linear relationship between the confinement time and electron density. The theoretical modeling of TEXTOR plasmas suggests the linear ohmic regime is dominated by the dissipative trapped electron mode (TEM), while the saturated ohmic regime is dominated by the ITG mode.[101-104] This interpretation is consistent with the fact that the TEM is stabilized by higher collisionality at a higher density, while the ITG mode is only weakly affected by collisionality. An analogous analysis in ASDEX Upgrade provides results consistent with the above interpretation.[105] Moreover, turbulence measurements in ASDEX Upgrade indicate a transition from TEM to ITG as collisionality increases.[106] However, complete nonlinear gyrokinetic simulations are still necessary for a more quantitative comparison between theory and experiment. As a result, revisiting these ohmic plasmas with experimental turbulence measurements and advanced gyrokinetic simulations is essential in quantitatively understanding electron transport, as well as validating the numerical codes.

In this chapter, we report the numerical and experimental studies of turbulence and transport in Alcator C-Mod ohmic plasmas. The phase contrast imaging (PCI) diagnostic[56,61] is used to measure the turbulent density fluctuations. Recent advances in gyrokinetic simulation allow us to quantitatively simulate core turbulence and associated transport.[80-85] Moreover, the development of a synthetic PCI diagnostic[91] for GYRO allows for direct and quantitative comparisons between the PCI measurements and numerical predictions. The plasma regimes studied cover both the linear and saturated ohmic regimes, with the goal of resolving a longstanding mystery in transport physics in tokamaks.

This chapter is arranged as follows: in Section 5.2, the discharges under study are overviewed; in Section 5.3, the transport analysis with TRANSP is discussed; in Section 5.4, the fluctuation measurements are presented; in Section 5.5, a direct and quantitative comparison is given between fluctuation measurements and GYRO predictions; in Sec. 5.6, a comparison in transport is given between GYRO simulation and TRANSP calculation; in Section 5.7, a further investigation of the low density plasma in the linear ohmic regime is discussed. Finally, in Sec. 5.8 the conclusions are presented.

5.2. Target Plasma Parameters

Our experiments were carried out over a range of densities in the Alcator C-Mod Tokamak[107] covering the "neo-Alcator" (also known as “linear ohmic”) to the "saturated ohmic" regime. As shown in Fig. 5-1, when the line-averaged electron density ($\overline{n}_e$) is below $0.7\times10^{20}\ \mathrm{m}^{-3}$, the global confinement time (τ_E) is linearly proportional to the line-averaged density, i.e. $\tau_E \propto \overline{n}_e$. After $\overline{n}_e$ increases above $0.8\times10^{20}\ \mathrm{m}^{-3}$, τ_E saturates and shows a weaker dependence on $\overline{n}_e$. The experiments were conducted with the on-axis toroidal magnetic field (B_ϕ) at 5.2 T, the plasma current (I_p) at 0.8 MA, and q_{95} at 4.4. The magnetic field configuration is the normal field lower single null (LSN) with the lower triangularity $\delta_l \simeq 0.5$, the upper triangularity $\delta_u \simeq 0.3$, and the elongation $\kappa \simeq 1.6$.

Statistical uncertainty in the data analysis and processing is reduced by using large data sets from relatively steady and reproducible discharges. All the data, including the plasma equilibria and fluctuation measurements used in this chapter, are averaged over the steady phase (~0.4 sec) of the discharge as shown in Fig. 5-2. The electron density (n_e) and temperature (T_e) profiles are shown in Fig. 5-3, where the smoothed profiles are obtained by fitting the experimental measurements from the Thomson scattering (measuring n_e and T_e) and electron cyclotron emission (measuring T_e) diagnostics[108] with a B-spline function. These smoothed profiles are used in the following transport analysis and gyrokinetic simulation.

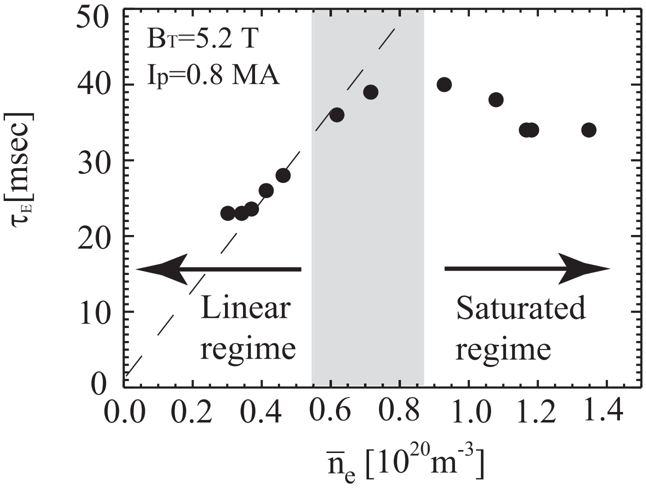

Figure 5-1: Energy confinement time τ_E versus line-averaged density $\overline{n}_e$. The shaded region represents the transition between the linear ohmic and saturated ohmic regime.

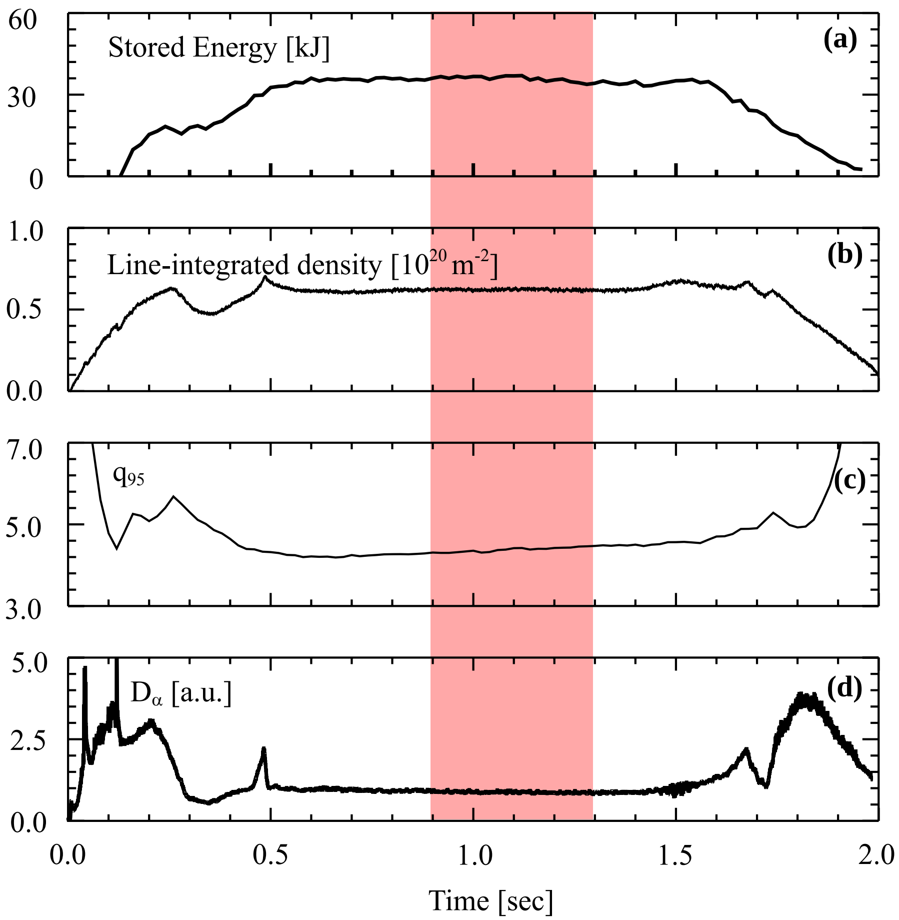

Figure 5-2: Plasma parameters for the discharge at $\overline{n}_e = 0.93\times10^{20}\ \text{m}^{-3}$: (a) store energy; (c) line-integrated electron density; (d) q_{95}; (d) D_α light. The shade region shows the time window where the data averaging is performed.

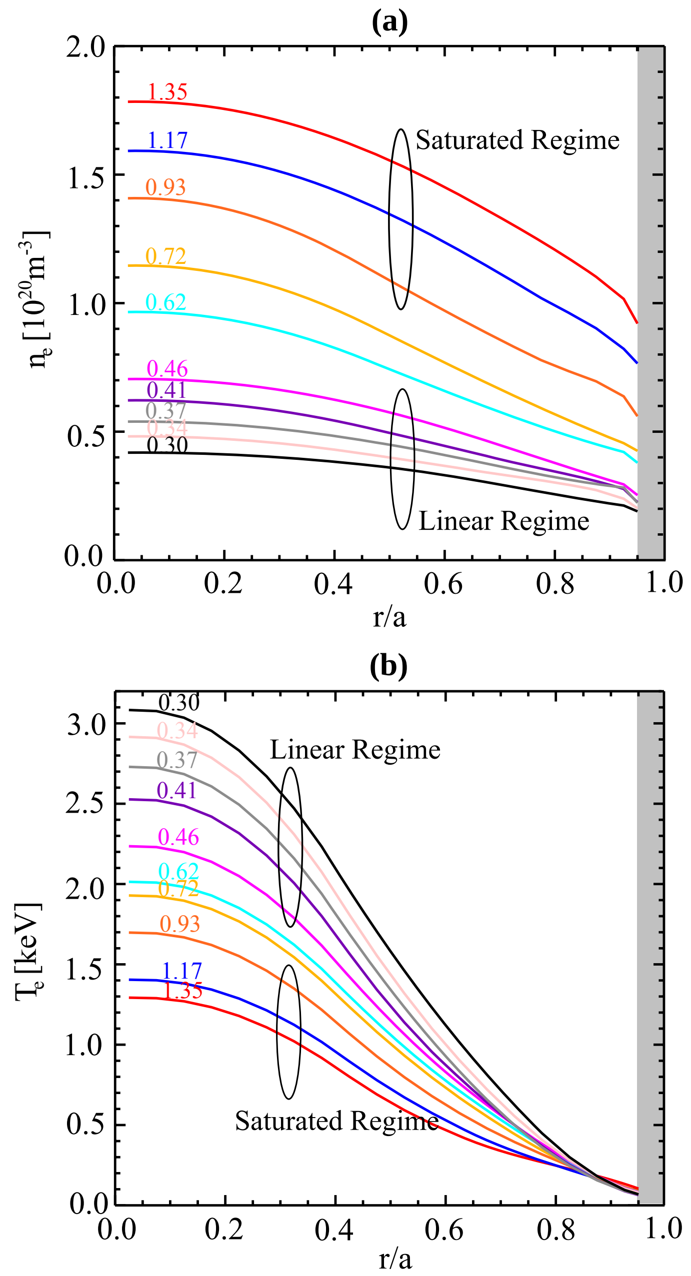

Figure 5-3: Electron density (a) and temperature (b) profiles at different densities, where the line-averaged density $\overline{n}_e$ in the unit of 10^{20} m^{-3} of each profile is labeled.

5.3. Transport Analysis with TRANSP

In our studies, the thermal transport characteristics are determined using the TRANSP[89] code, which calculates the local thermal diffusivities from the energy balance equations. TRANSP is also used to determine those unmeasured plasma parameters, such as ion temperature profiles, which are necessary in the gyrokinetic simulation. In Alcator C-Mod, the high resolution X-ray spectrometer (Hirex)[109] was used to measure ion temperature profiles but these measurements were not always available. Thus, the ion temperature profiles used here are calculated from the neutron measurement. TRANSP uses experimental electron density and temperature profiles and a multiplier on the electron diffusivity χ_e to obtain an ion temperature profile consistent with from the neutron measurement[110]. This modeling is based on two assumptions: first, the ion temperature profile is Gaussian with a width similar to that of the electron temperature profile; second, the ion density is calculated from the electron density using a flat Z_{eff} profile. Here, the plasma is assumed to consist of three species: electron, deuterium, and one impurity species; thus, Z_{eff} can be expressed as

$$Z_{eff} = \frac{n_i + n_I Z_I^2}{n_e}, \tag{5.1}$$

where n_i is the deuterium density, n_I is the impurity density, and Z_I is the atomic number of the impurity. In the TRANSP analysis presented in this chapter, Z_{eff} is calculated from the neoclassical resistivity[111]. The calculated Z_{eff} is shown in Fig. 5-4, where Z_{eff} decreases as density increases. As an exaple, the modeled ion temperature profile at $\bar{n}_e = 0.34\times10^{20}\ \mathrm{m}^{-3}$ is shown together with the measured electron temperature profle in Fig. 5-5.

To estimate the uncertainty of the modeled ion temperature T_i and its gradient ∇T_i, the calculated Z_{eff} and measured neutron rate is varied by ±15%. The resulting changes of the modeled T_i and ∇T_i are as much as 10% and 30%, respectively. The resulting change on the dimensionless parameter $a/L_{Ti} = -(a/T_i)(dT_i/dr)$ is as much as 30%.

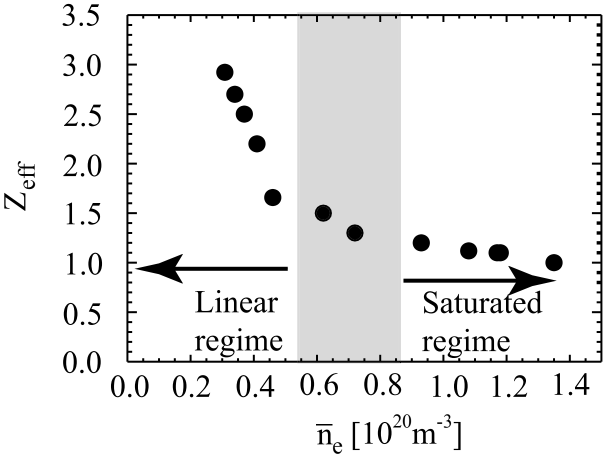

Figure 5-4: Z_{eff} calculated from the neo-neoclassical resistivity versus line-averaged $\bar{n}_e$. The shaded region represents the transition between the linear ohmic and saturated ohmic regime.

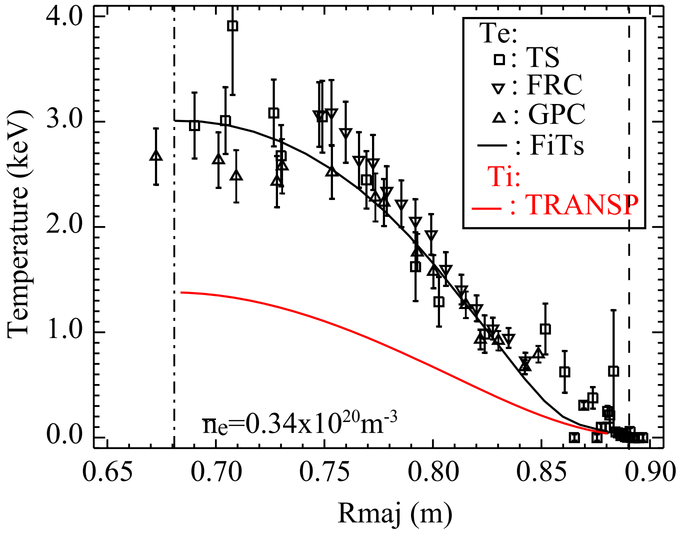

Figure 5-5: Electron and ion temperature profiles at $\bar{n}_e = 0.34 \times 10^{20}$ m^{-3}. The electron temperature profile is measured by the Thompson scattering (TS) and two ECE diagnostics (FRC and GPC). The solid line is a fit to the experimental measurements using FiTs. The ion temperature profile is obtained from the TRANSP modeling to match the neutron measurement. Two vertical dashed lines are the magnetic axis and the last closed flux surface (LCFS), respectively.

Regarding the density gradient, typical experimental uncertainty of the Thompson scattering (TS) measurement is ~15% as shown in Fig. 5-6. Thus, the estimated uncertainty of ∇n_e is ~30%.

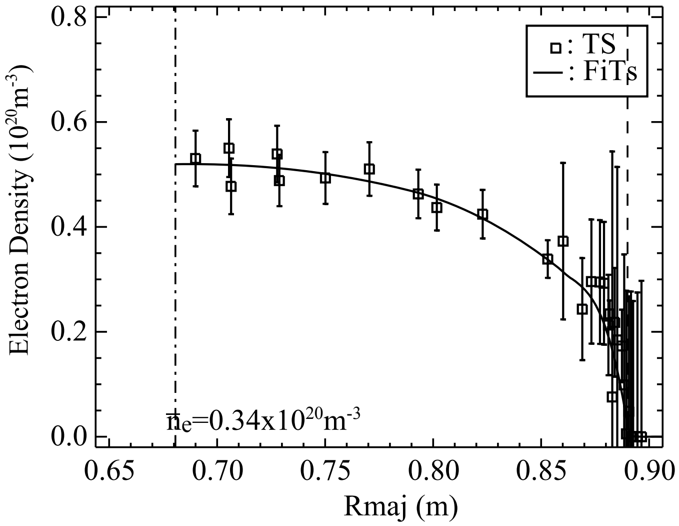

Figure 5-6: Electron density profile $\bar{n}_e = 0.34\times10^{20}$ m^{-3} from the Thomson scattering (TS) diagnostic. The solid line is a fit to the experimental measurements using FiTs. Two vertical dashed lines are the magnetic axis and the last closed flux surface (LCFS), respectively.

Approaching the center of the plasma column, the heat flux goes to zero, which implies that the temperature gradient goes to zero, i.e. $\nabla T \to 0$. Consequently, it is difficult to compute the thermal diffusivity (χ), since $\chi \propto 1/\nabla T$. Near the plasma edge, the errors in the electron density and temperature profiles are especially large. Therefore, the focus of the TRANSP analysis is the plasma core, which is taken to be in the range of $r/a \in [0.2, 0.8]$ in this chapter. The thermal diffusivities from the TRANSP analysis at low ($\bar{n}_e = 0.34\times10^{20}$ m^{-3}), medium ($\bar{n}_e = 0.62\times10^{20}$ m^{-3}), and high ($\bar{n}_e = 0.93\times10^{20}$ m^{-3}) density plasmas are shown in Fig. 5-7. The lowest density plasma corresponds to the linear ohmic regime where τ_E is linearly proportional to $\bar{n}_e$. The highest density plasma corresponds to the saturated ohmic regime where

τ_E is saturated. The medium density plasma represents the transition from the linear to saturated ohmic regime. As the density increases, the electron thermal diffusivity χ_e decreases, but the ion thermal diffusivity χ_i increases slowly; the effective thermal diffusivity

$$\chi_{eff} \equiv \frac{n_e \chi_e \nabla T_e + n_i \chi_i \nabla T_i}{n_e \nabla T_e + n_i \nabla T_i} \tag{5.2}$$

also decreases. We also note that χ_i is much lower than χ_e in the linear ohmic regime and becomes comparable to χ_e in the saturated ohmic regime. This indicates that the electron and ion transport channels are decoupled at low densities and the ohmic powers are mainly lost through the electron channel.

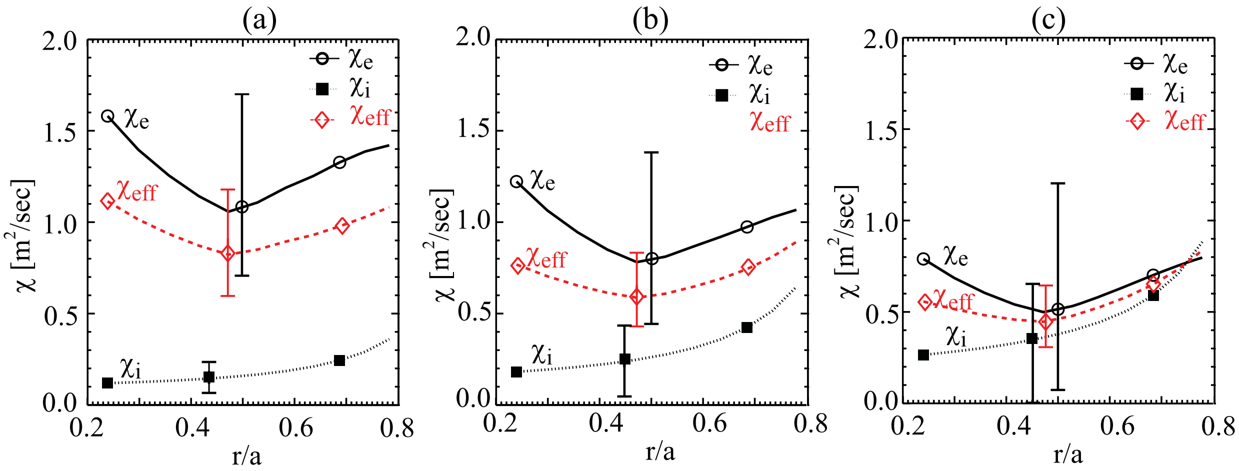

Figure 5-7: TRANSP calculated thermal diffusivities for ohmic plasmas at the line-averaged density of (a) $\bar{n}_e = 0.34\times10^{20}$ m^{-3}, (b) $\bar{n}_e = 0.62\times10^{20}$ m^{-3} and (c) $\bar{n}_e = 0.93\times10^{20}$ m^{-3}.

5.4. Fluctuation Measurements

To study the change in turbulent transport as the density varies in ohmic plasmas, it is of great importance to measure the change in turbulent fluctuations. In Alcator C-Mod, the phase contrast imaging (PCI) diagnostic has been used to monitor these fluctuations. The frequency spectra of a single chord PCI measurement are shown in Fig. 5-8, where the density fluctuation intensity decays as the frequency increases. A linear fit

$$\log P_f = -A_f \log f + B_f \tag{5.3}$$

is used to estimate the decay rate, where P_f is the fluctuation intensity of the frequency spectra. As shown in Fig. 5-9, The decay rate in the lower frequency range of 20-80 kHz, where $A_f \approx 1.5 \pm 0.3$, is smaller than that in the higher frequency range of 100-250 kHz, where $A_f \approx 4.2 \pm 0.7$, depending on densities. We also note a knee exists in the frequency spectrum when the density is above $0.7 \times 10^{20}\,\mathrm{m}^{-3}$. As the density decreases, the location of this knee in frequency tends to move toward higher frequency. However, the knee feature becomes less pronounced when the density is below $0.7 \times 10^{20}\,\mathrm{m}^{-3}$. Currently, the cause and influence of this feature is not well understood.

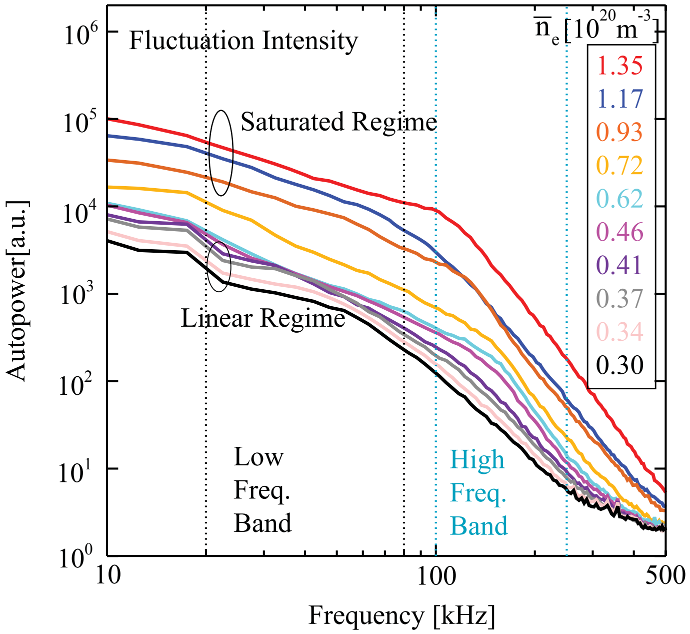

Figure 5-8: Frequency spectra of a PCI core channel (14) at different densities. The spectra are averaged over 400 ms and shown with a 5 kHz frequency resolution.

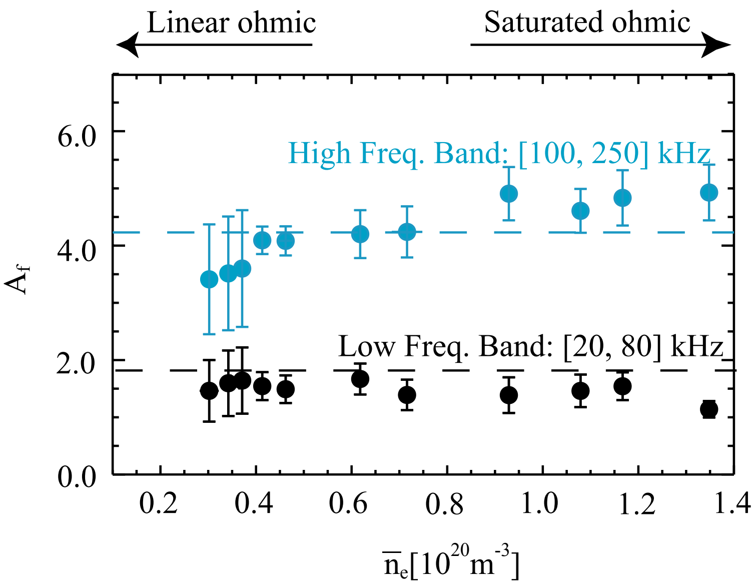

Figure 5-9: Linear fit parameter A_f vs. line-averaged density $\bar{n}_e$, where the fitting is performed in the low frequency range of 20-80 kHz and the high frequency range of 100-250 kHz, respectively. A_f has a weak dependence on $\bar{n}_e$.

In the studies presented in this chapter, the PCI system is set to view preferentially the bottom of the plasma column. According to the sign convention of wavenumbers shown in Fig. 5-10, the positive wavenumbers correspond to turbulent waves propagating in the ion diamagnetic direction, while the negative wavenumbers correspond to turbulent waves propagating in the electron diamagnetic direction. Figure 5-10 shows the frequency/wavenumber spectra of the PCI measurement at $\overline{n}_e = 0.93\times10^{20}\ \mathrm{m}^{-3}$ in the saturated ohmic regime. The measurement shows that the fluctuations in the higher frequency range of 80-250 kHz propagate in the ion diamagnetic direction in the laboratory frame, where the experimentally measured frequency (f_{lab}) equals to the mode frequency (f_{mode}) plus the Doppler shift due to E×B drift velocity ($f_{\mathrm{E\times B}}$), i.e. $f_{\mathrm{lab}} = f_{\mathrm{mode}} + f_{\mathrm{E\times B}}$. Although the radial electric field is not well measured for the considered plasmas, the available measurements indicate that the background Doppler rotation is not enough to reverse the mode propagating direction of the turbulence with the wavenumbers in the ITG and TEM regime. Therefore, this measurement also shows that the fluctuations in the higher frequency range of 80-250 kHz propagate in the ion diamagnetic direction in the plasma frame.

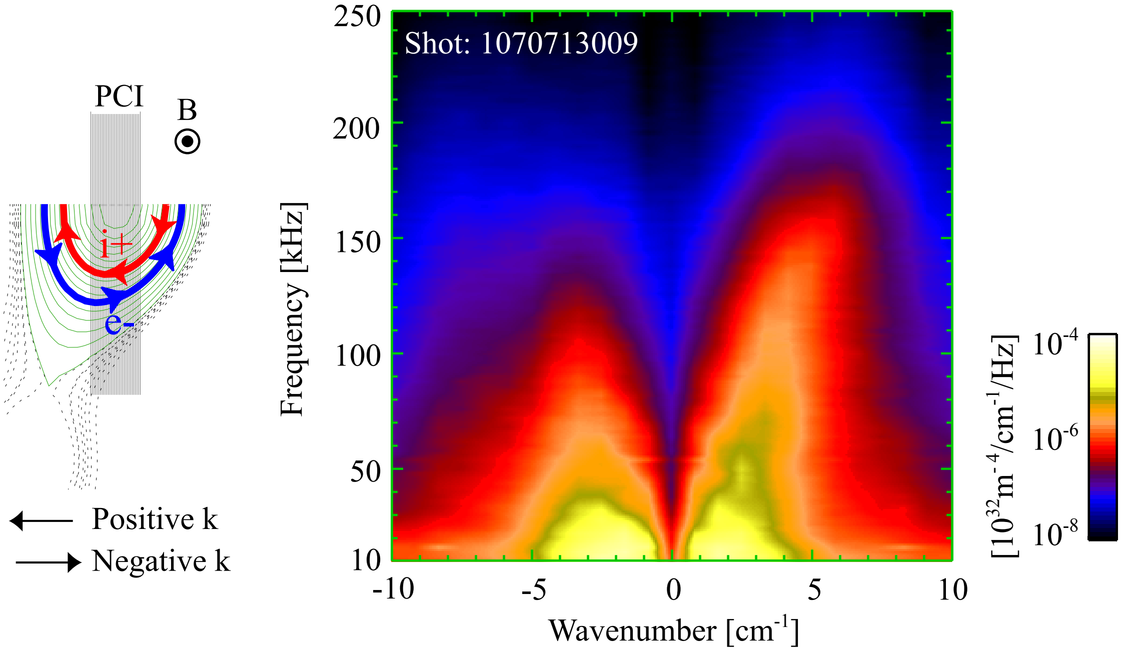

Figure 5-10: Frequency/wavenumber spectra of the PCI measurement at $\overline{n}_e = 0.93\times10^{20}$ m^{-3} in the saturated ohmic regime. The PCI diagnostic is set to preferentially view the bottom plasma.

It is very tempting to seek correlation between the overall fluctuation intensities measured by PCI and the global confinement time. The PCI measurements can be normalized to the line-integrated density for an estimated fluctuation level. The results are shown in Fig. 5-11. Here the normalized density fluctuation is shown in arbitrary units, since we only focus on its variation as the density changes. Currently, the experimental error of the PCI measurements mainly comes from the uncertainty of calibration, which provides a conversion factor to express fluctuation intensity ($\left|\int \tilde{n}_e dl\right|^2$) in the scale of m^{-4}. When the measurements are expressed in the real scale, the uncertainty is +/-60%. However, when the comparison is performed in arbitrary units between measurements with the same diagnostic performance, the uncertainty is typically below 10%. In the linear ohmic regime $\overline{n}_e \lesssim 0.7\times10^{20}$ m^{-3}, as shown in Fig. 5-11(a), the relative density fluctuation intensity in the frequency range of 20-80 kHz decreases as density increases;

this shows some correlation with the confinement time scaling where $\tau_E \propto \overline{n}_e$. However, there is no significant difference for relative density fluctuation in the electron and ion diamagnetic direction. This suggests that the PCI measurement below 80 kHz might be localized at the plasma edge, where the turbulence propagating in the ion and electron diamagnetic directions may be comparable. An alternative explanation is that low frequency modes coming from the plasma core and the edge are mixed together in a way that we cannot separate them. The masked PCI has resolved that fluctuations above 80 kHz are dominated by the mode propagating in the ion diamagnetic direction in both the linear and saturated ohmic regimes, as shown in Fig. 5-11(b). This dominance becomes more apparent in the saturated ohmic regime as density increases, which indicates that ITG becomes more significant as density increases when electrons and ions are more coupled.

We also want to point out that the above comparison between the estimated density fluctuation level and confinement time as the density varies is limited for two reasons. First, PCI measures line-integrated electron density fluctuations (including both plasma core and edge) and phase cancellation might be important in the line-integration of density fluctuations, which makes it difficult to directly relate the PCI measurement to the local transport. Second, since turbulence-driven transport also depends on other unknown plasma parameters and their correlations (such as potential and temperature fluctuations), large density fluctuations do not always correspond to large thermal transport. To provide better understanding of experimental measurements, we have also simulated turbulence with the GYRO code[85-86], which quantitatively relates the fluctuation spectra to transport.

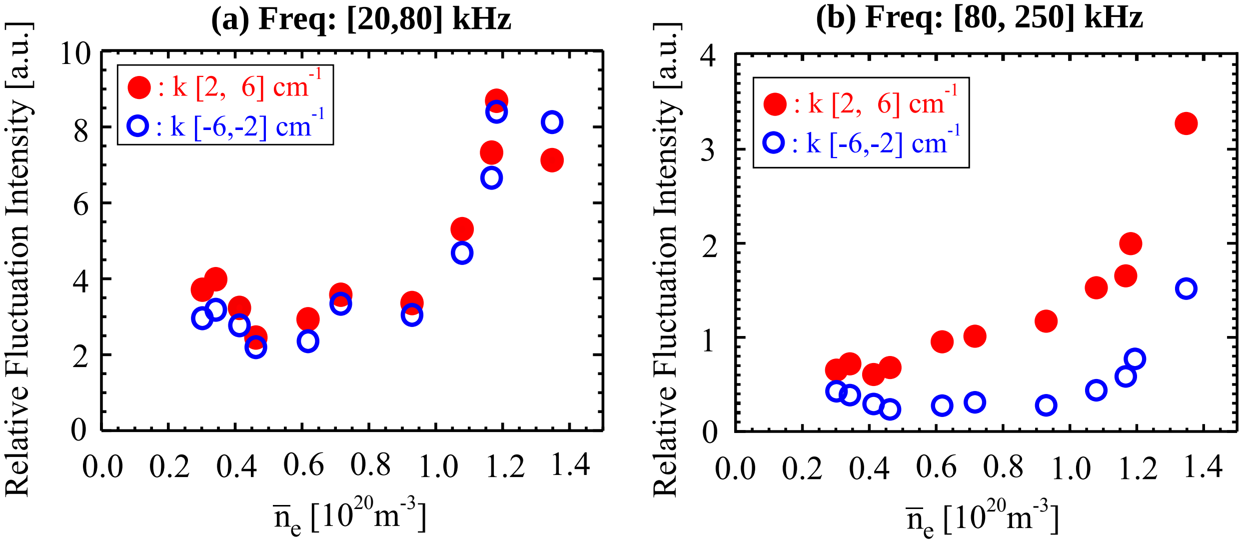

Figure 5-11: Relative density fluctuation intensity level vs. the line-averaged density (red dot: integrated over the wavenumber range of $[2, 6]\,\mathrm{cm}^{-1}$, corresponding to the mode propagating in the ion diamagnetic direction for the preferentially bottom view configuration of PCI; blue open circle: integrated over the wavenumber range $[-6, -2]\,\mathrm{cm}^{-1}$ corresponding to the mode propagating in the electron diamagnetic direction for the preferentially bottom view configuration of PCI) (a) integrated over the frequency range of 20-80 kHz; (b) integrated over the frequency range of 80-250 kHz.

5.5 Turbulence Studies with GYRO

To further explore the nature of turbulence and the drive mechanism of thermal transport, we have used GYRO to simulate turbulence and transport. GYRO is a physically comprehensive global code which solves the nonlinear 5-D gyrokinetic-Maxwell equations for both ions and electrons in a local (flux-tube) or 'global' radial domain[85]. The input file is prepared from the output of TRANSP using the data translator (trgk) developed at PPPL. The electrostatic approximation is assumed for all the simulations presented in this chapter, since we verified that the contributions from electromagnetic fluctuations are negligible in our simulation of the low-β C-Mod plasmas.

It is apparent that the unprocessed simulated density fluctuations cannot be directly compared with the PCI measurements, since PCI measures the line-integrated density fluctuations and is heavily influenced by the phase cancellations. Furthormore, variations of plasma profiles along the integrating line are important. This makes the synthetic PCI crucial when comparing simulations with experimental measurements. As discussed in Chapter 4, the synthetic PCI post-analyzes the output of the global GYRO simulations and emulates the PCI measurements by line-integrating the electron density fluctuations along the PCI beam path, where the system response is also included. After obtaining a synthetic PCI signal, the same analysis package as the experimental data is used for spectral analysis.

All simulations in this chapter are performed with the real mass ratio ($m_i / m_e \approx 3600$) and kinetic electrons. Unless otherwise specified, the nonlinear global GYRO simulations in this chapter include 16 modes evenly spaced between $0.0 \lesssim k_\theta \rho_s \lesssim 1.0$ and cover the plasma domain of $0.4 \lesssim r/a \lesssim 0.8$, where k_θ is the wavenumber in the poloidal direction, $\rho_s = c_s / \Omega_i$ is the ion-sound Larmor radius, $c_s = (T_e / m_i)^{1/2}$ is the ion sound speed, $\Omega_i = eB_\phi / m_i$ is the ion cyclotron frequency, and m_i is the ion mass.

Figure 5-12 shows the synthetic PCI spectra from the GYRO simulation of the plasma at $\overline{n}_e = 0.93\times10^{20}\ \mathrm{m}^{-3}$ in the saturated ohmic regime. As shown in Fig. 5-12(a) where the Doppler shift corresponding to the average poloidal flow is not accounted for, the fluctuation with the positive wavenumber dominates, consistent with the ITG turbulence. Here, an average poloidal flow $\mathrm{v}_{\mathrm{E\times B}} = 2$ km/sec is chosen to match the phase velocity of the broadband turbulence above 80 kHz in the PCI measurements; this value is within the uncertainty of the available measurements. This value corresponds to $E_r \simeq 10$ kV/m , which gives a typical Doppler shifted frequency of ~ 64 kHz for $k_\theta \sim 2\ \mathrm{cm}^{-1}$. With the assumed Doppler shift the synthetic spectra, as shown in Fig. 5-12(b), are similar to the experimental measurement (see Fig. 5-10).

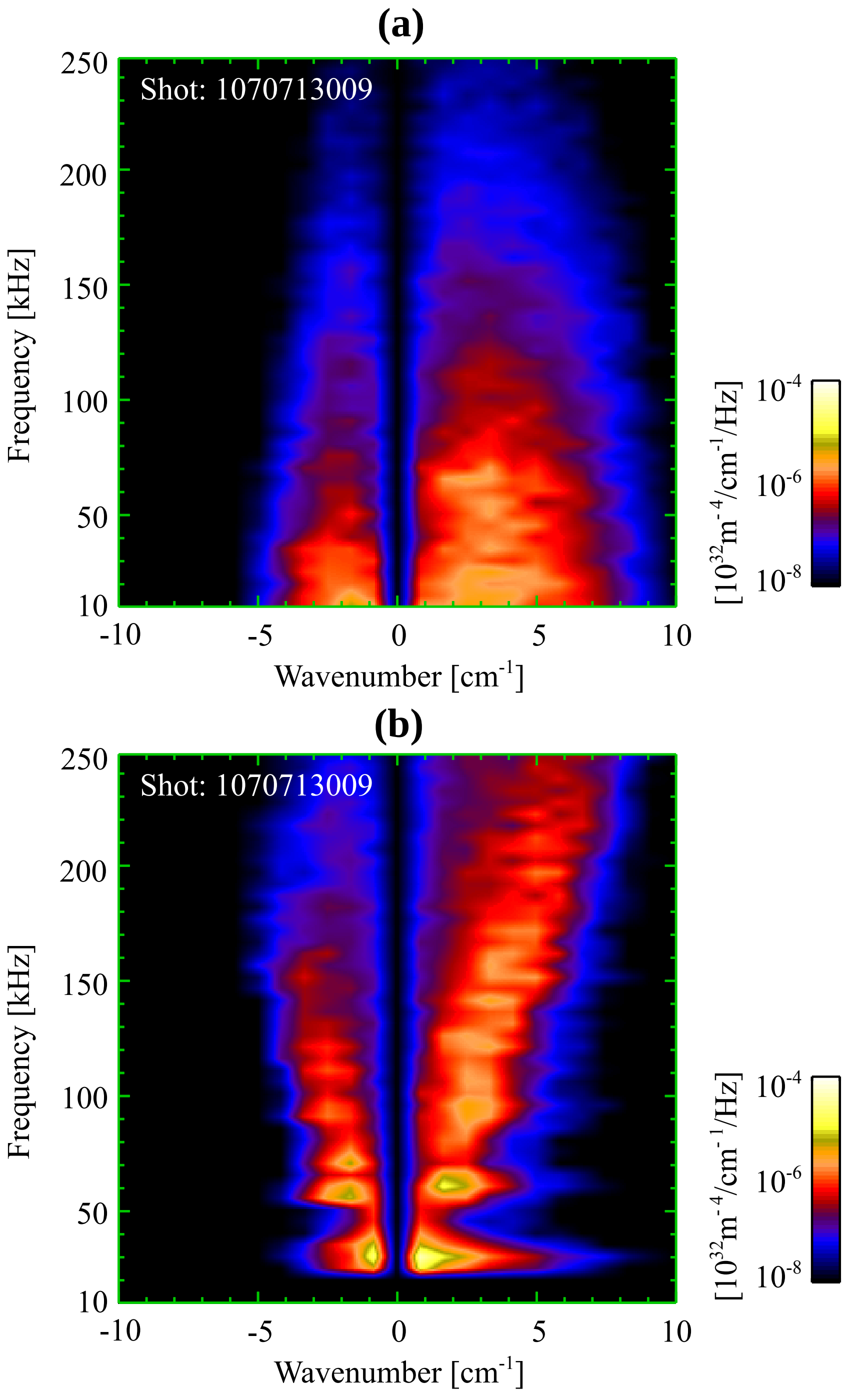

Figure 5-12: Synthetic PCI spectra at $\overline{n}_e = 0.93\times10^{20}\ \mathrm{m}^{-3}$: (a) no Doppler shift; (b) adding $\mathrm{v}_{\mathrm{E\times B}} = 2\ \mathrm{km/sec}$ to account for Doppler shift.

It is useful to integrate the frequency/wavenumber spectra (as shown in Fig. 5-12b) over a frequency range for a quantitative comparison between experiments and simulations. The integrating frequency range is chosen to be 80-250 kHz, where the PCI measurement is dominated by the core turbulence (see Sec. 5.4). As shown in Fig. 5-13, the wavenumber spectrum of density fluctuations in 80-250 kHz quantitatively agrees with GYRO simulation in the core ($0.4 \lesssim r/a \lesssim 0.8$). The convergence studies with different mode grid number N_n and toroidal mode separation Δn are shown in Fig. 5-13(a): (1) $N_n = 16$, $\Delta n = 10$; (2) $N_n = 10$, $\Delta n = 12$; (3) $N_n = 20$, $\Delta n = 10$. These simulations agree with experimental measurements within the experimental uncertainty (+/-60%). The simulations with different ion temperature profiles at $\overline{n}_e = 0.93 \times 10^{20}$ m^{-3} are shown in Fig. 5-13(b). Three ion temperature profiles are used: (1) Modeled T_i with TRANSP to match the neutron measurement; (2) $T_i = 0.8 \times T_e$; (3) $T_i = T_e$. The simulated wavenumber spectra with different ion temperature profiles all agree with each other, as well as experimental measurements.

The measured turbulence in the 50-80 kHz range propagates in the ion diamagnetic direction (see Fig. 5-10). After including the contribution of turbulence in the 50-80 kHz range, the simulated wavenumber spectra in the core ($0.4 < r/a < 0.8$; Fig. 5-12b) still agrees with the measured spectra within the experimental uncertainties (+/-60%) although the agreement is not as good as in Fig. 5-13. However, the PCI is a line-integrated density fluctuation diagnostic, where both core and edge turbulence contributes to the measured spectra. The induced ExB Doppler shift is relatively smaller since the turbulence in the 50-80 kHz range has lower wavenumbers than those above 80 kHz (see Fig. 5-10); thus, the core turbulence below 80 kHz is still mixed together with the edge turbulence.

Simulations of ohmic plasmas at other densities and similar analysis have been carried out. The same $\mathrm{v_{E\times B}} = 2$ km/sec is assumed to account for the Doppler shift. Figure 5-14(a) shows the comparison at $\overline{n}_e = 0.62\times10^{20}$ $\mathrm{m^{-3}}$. Figure 5-14(b) shows the comparison at $\overline{n}_e = 0.34 \times10^{20}$ $\mathrm{m^{-3}}$ in the linear ohmic regime. It is found that, at lower densities, similar spectral shapes were obtained but with progressively lower intensities. A summary of the results as a function of density is shown in Fig. 5-15, where the integrated density fluctuation intensities in the frequency range of 80-250 kHz are quantitatively consistent with a series of GYRO global simulations.

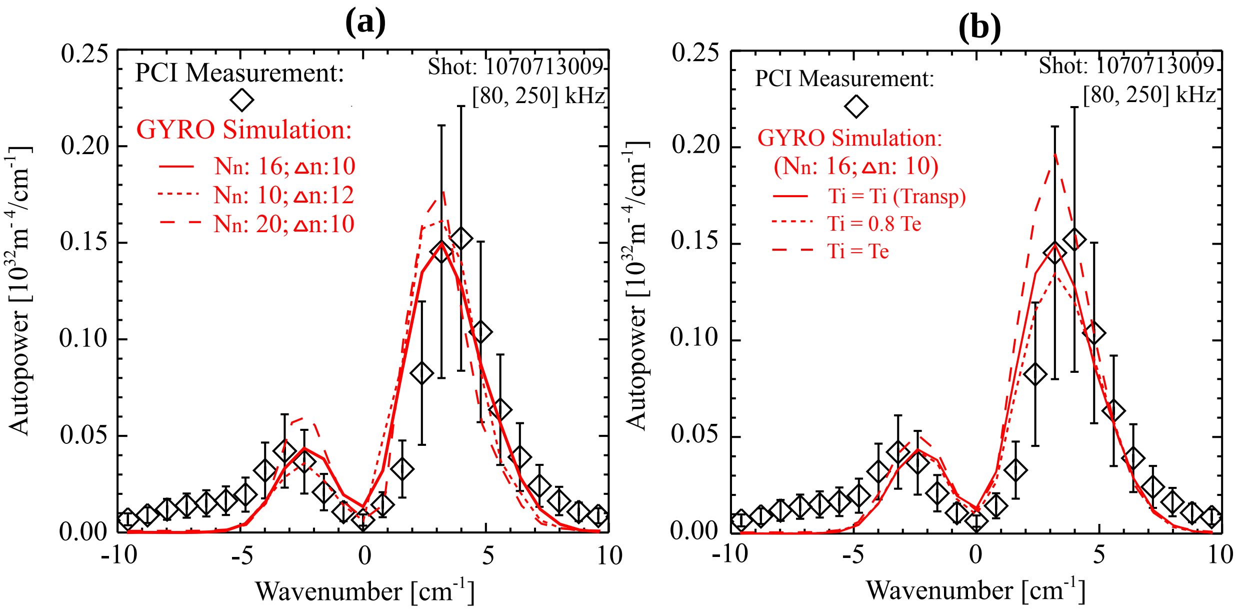

Figure 5-13. (a) Comparison of PCI measurements with GYRO simulations with different set of toroidal mode numbers at $\bar{n}_e = 0.93\times10^{20}$ m^{-3} in the saturated ohmic regime. (b) Comparison of PCI measurements with GYRO simulations with different ion temperature profiles at $\bar{n}_e = 0.93\times10^{20}$ m^{-3} in the saturated ohmic regime.

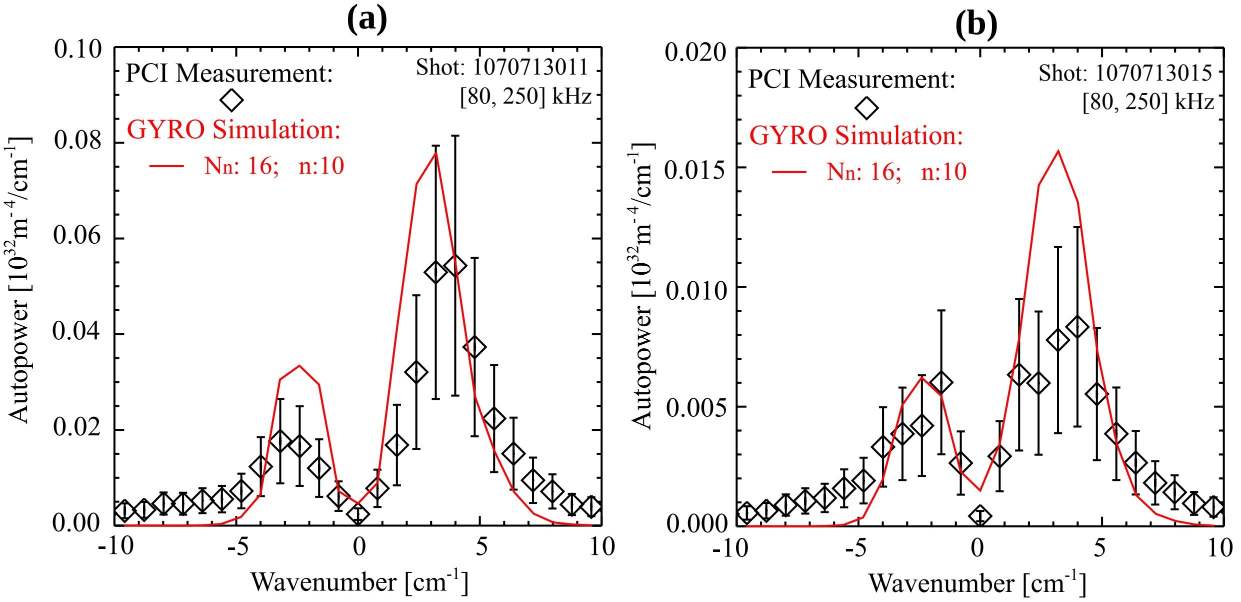

Figure 5-14. Comparison between the experimental and synthetic PCI wavenumber spectra in 80-250 kHz: (a) at $\bar{n}_e = 0.62\times10^{20}$ m^{-3} in the transition from the linear to saturated ohmic regime; (b) $\bar{n}_e = 0.34\times10^{20}$ m^{-3} in the linear ohmic regime.

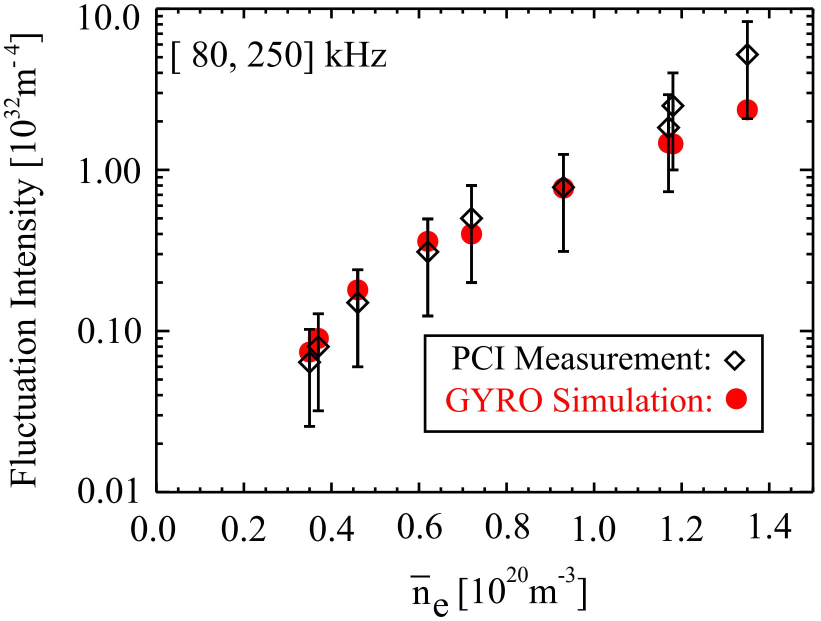

Figure 5-15: Comparison of the simulated fluctuation intensity ($|\int \tilde{n}_e dl|^2$) in the frequency range of 80-250 kHz with experimental measurements at various densities, where the fluctuation intensity is shown in the scale of 10^{32}m^{-4}. Comparison the simulated fluctuation intensity with experimental measurements at varies densities.

For the line-integrated fluctuation measurements, the background density is characterized by a profile instead of a constant. Thus, it is difficult to relate the PCI measurements to the local relative fluctuation intensity. However, it is still tempting to deduce the density fluctuation level ($\tilde{n}_e / n_e$) from the fluctuation intensity ($\left|\int \tilde{n}_e dl\right|^2$) as shown in Fig. 5-15 through $\tilde{n}_e / n \sim \left|\int \tilde{n}_e dl\right| / (\bar{n}_e L)$. Considering a reasonable integration length of $L \sim 5$ cm, we find that $\tilde{n}_e / n \sim 0.2\%$ (see Fig. 5-15). However, the deduced $\tilde{n}_e / n_e$ through the above approaches does not provide the right local value of $\tilde{n}_e / n_e$ or contain meaningful physics. The reasons are twofold. First, the PCI diagnostic measures the line-integrated density fluctuation. The phase cancellation during the line-integration will cause $|\int \tilde{n}_e dl| < \int |\tilde{n}_e|\, dl|$. Thus, the actual value of $\tilde{n}_e / n_e$ is likely to be much larger than the estimated one. Second, the integrating frequency band in Fig. 5-15 is selected to be 80-250 kHz, where the measured fluctuations are dominated by the core-localized turbulence. A proper calculation of $\tilde{n}_e / n_e$ should include the contribution of the fluctuations below 80 kHz. However, the measured fluctuations below 80 kHz are mixed together with the edge-localized turbulence and therefore the core contribution cannot be properly distinguished. However, we can state from the GYRO simulations that locally, $\tilde{n}_e / n_e \sim 1-3\%$ depending on densities in the range of Fig. 5-15.

5.6. Simulated Transport with GYRO

GYRO also simulates the thermal transport due to the turbulent fluctuations. It is well known that $a/L_{Ti} = -(a/T_i)(dT_i/dr)$ is a crucial parameter in transport analysis. To quantitatively investigate the impact of a/L_{Ti} on thermal transport, we have carried out extensive sensitivity studies at the higher density ($\overline{n}_e = 0.93\times10^{20}\ \mathrm{m}^{-3}$), the medium density ($\overline{n}_e = 0.62\times10^{20}\ \mathrm{m}^{-3}$) and the lower density ($\overline{n}_e = 0.34\times10^{20}\ \mathrm{m}^{-3}$). The most relevant nominal input parameters at the center of the global simulations are summarized in Table 5-1. For each density, the key parameter $a/L_{Ti} = -(a/T_i)(dT_i/dr)$ is reduced by a factor of $\varepsilon = 0.1$, 0.2, or 0.3. The nonlinear global GYRO electrostatic simulations include 16 modes evenly spaced between $0.0 \lesssim k_\theta\rho_s \lesssim 1.0$ at the center of the simulation domain and cover the plasma of $0.4 \lesssim r/a \lesssim 0.8$ with the real mass ratio ($m_i/m_e \approx 3600$) and kinetic electrons. In addition, we have also estimated the uncertainties of the experimental thermal diffusivities by scaling the electron temperature and ion temperature profiles by ±15% ($T_i \to 0.85T_i$, $T_e \to 0.85T_e$; $T_i \to 0.85T_i$, $T_e \to 1.15T_e$; $T_i \to 1.15T_i$, $T_e \to 0.85T_e$; $T_i \to 1.15T_i$, $T_e \to 1.15T_e$) and feeding the scaled profiles into the TRANSP. The variations of the calculated diffusivities are used to estimate the experimental uncertainties. The comparison between the calculated χ_{eff} with TRANSP and simulated χ_{eff} with GYRO averaged over $r/a \in [0.4,\ 0.8]$ is shown in Fig. 5-16(a). The simulated χ_{eff} agrees with the experimental measurements after a ~20% reduction of a/L_{Ti}, where the simulated fluctuation intensities still agree with experiments within the experimental uncertainty (+/-60%) as shown in Fig. 5-16(b).

At the lowest density, TRANSP shows χ_e is well above χ_i; hence we can analyze χ_e and χ_i separately instead of χ_{eff}. The comparisons between the simulated and experimental χ_e and χ_i

are shown in Fig. 5-17. At the highest density ($\overline{n}_e = 0.93\times10^{20}$ m^{-3}) in the saturated ohmic regime, both simulated χ_e and χ_i agree with experimental measurements after reducing a/L_{Ti} by 20%. However, at the lower density $\overline{n}_e = 0.62\times10^{20}$ m^{-3} and $\overline{n}_e = 0.34\times10^{20}$ m^{-3} in the linear ohmic regime, the simulated χ_e and χ_i do not agree with experiments. As shown in Fig. 5-18, the simulated ion thermal diffusivity can be reduced to the experimental level by further reducing a/L_{Ti} and/or adding E×B shear[112], but simulated electron thermal diffusivity is also reduced below the experimental level.

Table 5-1: The input parameters at the center ($r/a = 0.63$) of the global simulations.

$\overline{n}_e$ [10^{20} m^{-3}]	0.34	0.62	0.93
Aspect Ratio R/a	3.115097	3.118168	3.128948
Elongation κ	1.221334	1.233673	1.203849
$s_\kappa = (r/\kappa)\partial\kappa/\partial r$	0.164005	0.172129	0.097774
Triangularity δ	0.085349	0.091244	0.061823
$s_\delta = r\partial\delta/\partial r$	0.182362	0.194366	0.109060
Safety factor q	1.410419	1.494749	1.152875
$\hat{s} = (r/q)\partial q/\partial r$	1.625332	1.585791	1.097617
$\nu_{ei}/(c_s/a)$	0.050849	0.161528	0.194468
a/L_{T_i}	3.612313	3.617833	2.370893
a/L_{T_e}	3.451792	3.139384	2.559236
a/L_{n_i}	0.850856	1.171108	0.904540
a/L_{n_e}	0.850856	1.171108	0.904540
T_i/T_e	0.385030	0.595595	0.727208

(a) Effective Thermal Diffusivity

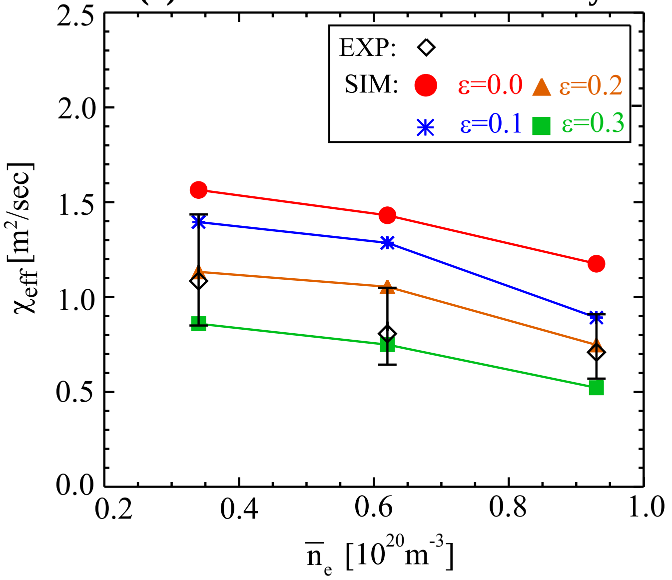

(b) Fluctuation Intensity

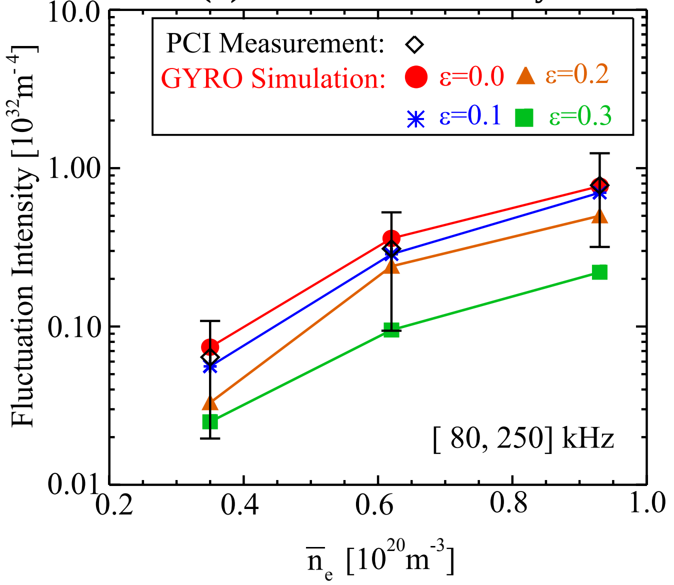

Figure 5-16: Comparison between simulations and experiments: (a) effective thermal diffusivities (χ_{eff}); (b) fluctuation intensity integrated over 80-250 kHz, where ε is the reduction factor of a/L_{Ti} in simulations, where ε is the reduction factor of a/L_{Ti} in simulations.

(a) Electron Thermal Diffusivity

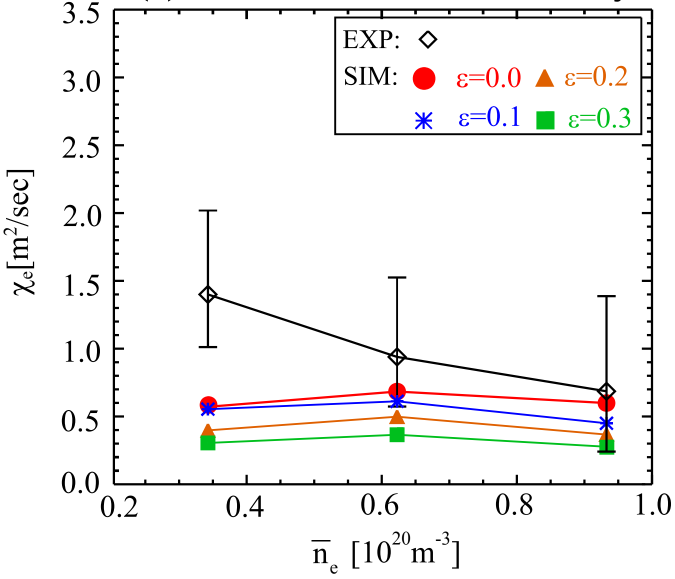

(b) Ion Thermal Diffusivity

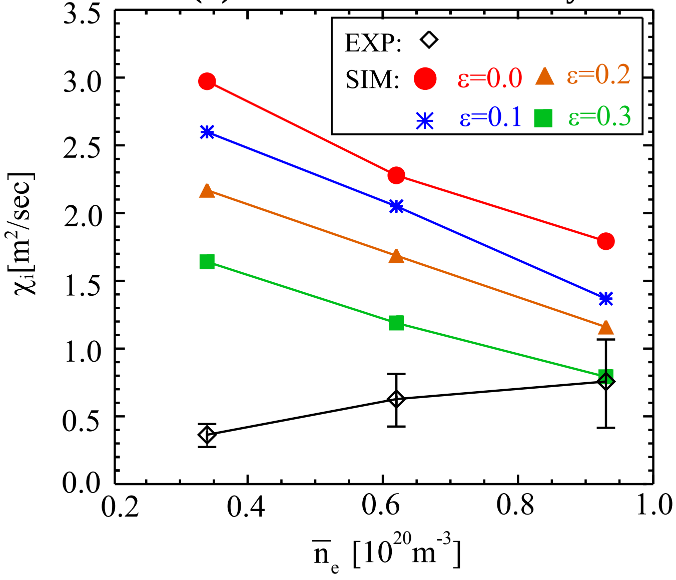

Figure 5-17: Comparison between the simulated (GYRO) and experimental (TRANSP) thermal diffusivities: (a) electron thermal diffusivity χ_e ; (b) ion thermal diffusivity χ_i, where ε is the reduction factor of a/L_{Ti} in simulations and $\chi_{e,i}$ is averaged over the domain of $r/a \in [0.4, 0.8]$..

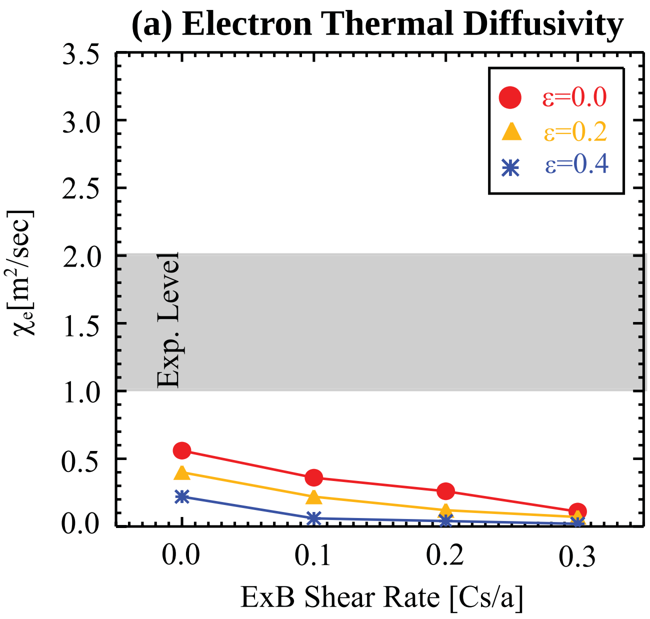

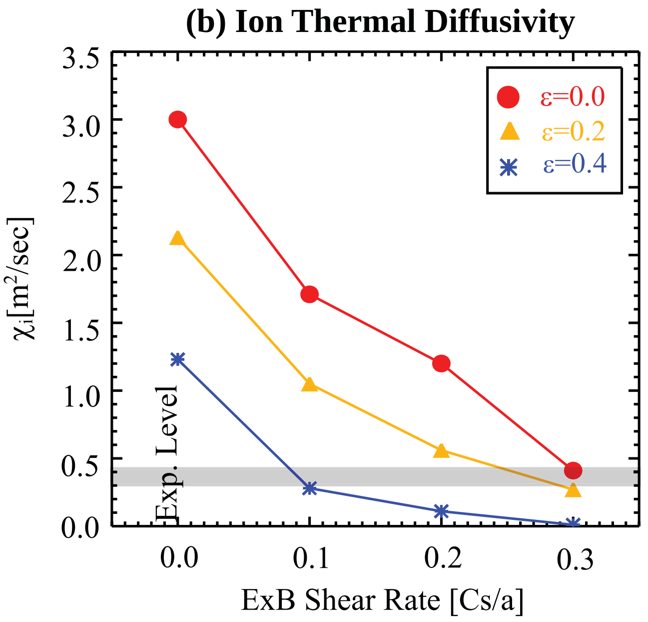

Figure 5-18: Effect of the E×B shear on the simulated thermal diffusivities at $\overline{n}_e = 0.34\times10^{20}$ m^{-3} : (a) electron thermal diffusivity χ_e ; (b) ion thermal diffusivity χ_i , where ε is the reduction factor of a/L_{Ti} in simulation, $\chi_{e,i}$ is averaged over the domain of $r/a \in \left[0.4, 0.8\right]$, and the E×B shear rate is in the scale of $c_s = 1.1\times10^6$ sec^{-1}. The shaded regime corresponds to the experimental level of χ_e and χ_i, respectively.

5.7. Further Investigation of the Linear Ohmic Regime

To further explore the discrepancy in thermal diffusivity between experiments and simulations in the linear ohmic regime, we have explored the impact of the trapped electron mode, impurity species, impurity profile, electromagnetic fluctuations, and high-k turbulence.

5.7.1 Impact of the Trapped Electron Modes

In principle, the trapped electron mode (TEM) can be destabilized when the density is steep as discussed in Chapter 2. To study the impact of the TEM turbulence, we have studied the effect of varying density gradients on turbulent transport with nonlinear global GYRO simulations at $\bar{n}_e = 0.34\times10^{20}\ \mathrm{m}^{-3}$ in the linear ohmic regime. The nonlinear global GYRO simulations include 16 modes evenly spaced between $0.0 \lesssim k_\theta \rho_s \lesssim 1.0$ and cover the plasma domain of $0.4 \lesssim r/a \lesssim 0.8$ with the real mass ratio ($m_i/m_e \approx 3600$) and kinetic electrons. The value of the dimensionless parameter $a/L_{ne} = -(a/n_e)(dn_e/dr)$ at $r/a = 0.63$ is used to quantify the variation of the density gradient. The value of $a/L_{ni} = -(a/n_i)(dn_i/dr)$ is varied together with a/L_{ne}, i.e. $a/L_{ni} = a/L_{ne}$. To also study the impact of the temperature gradient as the density gradient varies, two extra simulations in addition to the base case are performed for each a/L_{n_e}, where a/L_{T_i} is reduced by a factor of 0.2 and 0.4.

The comparison between the experimental $\chi_{e,i}$ and simulated $\chi_{e,i}$ with GYRO averaged over $r/a \in [0.4, 0.8]$ is shown in Fig. 5-19. It is found that the density gradient variation has a weak impact on turbulent transport. The simulated electron thermal diffusivity χ_e can only be raised to the experimental level after increasing a/L_{n_e} by at least a factor of two where the TEM turbulence becomes significant. The simulated ion transport χ_i always remains above the experimental level. The impact of the variation of the ion temperature gradient a/L_{T_i} on the turbulent transport becomes weaker when the TEM turbulence gets stronger. Since an increase of a/L_{n_e} by a factor of 2 is beyond the experimental uncertainty as shown in Fig. 5-6, significant thermal transport contribution from the TEM turbulence is not likely for the measured temperature and density profiles.

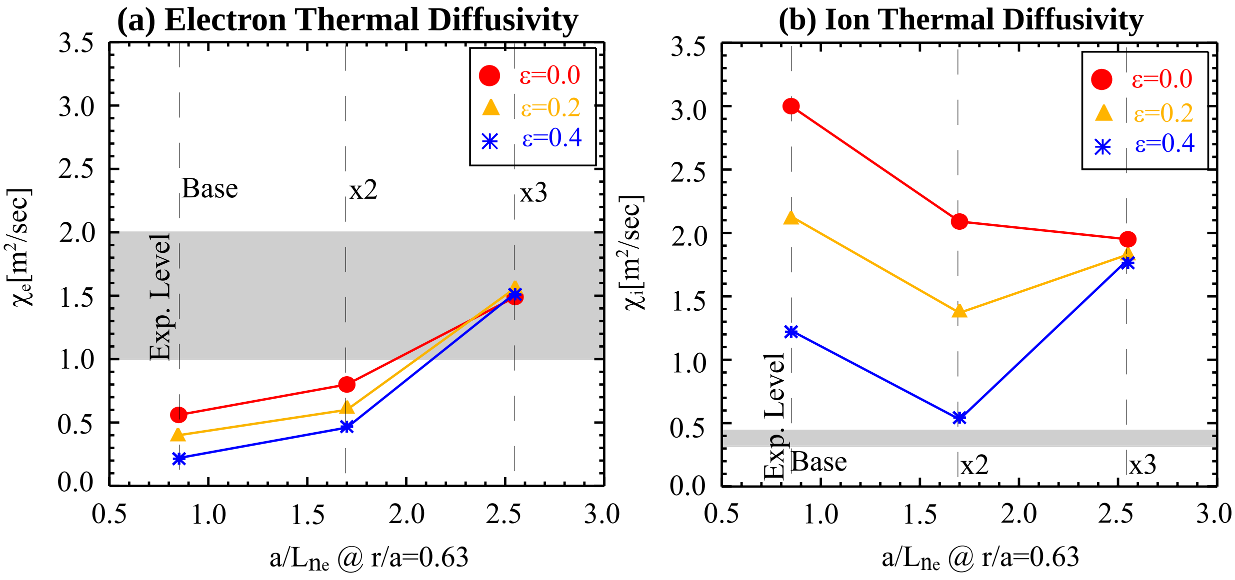

Figure 5-19: Impact of varying a correction factor applied to the measured density gradient on the simulated thermal diffusivities at $\bar{n}_e = 0.34\times10^{20}$ m^{-3}: (a) electron; (b) ion, where the a/L_{ne} of the base case is taken from the smoothed electron density profile as shown in Fig. 5-6, ε is the reduction factor of a/L_{Ti} used in the simulations. The shaded regime corresponds to the experimental level of χ_e and χ_i, respectively.

The collisions also play an important role in TEM, since the pitch angle scattering can scatter the trapped particles into the passing domain and vice versa. To explore the impact of the collisionality, we have a series of linear stability runs in the plane of a/L_{Ti}-$\nu_{ei}/(c_s/a)$, where ν_{ei} is the electron-ion collisional frequency and c_s is the ion sound speed. The other input parameters are taken from $r/a = 0.63$ at the lowest density plasma with $\bar{n}_e = 0.34\times10^{20}$ m^{-3} as in Table 5-1. These linear runs cover $0.0 \le a/L_{Ti} \le 4.0$ and $0.0 \le \nu_{ei}/(c_s/a) \le 0.1$. Because linear GYRO uses an initial value approach, it is restricted to only resolve the fastest growing (or least damped) eigenmode. The results are shown in Fig. 5-19. As shown in Fig. 5-20(a), for the experimental collisionality ($\nu_{ei}/(c_s/a) \sim 0.05$), TEM becomes the most unstable mode when $a/L_{Ti} \le 1.8$, which corresponds to a 50% reduction of the experimental base case. As shown in Fig. 5-20(b), the collisionality shows a strong stabilization of the TEMs but only a weak impact on the ITG modes. For the experimental collisionality ($\nu_{ei}/(c_s/a) \sim 0.05$), the growth rate ($\sim 320\times 10^3 \text{ sec}^{-1}$) of the ITG mode at $a/L_{Ti} \sim 3.6$ is larger than the growth rate of the TEMs $\sim 200\times 10^3 \text{ sec}^{-1}$ at $a/L_{Ti} \sim 0$. Thus, the thermal transport from the TEMs is expected to be less significant than the ITG modes. For illustrative purposes, a nonlinear flux-tube simulation has been performed at $a/L_{Ti} \sim 0.72$ (well below the experimental value) and $\nu_{ei}/(c_s/a) \sim 0.05$ where the TEM is the most unstable mode. The flux-tube simulation includes 20 modes up to $k_\theta \rho_s = 2.0$ with the real mass ratio ($m_i/m_e \approx 3600$) and kinetic electrons. The simulated electron thermal diffusivity χ_e is $0.08 \text{ m}^2/\text{sec}$, which is significantly below the experimental level of $1.5 \pm 0.5 \text{ m}^2/\text{sec}$.

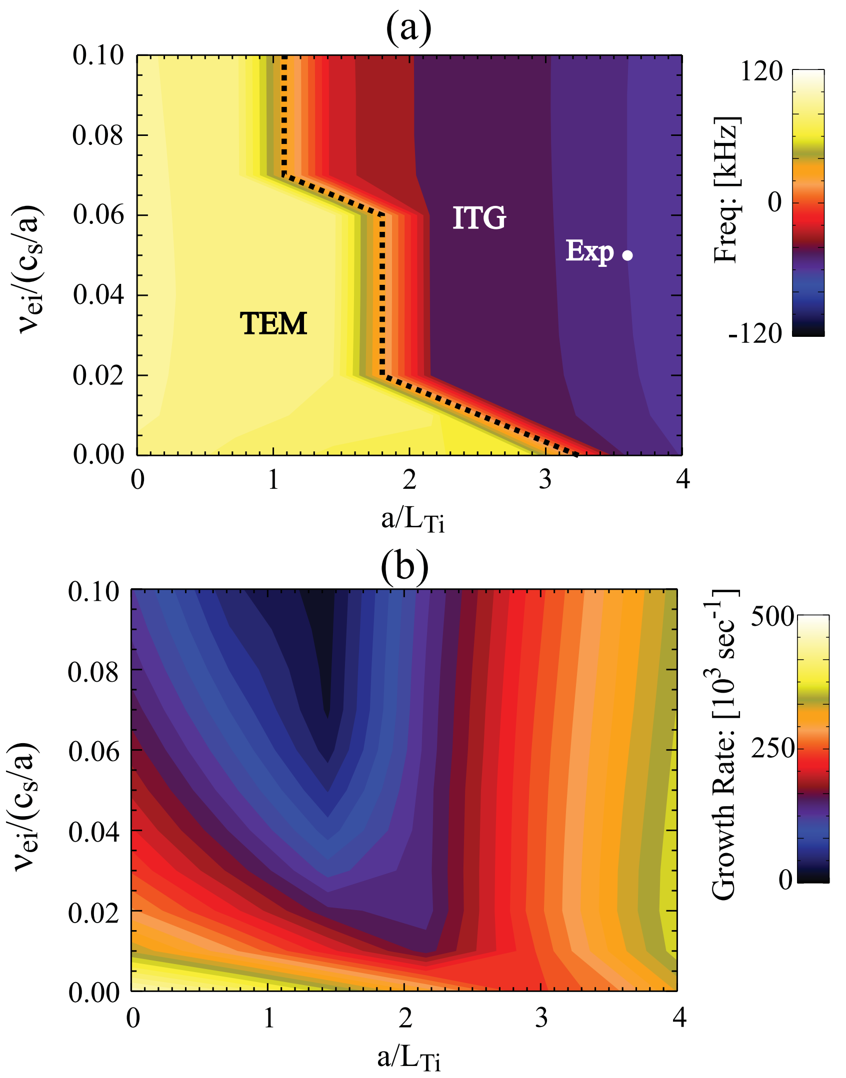

Figure 5-20: Contour plots of the frequency (a) and the growth rate (b) in the a/L_{Ti} - $\nu_{ei}/(c_s/a)$ plane. The other plasma parameters are taken from $r/a = 0.63$ at the lowest density plasma with $\bar{n}_e = 0.34\times10^{20}$ m^{-3}, where a/L_{Te}=3.452, a/L_{ne}=a/L_{ni}=0.851, and $T_i/T_e = 0.385$. The linear stability calculation is performed at $k_\theta\rho_s \sim 0.8$. The experimental values a/L_{Ti} and $\nu_{ei}/(c_s/a)$ are marked on the contour plot of the frequency, where the dashed line corresponds to the separation between the ITG mode $(f<0)$ and the TEM ($(f>0)$).

To quantitatively study the impact of collisionality on the simulated thermal transport, we have performed nonlinear local simulations with different ν_{ei} input. Three cases are considered: $\nu_{ei}/(c_s/a)=0.01$, $\nu_{ei}/(c_s/a)=0.05$, and $\nu_{ei}/(c_s/a)=0.10$, where $\nu_{ei}/(c_s/a)=0.05$ corresponds to the experimental measurements at $r/a=0.63$. The other input parameters are taken from $r/a=0.63$ at the lowest density plasma with $\overline{n}_e=0.34\times10^{20}$ m^{-3} as in Table 5-2. The local simulation includes 20 modes up to $k_\theta\rho_s=2.0$ with the real mass ratio ($m_i/m_e\approx3600$) and kinetic electrons. The results of the nonlinearly simulated thermal diffusivities at various ν_{ei} are summarized in Table 5-2, where both χ_e and χ_i increase as ν_{ei} decreases. The simulated electron thermal diffusivity χ_e remains below the experimental level of 1.5 ± 0.5 m^2/sec as ν_{ei} varies, while the simulated ion thermal diffusivity χ_i remains well above the experimental level of 0.4 ± 0.1 m^2/sec. The simulated wavenumber spectra of χ_e and χ_i are shown in Fig. 5-21. It is found that the increase of χ_e and χ_i at lower ν_{ei} is mainly due to the change of the longer wavelength turbulence ($k_\theta\rho_s\lesssim0.4$), while the impact of ν_{ei} on the shorter wavelength turbulence ($0.4\lesssim k_\theta\rho_s\lesssim2.0$) is less pronounced.

Table 5-2: Simulated χ_e and χ_i at various ν_{ei}, where $\nu_{ei}/(c_s/a)=0.05$ corresponds to the calculated ν_{ei} based on the experimental measurements. The other plasma parameters are taken from $r/a=0.63$ at the lowest density plasma with $\overline{n}_e=0.34\times10^{20}$ m^{-3}, where a/L_{Te}=3.45, a/L_{Te}=3.61, a/L_{ne}= a/L_{ni} =0.85, and $T_i/T_e=0.385$.

	χ_e [m^2/sec]	χ_i [m^2/sec]
$\nu_{ei}/(c_s/a)=0.01$	0.67	2.97
$\nu_{ei}/(c_s/a)=0.05$	0.56	2.67
$\nu_{ei}/(c_s/a)=0.10$	0.48	2.32

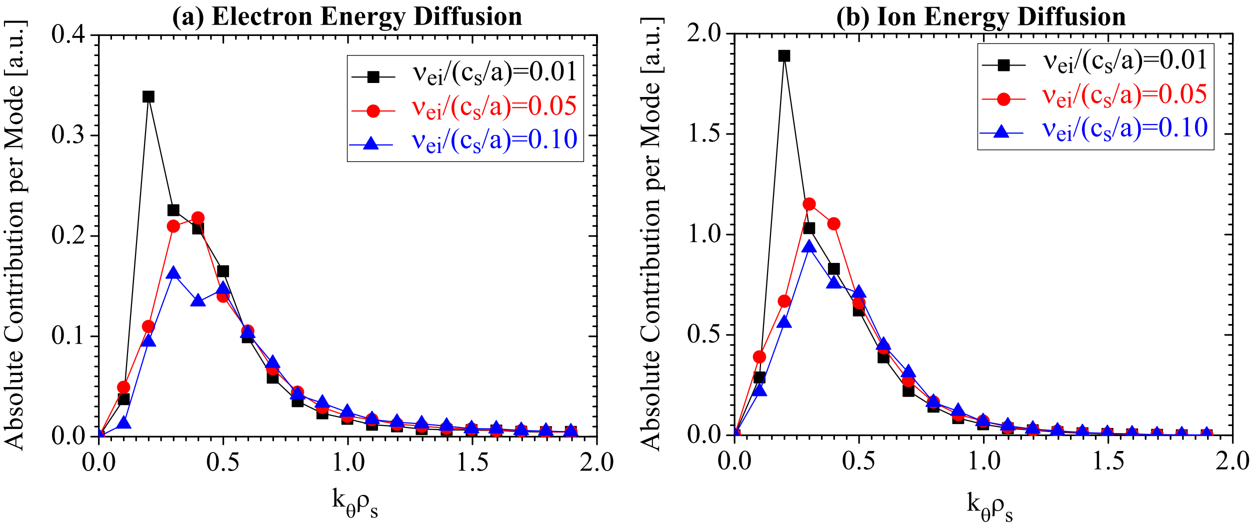

Figure 5-21: Absolute contribution per mode to thermal energy diffusion: (a) electron; (b) ion. The local simulations are performed at $r/a = 0.63$ at $\overline{n}_e = 0.34\times10^{20}$ m^{-3} with different $\nu_{ei}/(c_s/a)$: 0.01, 0.05, and 0.10. The other plasma parameters are taken from $r/a = 0.63$ at the lowest density plasma with $\overline{n}_e = 0.34\times10^{20}$ m^{-3}, where a/L_{Te}=3.45, a/L_{Te}=3.61, a/L_{ne}= a/L_{ni} =0.85, and $T_i/T_e = 0.385$.

Similar linear stability analyses are performed in the planes of a/L_{Ti}-a/L_{Te} and a/L_{Ti}-T_i/T_e. The result in the planes of a/L_{Ti}-a/L_{Te} are shown in Fig. 5-22 where ITG remains the most unstable mode even after varying a/L_{Ti} and a/L_{Te} by 50%. The results in the planes of a/L_{Ti}-T_i/T_e are shown in Fig. 5-23, where ITG also remains the most unstable mode in the range of $a/L_{Ti} \geq 1.6$ and $0.2 \leq T_i/T_e \leq 1.0$.

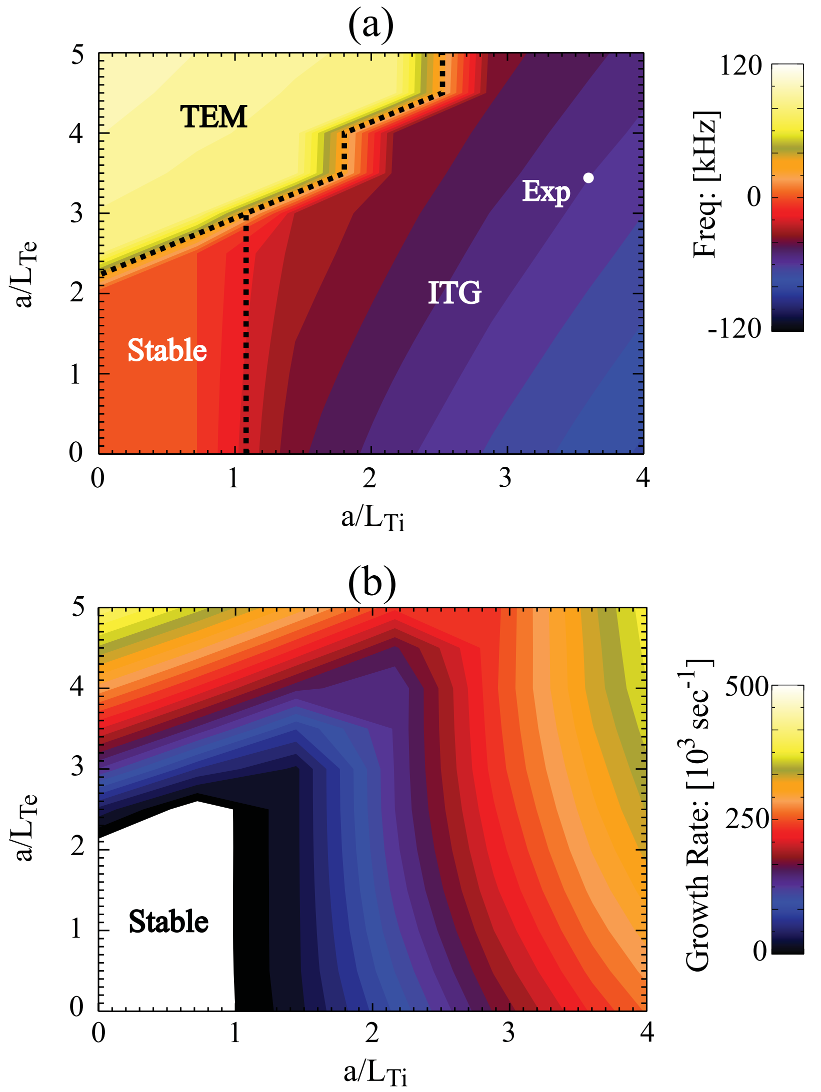

Figure 5-22: Contour plots of the frequency (a) and the growth rate (b) in the a/L_{Ti} - a/L_{Te} plane. The other plasma parameters are taken from $r/a = 0.63$ at the lowest density plasma with $\overline{n}_e = 0.34\times10^{20}$ m^{-3}, where a/L_{ne}=a/L_{ni}=0.851, $T_i/T_e = 0.385$, and $\nu_{ei}/(c_s/a) = 0.051$. The linear stability calculation is performed at $k_\theta\rho_s \sim 0.8$. The experimental values a/L_{Ti} and a/L_{Te} are marked on the contour plot of the frequency, where the dashed line corresponds to the separation between the stable regime, the ITG mode ($f < 0$) , and the TEM (($f > 0$)).

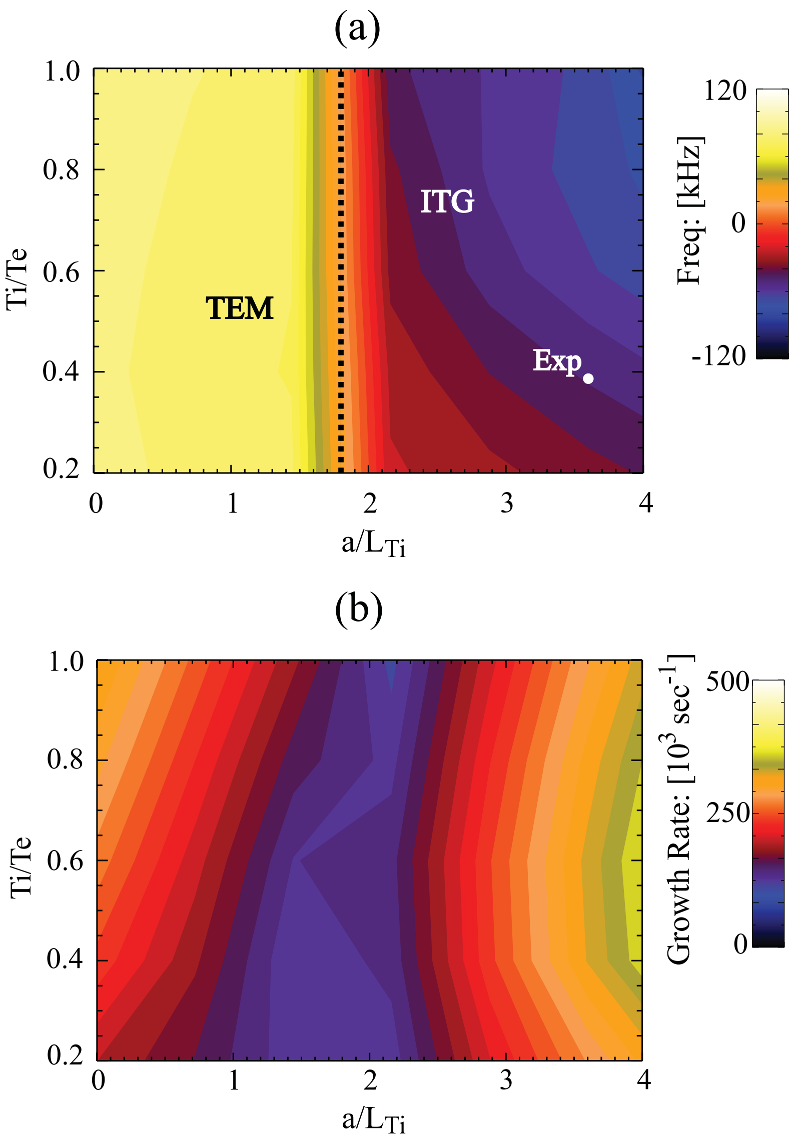

Figure 5-23: Contour plots in the a/L_{Ti} - T_i/T_e plane of the frequency at the maximum growth rate (a) and the maximum growth rate (b) in the wavenumber range of $0.4 \le k_\theta \rho_s \le 1.2$. The other plasma parameters are taken from $r/a = 0.63$ at the lowest density plasma with $\bar{n}_e = 0.34 \times 10^{20}$ m^{-3} , where a/L_{ne}=a/L_{ni}=0.851 , a/L_{Te}=3.452 , and $\nu_{ei}/(c_s/a) = 0.051$. The experimental values a/L_{Ti} and T_i/T_e are marked on the contour plot of the frequency, where the dashed line corresponds to the separation between the ITG mode ($f < 0$) and the TEM (($f > 0$)).

5.7.2 Impact of Assuming Different Impurity Species

To investigate the impact of impurities on the simulated thermal diffusivities, we have performed GYRO simulations with assumptions of different impurity species. To reduce the simulation time, the local simulations at $r/a = 0.63$ instead of global simulations are performed at $\overline{n}_e = 0.34\times10^{20}\ \mathrm{m}^{-3}$ in the linear ohmic regime. Each simulation includes 20 modes up to $k_\theta \rho_s = 2.0$ with the real mass ratio ($m_i / m_e \approx 3600$) and kinetic electrons. Four cases with different assumptions of the impurity species are used: (1) two species plasma, i.e. no impurity; (2) $Z_I = 5$, $M_I = 11$; (3) $Z_I = 12$, $M_I = 24$; (4) $Z_I = 42$, $M_I = 96$, where Z_I and M_I are the atomic number and atomic mass of assumed impurity species, respectively. For each assumed impurity species, n_e and ∇n_e are taken from the experimental measurement shown in Fig. 5-6, where $a/L_{n_e} = 0.85$. Z_{eff} is taken to be fixed at 2.6. The other unknown parameters (n_i, $\partial n_i / \partial r$, n_I, $\partial n_I / \partial r$) are calculated by combing the quasi-neutrality ($n_e = n_i + n_I Z_I$) and the expression of Z_{eff} ($n_e Z_{eff} = n_i + n_I Z_I^2$). The calculated densities are

$$\frac{n_i}{n_e} = \frac{Z_I - Z_{eff}}{Z_I - 1}, \tag{5.4}$$

$$\frac{n_I}{n_e} = \frac{Z_{eff} - 1}{Z_I \left(Z_I - 1 \right)}. \tag{5.5}$$

The calculated density gradients are

$$a/L_{n_i} = a/L_{n_e} + \frac{a}{Z_I - Z_{eff}} \frac{\partial Z_{eff}}{\partial r}, \tag{5.6}$$

$$a/L_{n_I} = a/L_{n_e} - \frac{a}{Z_{eff} - 1} \frac{\partial Z_{eff}}{\partial r}\ , \tag{5.7}$$

where $a/L_{n_e} = -\left(a/n_i\right)\left(\partial n_i / \partial r\right)$ and $a/L_{n_I} = -\left(a/n_I\right)\left(\partial n_I / \partial r\right)$. In this section, a flat Z_{eff} profile is assumed, i.e. $\partial Z_{eff} / \partial r = 0$. Thus, $a/L_{n_i} = a/L_{n_I} = a/L_{n_e}$. The impact of the inhomogeneity of the Z_{eff} profiles will be addressed in the next section. Both linear stability analysis and nonlinear simulations are performed.

The results of the linear stability calculation are shown in Fig. 5-24, where the ITG mode remains the most unstable mode with the growth rate spectrum peaking at $k_\theta \rho_s \sim 0.8$ and the frequency spectrum roughly proportional to $k_\theta \rho_s$. It is also seen that both the growth rate and frequency of the ITG mode decreases after the impurity species is included. Moreover, the case with the smallest Z_I ($Z_I = 5$) has the lowest growth rate and frequency. These numerical results indicate that the decrease of the growth rate and frequency is caused by the dilution of the main ions due to impurities, since the density of the main ion n_i decreases as Z_I increases when Z_{eff} is fixed at 2.6.

The nonlinear wavenumber spectra of electron and ion thermal diffusivities are shown in Fig. 5-25. The simulated electron thermal diffusivity χ_e is $0.86\ \mathrm{m}^2/\mathrm{sec}$ with the spectrum peaking at $k_\theta \rho_s \sim 0.4$ for the two species assumption. The impurity shows a stabilizing effect in the considered case. χ_e is reduced to $0.56\ \mathrm{m}^2/\mathrm{sec}$ in the case with $Z_I = 5$, while the structure of the wavenumber spectrum of χ_e remains similar. The simulated χ_e at different Z_I cases remains below the experimental level. The simulated ion thermal diffusivity χ_i behaves similarly to χ_e when the impurity is introduced. χ_i is reduced from $3.72\ \mathrm{m}^2/\mathrm{sec}$ to $2.67\ \mathrm{m}^2/\mathrm{sec}$ after the impurity with $Z_I = 5$ is included. The structure of the wavenumber spectrum remains similar for different assumptions of Z_I. The simulated χ_e and χ_i only show a weak dependence on the value of Z_I. This numerical study shows that the discrepancy in the electron thermal diffusivity in the linear ohmic regime between experiments and simulations cannot be explained by assuming different impurity species.

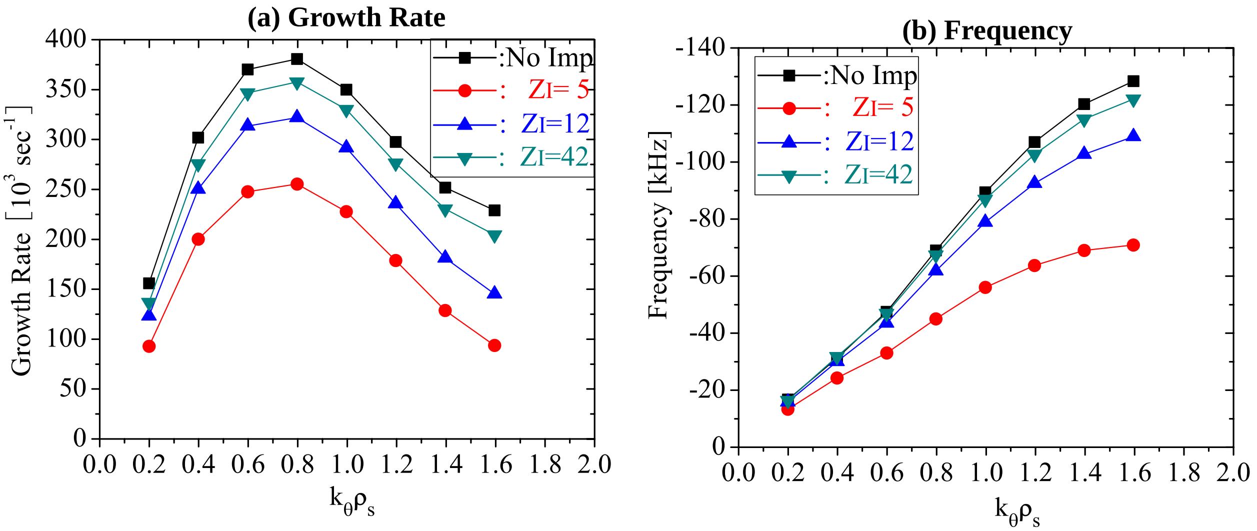

Figure 5-24: Linearly calculated growth rate spectra (a) and frequency spectra (b) at different Z_I: no impurity, 5, 12, and 42. The linear analysis is performed at $r/a = 0.63$ at $\bar{n}_e = 0.34\times10^{20}\ \mathrm{m}^{-3}$ in the linear ohmic regime.

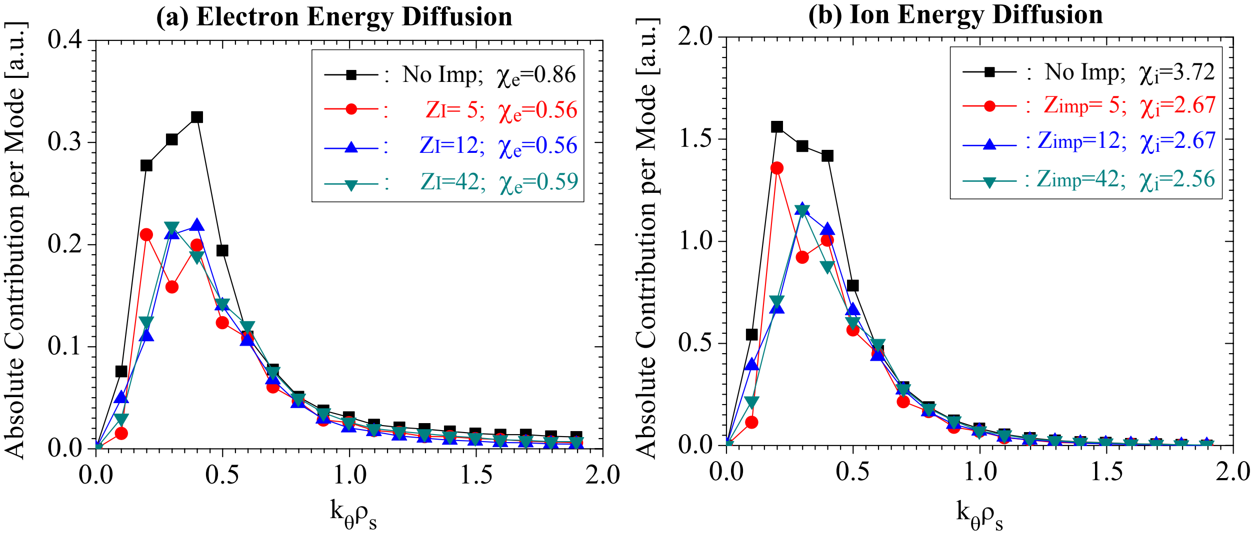

Figure 5-25: Absolute contribution per mode to thermal energy diffusion: (a) electron; (b) ion. The local simulations are performed at $r/a = 0.63$ at $\bar{n}_e = 0.34\times10^{20}\ \mathrm{m}^{-3}$ in the linear ohmic regime with different assumptions of impurity species: no impurity, Z_I=5, Z_I=12, and Z_I=42. The electron and ion thermal diffusivities of each case are labelled in the unit of $\mathrm{m}^2/\mathrm{sec}$.

5.7.3 Impact of a non-Flat Z_{eff} Profile

In this section, we explore the impact of a non-flat Z_{eff} profile on thermal transport at $\bar{n}_e = 0.34\times10^{20}$ m^{-3} in the linear ohmic regime. To isolate the effect of the non-flat Z_{eff} profile, the charge number Z_I of the impurity species is assumed to be 12, the atomic number M_I is assumed to be 24, Z_{eff} is taken to be fixed at 2.6, and $a/L_{n_e} \simeq 0.85$ is taken from the experimental measurement. A parameter a/L_{Zeff} defined as

$$a/L_{Zeff} = -\frac{a}{Z_{eff}}\frac{\partial Z_{eff}}{\partial r} \tag{5.8}$$

is used to quantify the gradient of the Z_{eff} profile. To reduce the simulation time, the local simulations at $r/a = 0.63$ are performed. Both linear stability analysis and numerical simulations are carried out.

Linear stability analysis of five cases were performed, where $a/L_{Zeff} = 1.0$, 0.5, 0.0, -0.5, and -1.0. Table 5-3 lists the other density parameters of the main ion and the impurity species of each case. It is found that the impurity density profile is inverted and $a/L_{n_I} \simeq -0.74$, when $a/L_{Zeff} = -1.0$. The calculated growth rate and frequency spectra are shown in Fig. 5-26. The growth rate increases as a/L_{Zeff} decreases, which indicates the stabilizing effect from a central peaked impurity profile ($a/L_{n_I} > 0.0$) and destabilizing effect from an inverted impurity profile ($a/L_{n_I} < 0.0$). The frequency also increases as a/L_{Zeff} decreases, while the ITG mode remains the most unstable mode. This numerical result in toroidal geometry is consistent with early studies by Coppi of drift instability due to impurity ions in slab geometry[24].

Table 5-3: Density parameters of main ion and impurity species for each case of the non-flat Z_{eff} profiles.

	Case 1	**Case 2**	**Case 3**	**Case 4**	**Case 5**
a/L_{Zeff}	1.0	0.5	0.0	−0.5	−1.0
n_i/n_e	0.85	0.85	0.85	0.85	0.85
n_I/n_e	0.013	0.013	0.013	0.013	0.013
a/L_{n_i}	0.56	0.70	0.85	1.00	1.14
a/L_{n_I}	2.44	1.64	0.85	0.056	−0.74

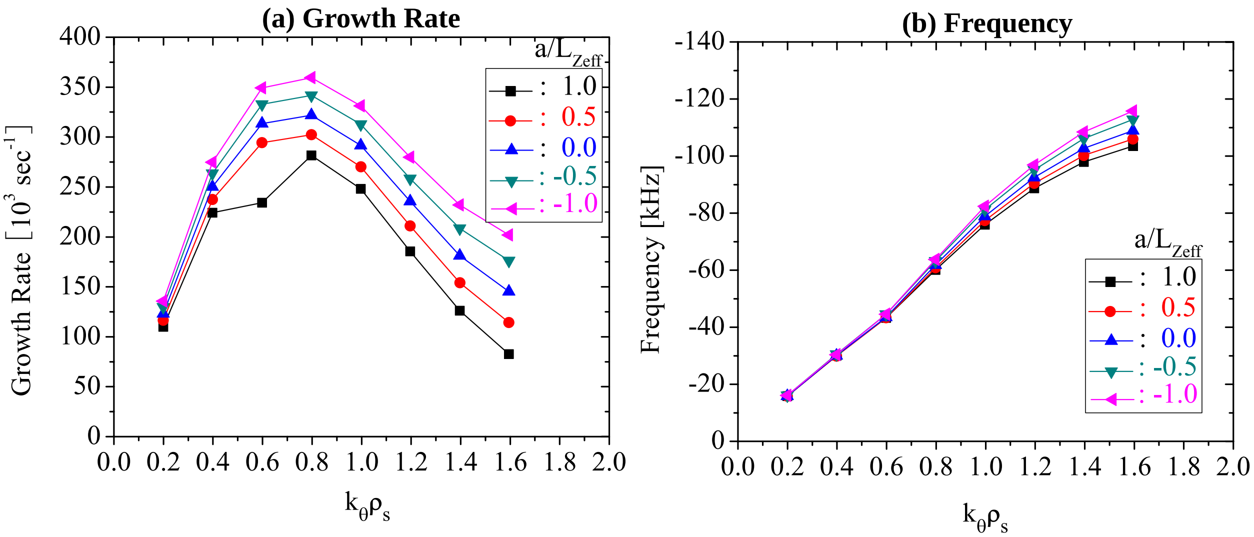

Figure 5-26: Linearly calculated growth rate spectra (a) and frequency spectra (b) at different a/L_{Zeff} : 1.0, 0.5, 0.0, -0.5, and -1.0. The linear analysis is performed at $r/a = 0.63$ at $\bar{n}_e = 0.34\times10^{20}$ m^{-3} in the linear ohmic regime.

To further explore whether the turbulence with an increased growth rate can drive enough electron thermal transport to account for the experimental measurements, we have also nonlinearly simulated the case with $a/L_{Zeff} = -1.0$. The local simulation at $r/a = 0.63$ is performed and the simulation includes 20 modes up to $k_\theta\rho_s = 2.0$ with the real mass ratio ($m_i/m_e \approx 3600$) and kinetic electrons. The simulated thermal diffusivity spectra are shown together with the case with $a/L_{Zeff} = 0.0$ in Fig. 5-27. The simulated electron diffusivity spectra at $a/L_{Zeff} = 0.0$ and $a/L_{Zeff} = -1.0$ are similar as shown in Fig. 5-27(a). After changing a/L_{Zeff} from 0.0 to -1.0, the χ_e is increased from $0.56\ \mathrm{m}^2/\mathrm{sec}$ to $0.61\ \mathrm{m}^2/\mathrm{sec}$ but remains below the experimental level. The structure of the simulated diffusivity spectrum remains similar. The simulated wavenumber spectrum of the ion diffusivity χ_i at $a/L_{Zeff} = 0.0$ and $a/L_{Zeff} = -1.0$ is shown in Fig. 5-27(b). After changing a/L_{Zeff} from 0.0 to -1.0, χ_i behaves similarly to χ_e. χ_i is increased from $2.67\ \mathrm{m}^2/\mathrm{sec}$ to $2.96\ \mathrm{m}^2/\mathrm{sec}$ and the structure of the diffusivity spectrum remains similar.

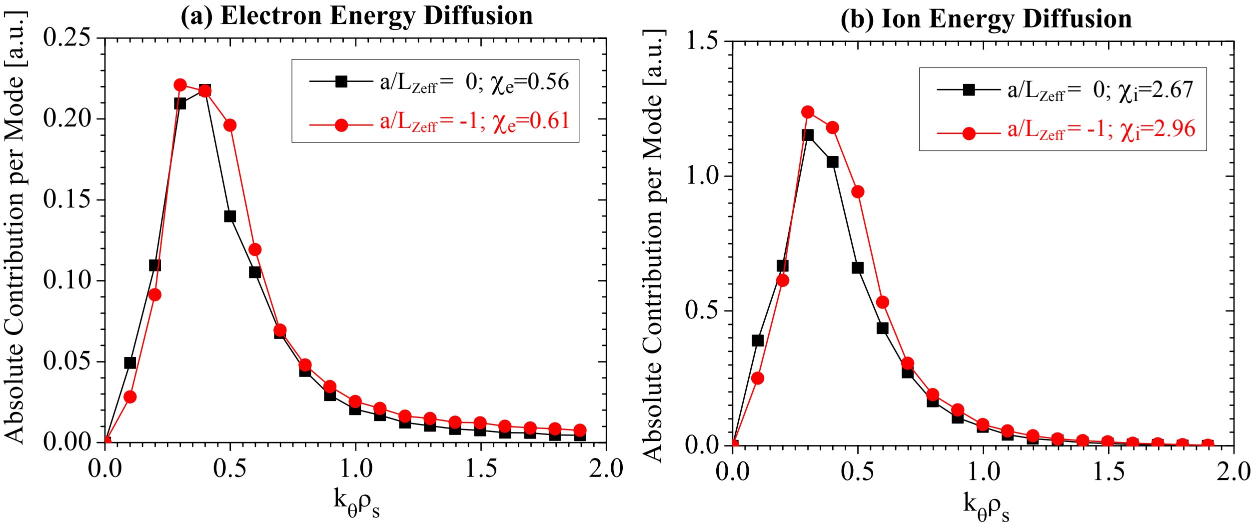

Figure 5-27: Absolute contribution per mode to thermal energy diffusion: (a) electron; (b) ion. The local simulations are performed at $r/a = 0.63$ at $\overline{n}_e = 0.34\times10^{20}\ \mathrm{m}^{-3}$ in the linear ohmic regime with $a/L_{Zeff} = 0.0$ and -1.0. The electron and ion thermal diffusivities of each case are labelled in the unit of $\mathrm{m}^2/\mathrm{sec}$.

5.7.5 Impact of Electromagnetic Fluctuations

The electrostatic approximation is assumed for all the above nonlinear simulations presented in this chapter, since the contributions from electromagnetic fluctuations should be negligible in the simulated low-β C-Mod plasmas. To further quantify the contribution to the thermal transport from electromagnetic fluctuations and verify the electrostatic assumption, we have performed nonlinear flux-tube simulations with finite-β effect included at $\overline{n}_e = 0.34\times10^{20}$ m^{-3} in the linear ohmic regime. The local simulation is performed at $r/a = 0.63$ and the simulation includes 20 modes up to $k_\theta\rho_s = 2.0$ with the real mass ratio ($m_i/m_e \approx 3600$) and kinetic electrons. Two simulations are performed with different scaling factors on the measured electron beta $\beta_e = 2\mu_0 n_e T_e / B_\phi^2$, where the scaled β_e is 0.07% and 0.14%, respectively. 0.07% corresponds to the experimental measurements. The results of the nonlinearly simulated thermal diffusivities at different β_e are shown together with the simulation under the electrostatic assumption in Table 5-4. It is found that the electromagnetic fluctuations contribute less than 3% of the total simulated thermal transport even after doubling the experimental measured β_e. Therefore, the electrostatic assumption is justified for the considered low-β C-Mod plasmas.

Table 5-4: Simulated χ_e and χ_i at various β_e, where $\chi_{e,i}^{ES}$ is the thermal diffusivity due to the electrostatic fluctuations and $\chi_{e,i}^{EM}$ is thermal diffusivity due to the electromagnetic fluctuations. The local simulations are performed at $r/a = 0.63$ at $\overline{n}_e = 0.34\times10^{20}$ m^{-3} with $Z_I = 12$, $Z_{eff} = 2.6$, and $a/L_{Zeff} = 0.0$.

	χ_e^{ES} [m^2/sec]	χ_e^{EM} [m^2/sec]	χ_i^{ES} [m^2/sec]	χ_i^{EM} [m^2/sec]
$\beta_e = 0.00\%$	0.56	0.0	2.67	0.0
$\beta_e = 0.07\%$	0.56	0.004	2.67	0.001
$\beta_e = 0.14\%$	0.56	0.017	2.67	0.003

5.7.6 Contributions from the High-k Turbulence

To further investigate the discrepancy at $\overline{n}_e = 0.34 \times 10^{20}$ m^{-3} in the linear ohmic regime, we have performed GYRO simulations in the shorter wavelength length ($k_\theta \rho_s > 1.0$) regime. The results of the linear stability analysis at $r/a = 0.63$ in the range of $60 > k_\theta \rho_s > 2.0$ are shown in Fig. 5-28, where the ETG mode is unstable with the growth rate spectrum peaking at $k_\theta \rho_s \sim 25$ and the frequency spectrum approximately proportional to $k_\theta \rho_s$.

The nonlinear GYRO simulations include 16 modes up to $k_\theta \rho_s = 4$ with the real mass ratio ($m_i / m_e \approx 3600$) and kinetic electrons. The wavenumber spectra of the simulated electron and ion thermal transport are shown in Fig. 5-29. The short wavelength turbulence in the range of $4.0 > k_\theta \rho_s > 2.0$ only can contribute to the electron thermal transport by 5.0% and its contribution to the ion thermal diffusivity is negligible.

Recent simulations with characteristic parameters of DIII-D core plasmas by Candy and Waltz[113-114] shows that 10-20% of the total electron transport can arise from the ETG scale ($k_\theta \rho_s > 1.0$) where the ion-scale instabilities are not suppressed. They also showed that if the ion-scale instabilities are suppressed, by removal of the ion free energy[113] or by the presence of ExB shear suppression[114], this fraction can increase significantly. This result was also confirmed by Goerler and Jenko.[115] However, since the case we are considering has significant ITG drive, it seems unlikely that the ETG scale ($k_\theta \rho_s > 1.0$) turbulence can significantly contribute to the electron thermal transport. This has been partially verified by our simulations up to $k_\theta \rho_s = 4.0$, which shows that only 12.5% of the electron transport arises from the short wavelength turbulence in the range of $4.0 > k_\theta \rho_s > 1.0$. Nevertheless, in the future, it may be interesting to explore the role of even shorter wavelength turbulence in the range of $k_\theta \rho_s > 4.0$ under our experimental conditions and profiles to resolve this issue. Currently, we have not had access to expensive computer capabilities that are necessary for nonlinear GYRO simulation of such turbulence.

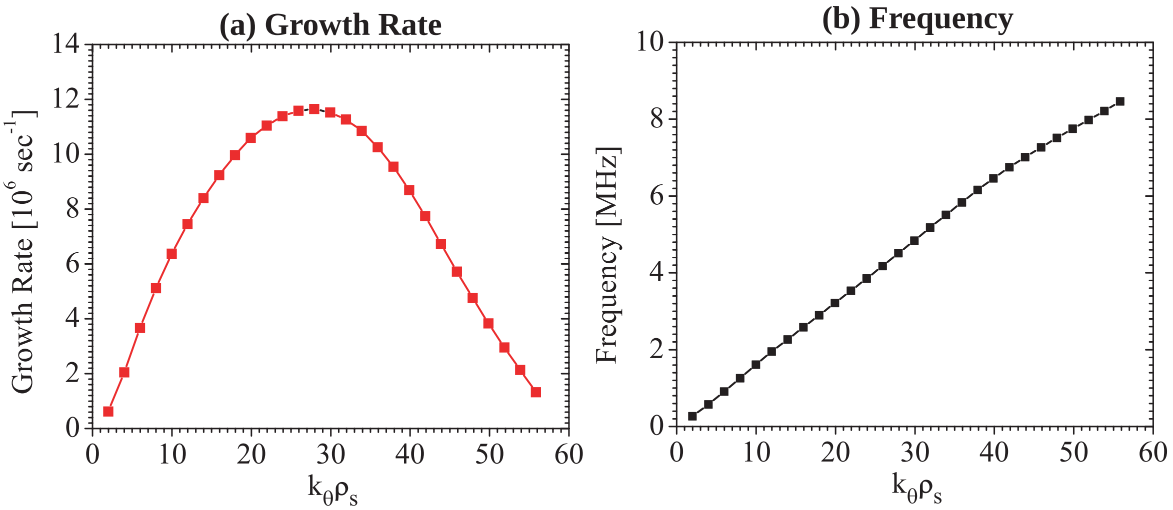

Figure 5-28: Growth rate (a) and frequency (b) spectra of the ETG mode. The parameters in the linear analysis are taken at $r/a = 0.63$ at $\bar{n}_e = 0.34\times10^{20}$ m^{-3} in the linear ohmic regime.

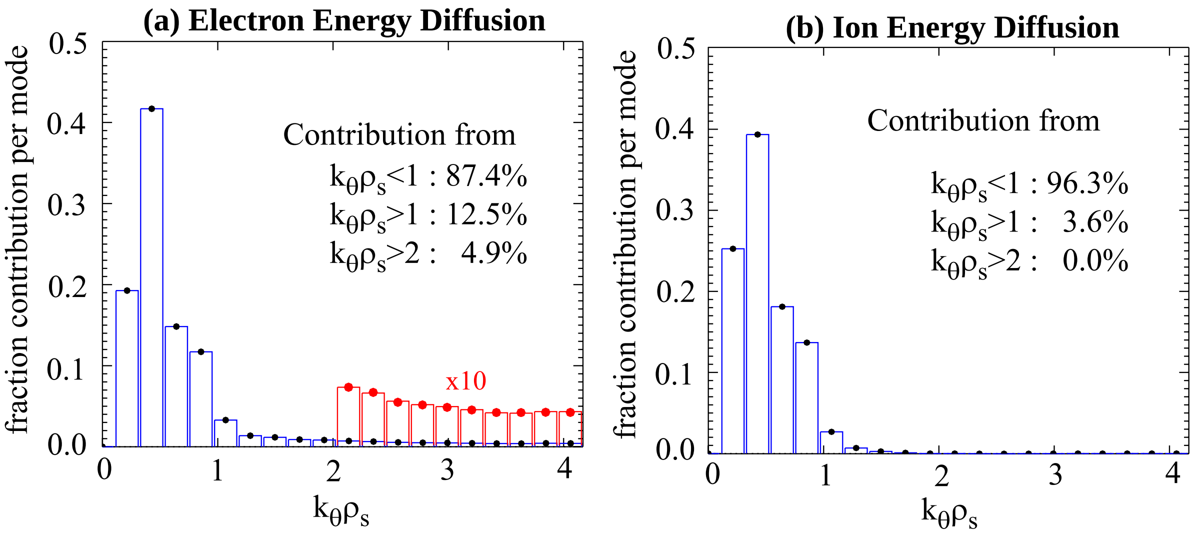

Figure 5-29: Fractional contribution per mode to thermal energy diffusion: (a) electron; (b) ion. The simulation is performed at $\bar{n}_e = 0.34\times10^{20}$ m^{-3} in the linear ohmic regime.

5.8. Summary and Discussion

In this chapter, we reported numerical and experimental studies of turbulence and transport in Alcator C-Mod ohmic plasmas. The studies were carried out over the range of densities covering the "neo-Alcator" (linear confinement time scaling with density, electron transport dominates) to the saturated ohmic regime. Quantitative comparisons in both turbulence and thermal transport between experimental measurement and simulation were performed.

At high densities in the saturated ohmic regime, the key role played by the ITG turbulence has been verified, including measurements that the turbulent waves propagate in the ion diamagnetic direction. It is also found that the intensity of the ITG turbulence increases with density, in agreement between simulation and experiments. The absolute fluctuation wavenumber spectrum agrees with simulation within experimental error (+/-60%). Agreement in χ_e , χ_i , and χ_{eff} between experiment and theory is obtained after taking a 20% reduction of a / L_{Ti} , all within the experimental uncertainty.

At the low density in the linear ohmic regime, where the electron transport dominates ($\chi_e \gg \chi_i$), the GYRO simulation of the longer wavelength turbulence ($k_\theta \rho_s < 1$) shows $\chi_i > \chi_e$ although the simulated χ_{eff} agrees with experiments after reducing the ion temperature gradient by 20%. Our nonlinear simulation including the shorter wavelength turbulence up to $k_\theta \rho_s \sim 4$ does not raise the simulated electron thermal diffusivity to the experimental level. Although it is possible that measurements and simulations at even shorter wavelengths may be necessary to explain transport in this regime, measurements to date by PCI indicate very low levels of high-k turbulence, falling into the background noise level. While the TEM modes are linearly unstable, under our experimental conditions their growth rates are smaller than the ITG modes. The nonlinear simulations of TEM turbulence would become important only for significantly steeper density gradients, namely a/L_n greater than about 2.5. Hence according to our nonlinear GYRO simulations, a significant thermal transport contribution from the TEM turbulence is not likely in the C-Mod low density ohmic regime. Our simulations including electromagnetic effects also show that the contribution from electromagnetic fluctuations is negligible in these low-β plasmas. Therefore, at the present time we are unable to determine the cause of the electron transport in the linear ohmic regime. One possibility, not included in gyrokinetic simulations, is that the electron drift velocity associated with the "ohmic toroidal plasma current" drives electron drift waves which may be more unstable at the lower densities where the electron drift velocity can be a non-negligible fraction of the electron thermal speed and can even exceed the ion acoustic speed. To explore this would require a modification of present day gyrokinetic codes in use. Another possibility is the micro-reconnecting mode (MRM)[39-43] discussed in Section 2.2.2. For the parameters at $r/a = 0.63$ in a low density C-Mod ohmic plasma in the linear ohmic regime with $n_e \sim 0.4\times10^{20}\ \mathrm{m}^{-3}$, $T_e \sim 1.2\ \mathrm{keV}$, $L_{Te} \sim 0.06\ \mathrm{m}$, $L_{ne} \sim 0.26\ \mathrm{m}$, and $B \sim 5.2\ \mathrm{T}$, we have $d_e \sim 8.4\times10^{-4}\ \mathrm{m}$, $\rho_e \sim 1.6\times10^{-5}\ \mathrm{m}$, $k_{MRM} \sim 1.2\times10^{3}\ \mathrm{m}^{-1}$, $k_{MRM}\rho_e \sim 0.02$, $\chi_{MRM} \sim d_e\rho_e\upsilon_{the}/L_{Te}$ $\sim 3\ \mathrm{m}^2/\mathrm{sec}$. The thermal diffusivity induced by the MRM instability is in the experimentally relevant level. Currently, low-n tearing modes may not be well accounted for in GYRO because of certain numerical issues.

Chapter 6

Turbulence and Transport Studies in H-Mode Plasmas

6.1 Introduction

The phase contrast imaging diagnostic (PCI) has been used to study drift-wave type turbulence in C-Mod H-Mode plasmas. However, the previous studies were limited to experimental observation[57], or at best a qualitative comparison with numerical simulations in the structure of the wavenumber spectrum[116]. The recent development of an improved calibration for the PCI system allows for the intensity of the observed fluctuations to be determined absolutely.[58] Furthermore, the localizing upgrade has also enabled the PCI diagnostic to localize the short wavelength turbulence in the electron temperature gradient (ETG) range and resolve the direction of propagation (i.e., electron vs. ion diamagnetic direction) of the longer wavelength turbulence in the ion temperature gradient (ITG) and trapped electron mode (TEM) range. In addition, development of the synthetic PCI diagnostic[91] on GYRO allows for direct and quantitative comparisons between the PCI measurements and numerical predictions. As a result, revisiting H-Mode plasmas with improved experimental turbulence measurements and advanced gyrokinetic simulations is essential in quantitatively validating the numerical codes.

In this chapter, we present studies of turbulence and transport in C-Mod H-Mode plasmas using the calibrated PCI diagnostic with the localizing capability and synthetic diagnostic tools. We also examine H-Mode plasmas with internal transport barriers (ITBs) assisted with ion cyclotron resonance frequency (ICRF) heating.[117] Because of its reduced energy and/or particle transport and improved confinement, understanding ITB physics remains of great interest to the fusion community. Our studies focus on the plasma both before and after the ITB formation as on and off-axis ICRF heating is applied.

The remainder of this chapter is organized as follows: in Section 6.2, the experimental setup is presented; in Section 6.3, fluctuation measurements are presented; in Section 6.4, the gyrokinetic simulation of turbulence and transport is discussed; in Section 6.5, a comparison is given between fluctuation measurements and GYRO predictions. Finally, in Section 6.7 the conclusions are presented.

6.2 Experimental Setup

The experiments considered here were conducted with the on-axis toroidal magnetic of 4.5 T and the plasma current of 0.8 MA. The primary auxiliary heating in C-Mod is radio frequency (RF) waves in ion cyclotron range of frequencies (ICRF) launched by two 2-strap antennas at 80 MHz and one 4-strap antenna with a tunable frequency from 50 to 80 MHz.[11] The ICRF antennas are configured for hydrogen minority resonance heating in deuterium majority plasmas.

Time traces of the major parameters of a typical H-Mode plasma discharge in Alcator C-Mod are shown in Fig. 6-1. At t=0.8 sec, the enhanced D_α H-Mode[118] is fully developed, following application of the off-axis (r/a=0.5) ICRF heating of 2.0 MW at 80 MHz on the high field side starting at t=0.7 sec. After another ~0.28 sec, an ITB is established at t=1.08 sec, manifesting itself in steepened density profiles (see Fig. 6-2). Earlier experiments found that impurities accumulate in the plasma core after the ITB formation, which can lead to a radiative collapse of the transport barrier.[119] To control the impurity accumulation and maintain the steady ITB, an additional on-axis (r/a=0.1) ICRF heating power of 0.6 MW at 70 MHz is added at t=1.2 sec.[120] This added on-axis ICRF heating arrests the density rise, as shown in Fig. 6-1(c), where the line-integrated density ceases to increase after the on-axis heating. As a result, the ITB lasts for another ~0.3 sec until the end of the ICRF heating pulse at t=1.5 sec. The on-axis ICRF heating also causes a near-doubling of the fusion neutron rate, as shown in Fig. 6-1(b). In addition, the intensity of the D_α emission increases after the on-axis ICRF heating is added, which suggests an impact of the extra on-axis heating on plasma edge turbulence.

The ITB plasmas in Alcator C-Mod feature a peaked electron density profile, as shown in Fig. 6-2a, while the induced change in the electron temperature profiles during ITB is much less pronounced (see Fig. 6-2b). At such high electron density, the electron-ion thermal equilibrium time $\tau_{ei} \sim 0.005\ \mathrm{sec}$, which is much smaller than the energy confinement time $\tau_E \sim 0.025\ \mathrm{sec}$. Therefore, the electrons and ions are strongly coupled due to collisions and the ion temperature is close to the electron temperature, i.e. $T_i \simeq T_e$.

We also want to point out that the experimental features of ITB in the considered plasmas are not very apparent. Our later transport analysis (Fig. 6-14) in Sec. 6.5 shows that the effective thermal diffusivity χ_{eff} drops from $0.4\ \mathrm{m}^2/\mathrm{sec}$ to $0.2\ \mathrm{m}^2/\mathrm{sec}$ at $r/a = 0.5$ after the ITB onset, which confirms the existence of an ITB.

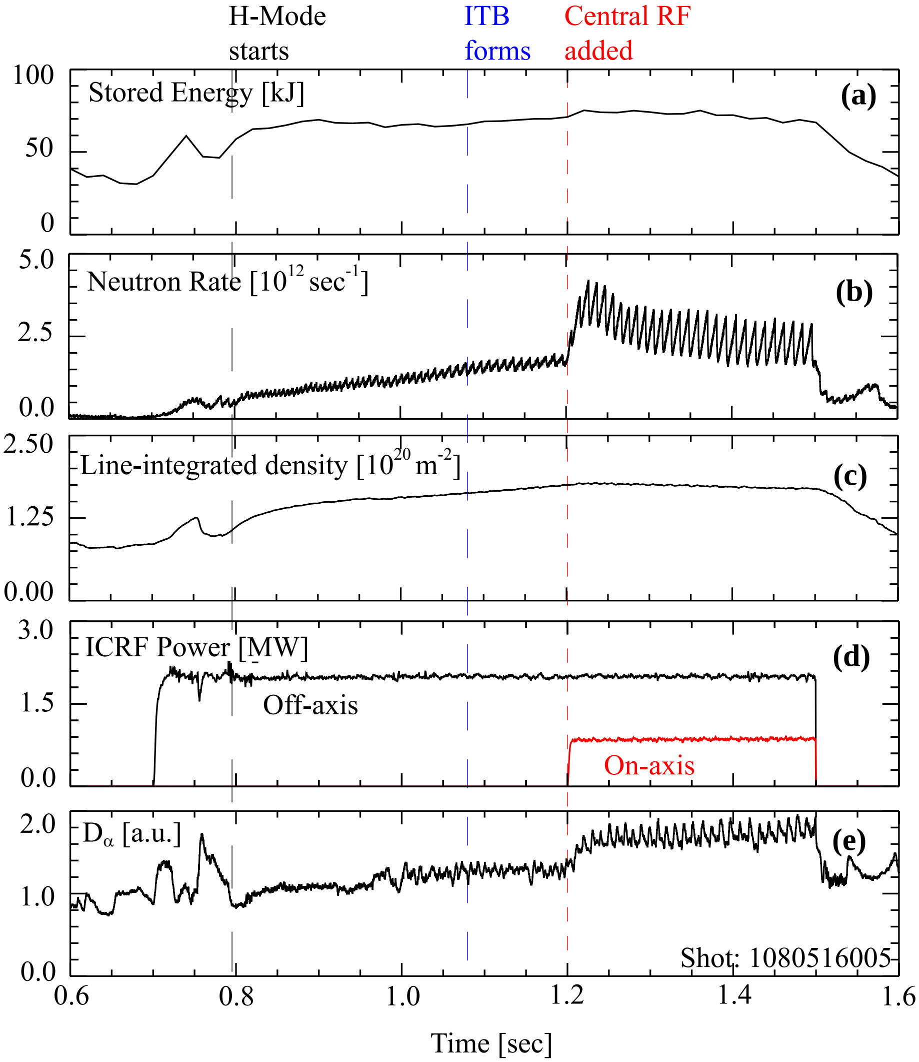

Figure 6-1: Plasma parameters for the studied discharge: (a) store energy; (b) neutron rate; (c) line-integrated electron density; (d) ICRF power; (e) Dα light.

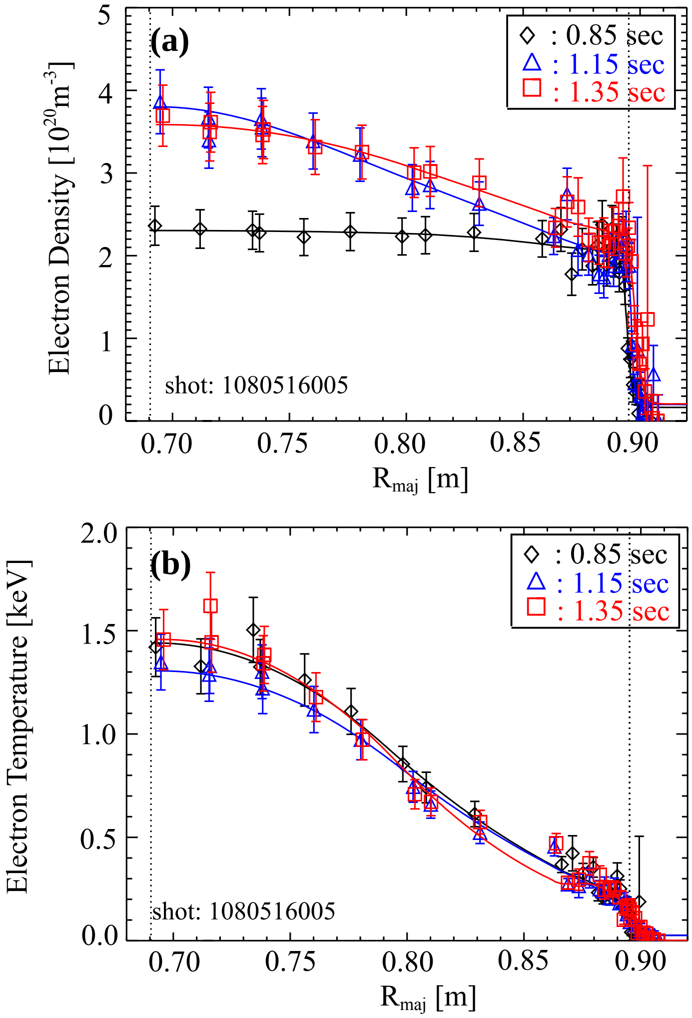

Figure 6-2: Profiles of electron density (a) and temperature (b) from the Thomson scattering (TS) diagnostic[121] are shown before the ITB onset at t=0.85 sec (black diamond), during the ITB with only off-axis ICRF heating at t=1.15 sec (blue triangle), and during the ITB after adding on-axis ICRF heating at t=1.35 (red square). The solid line is a fit to the experimental measurements using FiTs. Two vertical dashed lines are the magnetic axis and last closed flux surface (LCFS), respectively.

6.3. Fluctuation Measurements

To study the change in turbulent transport as an ITB forms, it is of great importance to measure the change in turbulent fluctuations. In Alcator C-Mod, the phase contrast imaging (PCI) diagnostic has been used to monitor these fluctuations. Typical discharges studied in this chapter exhibit broadband turbulence as well as a quasi-coherent (QC)[54] fluctuation. The spectrogram of the measured fluctuation from a single PCI chord (channel 17) is shown in Fig. 6-3, corresponding to the plasma evolution shown in Fig. 6-1. When the EDA H-Mode develops ~0.1 sec after the off-axis ICRF heating is applied, the QC mode (~140 kHz) appears. The visible frequency of the broadband fluctuations increases from ~250 kHz at 0.65 sec to ~450 kHz at 0.90 sec, where the visible frequency is defined as the signal level drops to 10^{-4} as shown in Fig. 6-4. The burst at 0.75 sec is due to the unsteadiness of the ICRF heating (i.e., periodic dropouts). The density peaking starts at ~1.0 sec and the ITB forms at ~1.1 sec. During the density peaking, the intensity of broadband turbulence with frequencies below 80 kHz increases (see Fig. 6-3d), but the upper bound of the visible frequency of broadband turbulence decreases from ~450 kHz to ~350 kHz (see Fig. 6-4). The experimentally measured frequency in the laboratory frame is affected by the Doppler Effect and equals to the mode frequency plus the Doppler shift due to E×B drift velocity, i.e.

$$f_{lab} = f_{\mathrm{mode}} + f_{\mathrm{E\times B}} \text{ and } f_{\mathrm{E\times B}} = \frac{k_\theta}{2\pi}\frac{E_r}{B_\phi}, \tag{6.1}$$

where k_θ is the poloidal wavenumber and E_r is the radial electric field. Thus, the decrease of the frequency broadening suggests a corresponding change in the mode frequency f_{mode}, the mode wavenumber k_θ, or the radial electric field, since the toroidal magnetic field $\overline{n}_e$ B_ϕ is kept constant throughout the whole discharge. After the addition of the on-axis ICRF heating, the intensities of broadband turbulence with frequencies below 80 kHz (see Fig. 6-3d) and QC modes (see Fig. 6-3c) increase, while the intensity of broadband turbulence with frequencies above 200 kHz (see Fig. 6-3b) remains the same.

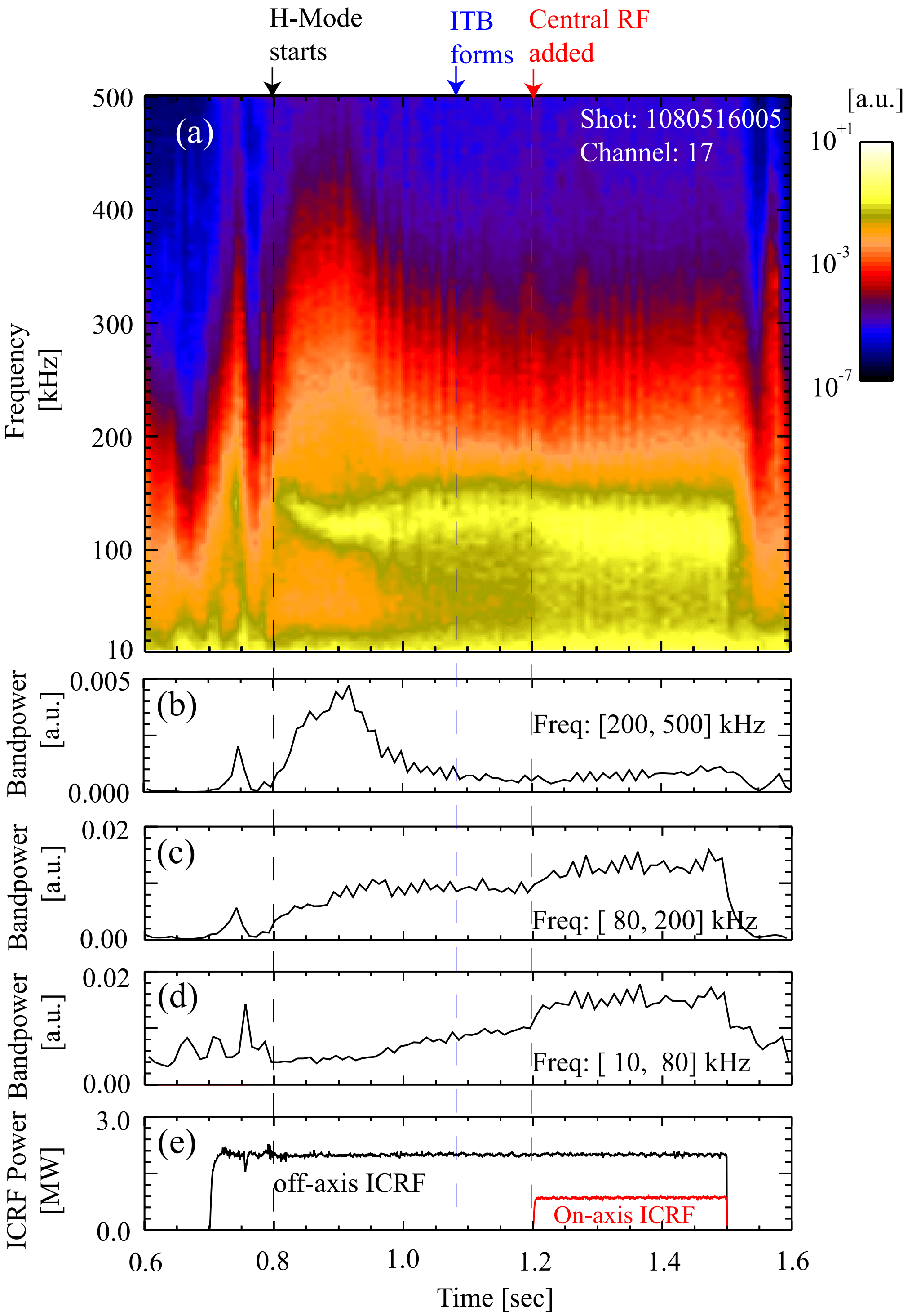

Figure 6-3: (a) Spectrogram of a core PCI channel (17) vs. time. Time resolution is 10 ms and frequency resolution is 5 kHz. (b) Time trace of the integrated fluctuation intensity over the frequency range of 200-500 kHz. (c) Time trace of the integrated fluctuation intensity over the frequency range of 80-200 kHz. (d) Time trace of the integrated fluctuation intensity over the frequency range of 10-80 kHz. (e) Time traces of on-axis (black) and off-axis (red) ICRF power.

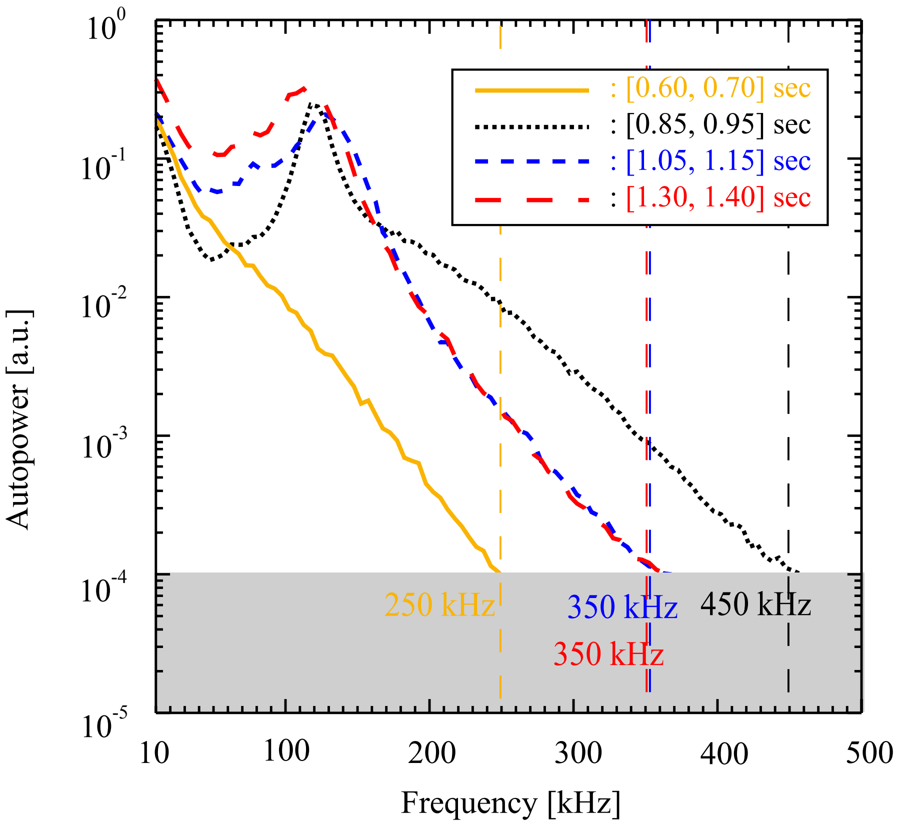

Figure 6-4: Frequency spectra of a core PCI channel (17): the orange curve is averaged over the time window of 0.60-0.70 sec, corresponding the L-Mode plasma before the L-H transition; the black curve is averaged over the time window of 0.85-0.95 sec, corresponding to the H-Mode plasma before the ITB onset; the blue curve is averaged over the time window of 1.05-1.15 sec, corresponding to the ITB plasma with only off-axis ICRF heating; and the red curve is averaged over the time window of 1.30-1.40 sec, corresponding to the ITB plasma after adding on-axis ICRF heating. The defined visible frequencies at the signal level of 10^{-4} are also labeled for each curve.

The frequency/wavenumber spectra can be obtained through the two-dimensional Fourier transform, where the propagating direction of the measured turbulence is also resolved with the localizing configuration. Figure 6-5 shows how the mode propagating direction is inferred by comparing the measured frequency/wavenumber spectra with the different localizing configurations. In Fig. 6-5(a), the masking plate was set up primarily to view the bottom of the plasma column, and we see that the positive wavenumber QC at frequency ~140 kHz and wavenumber ~4 cm^{-1} dominates. In Fig. 6-5(b), the masking plate was set up mainly to view the top of the plasma column in a similar discharge, and it is seen that the negative wavenumber QC mode dominates. This measurement agrees with the fact that the QC mode propagates in the electron diamagnetic direction.[54] Early studies also show that the QC mode propagates perpendicular to the magnetic field just as the electrostatic turbulence, which validates the use of the localizing procedure, since the localization requires that the wavevectors of the measured turbulence are mainly perpendicular to the field lines, i.e., $\mathbf{k}\cdot\mathbf{B}\approx 0$. Similar analysis of the frequency/wavenumber spectra in Fig. 6-6 shows that the broadband turbulence in the frequency range of 200-500 kHz propagates in the ion diamagnetic direction, where the measured frequency is dominated by the Doppler shift due to E×B drift velocity.

The PCI measurements are averaged over 0.1 sec to reduce the statistical uncertainty while turbulence is still evolving within the averaging time range, which causes the ripple patterns as shown in Fig. 6-5(a). The comparisons with nonlinear gyrokinetic simulations in Sec. 6-5 show that the broadband turbulence is consistent with the ITG turbulence.

The masking system also suppresses the broadband turbulence in the frequency range of 200-500 kHz more strongly than the QC mode. As shown in Fig. 6-5(b), for the top plasma view, the ratio of intensity of the broadband turbulence in the negative wavenumber to that in the positive wavenumber is 4.5, while the ratio of intensity of the QC mode in the positive wavenumber to that in the negative wavenumber is 1.5. Since the top/bottom differentiation is better for the broadband turbulence than for the QC mode, the broadband turbulence has to be localized further radially inward where the magnetic pitch angle is greater.

The phase velocity v_{ph} of the measured turbulence can also be calculated from the frequency/wavenumber spectra, i.e.

$$\mathrm{v}_{ph} = \frac{2\pi f}{k}. \tag{6.2}$$

The calculated phase velocity is shown on frequency/wavenumber spectra. As shown in Fig. 6-5, in the plasma before the ITB formation, the phase velocity of the broadband turbulence is ~4 km/sec. As shown in Fig. 6-6, in the plasma after the ITB formation, the phase velocity of the broadband turbulence is reduced to 2 km/sec. As shown in Fig. 6-7, in the plasma during the ITB control with the on-axis ICRF heating, the phase velocity of the broadband turbulence remains 2 km/sec.

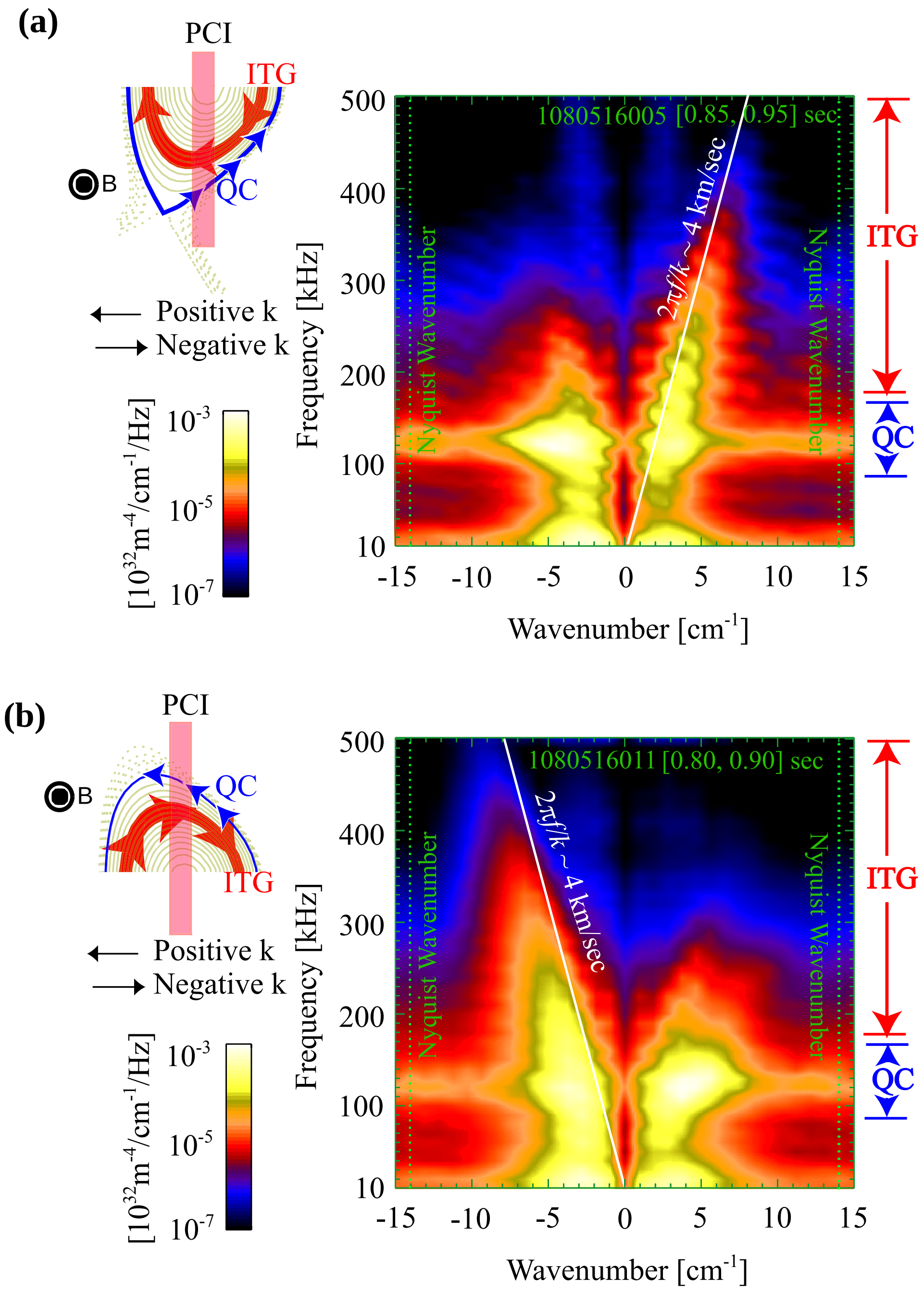

Figure 6-5: Frequency/wavenumber spectra of plasma fluctuations measured by PCI in the H-mode plasma before the ITB formation. On the left-corner of each plot, the diagnostic line-of-sight is shown according to the masking phase plate setup: (a) the bottom plasma view (Shot #: 1080516005; time window: [0.85, 0.95] sec), (b) the top plasma view (Shot #: 1080516011; time window: [0.80, 0.90] sec).

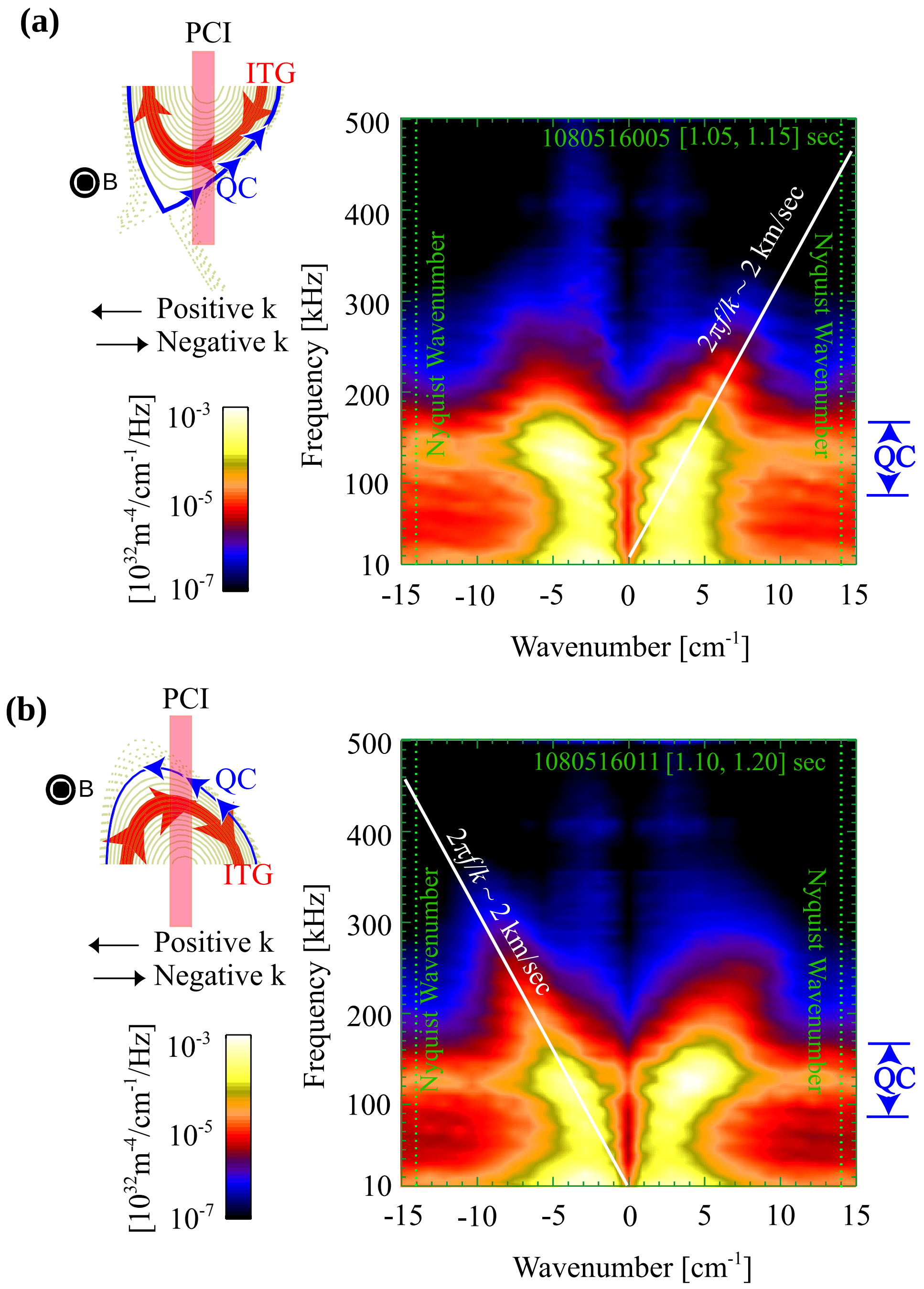

Figure 6-6: Frequency/wavenumber spectra of plasma fluctuations measured by PCI in the ITB plasma with only off-axis ICRF heating. On the left-corner of each plot, the diagnostic line-of-sight is shown according to the masking phase plate setup: (a) the bottom plasma view (Shot #: 1080516005; time window: [1.05, 1.15] sec), (b) the top plasma view (Shot #: 1080516011; time window: [1.10, 1.20] sec).

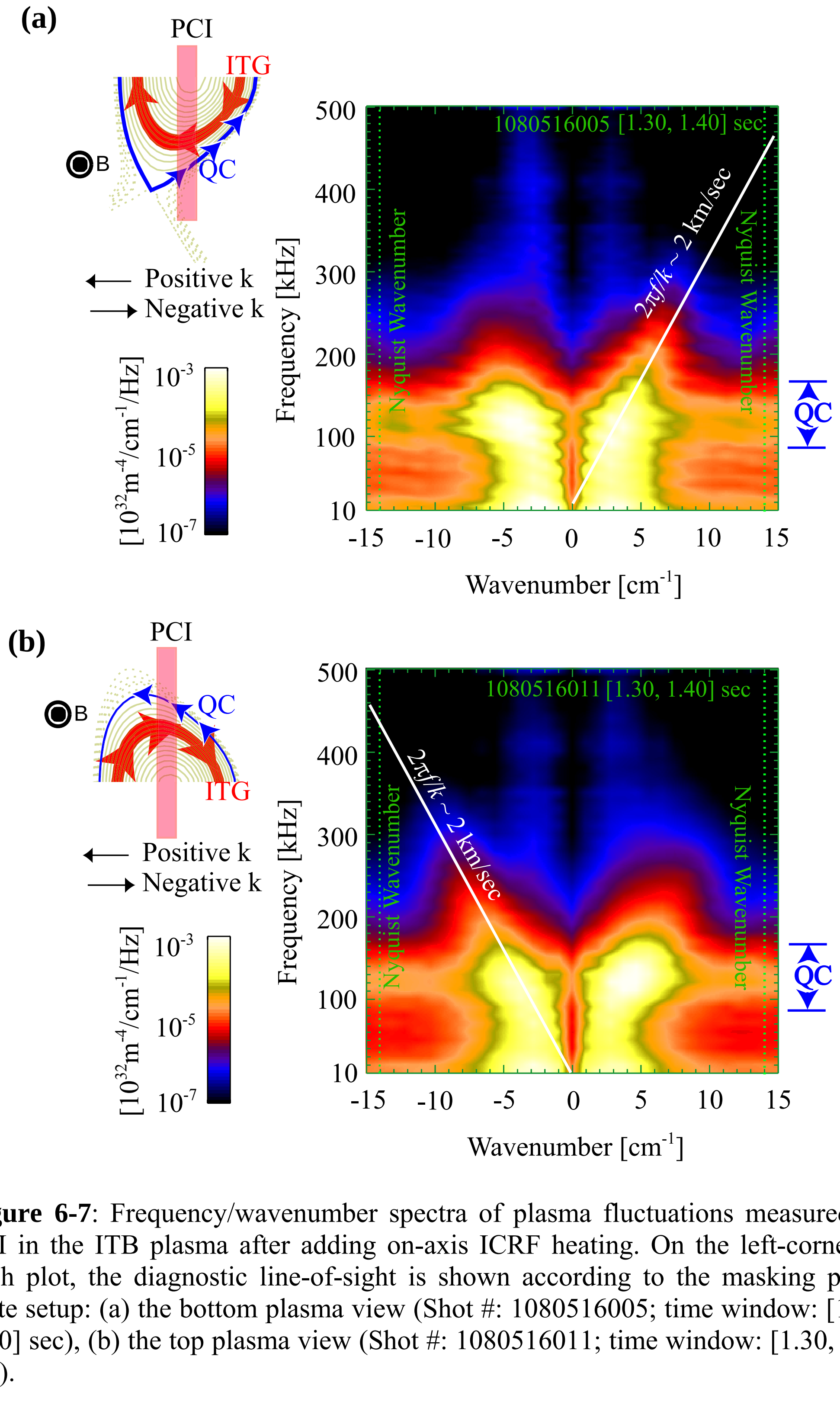

Figure 6-7: Frequency/wavenumber spectra of plasma fluctuations measured by PCI in the ITB plasma after adding on-axis ICRF heating. On the left-corner of each plot, the diagnostic line-of-sight is shown according to the masking phase plate setup: (a) the bottom plasma view (Shot #: 1080516005; time window: [1.30, 1.40] sec), (b) the top plasma view (Shot #: 1080516011; time window: [1.30, 1.40] sec).

The comparison with the measured electric field indicates that the change of the phase velocity is due to the reduction of the E×B Doppler shift. In Alcator C-Mod, the high resolution spectroscopy (Hirex) diagnostic[109] measures the density (n_I), temperature (T_I), flow velocity (V_θ and V_ϕ) of the Ar^{+17} impurity. The radial electric field (E_r) can be calculated through the force balance equation E_r

$$E_r = \frac{\nabla p_I}{e n_I Z_I} - V_\theta B_\phi + V_\phi B_\theta \,, \tag{6.3}$$

where $p_I = n_I T_I$. Unfortunately, the Hirex diagnostic was not well calibrated in the studied plasmas and the absolute value of E_r was not available. To eliminate the arbitrary offset, we only consider the relative change of , i.e.

$$\Delta E_r(t) = E_r(t) - E_r(t_0) \,, \tag{6.4}$$

where $t_0 = 0.85\ \mathrm{sec}$ corresponding to the non-ITB H-Mode plasma. As shown in Fig. 6-8, the radial electric fields shows a 10±3 kV/m decrease at $0.73\ \mathrm{m} < R < 0.80\ \mathrm{m}$ after the ITB forms, which will cause 2±0.6 km/sec reduction of the phase velocity of the measured fluctuation. Here, only $0.35 < r/a < 0.65$ is considered since our gyrokinetic analysis in Sec. 6-4 shows no unstable drift-wave turbulence for $r/a < 0.35$. Moreover, since the ITB tends to create an impurity pinch and causes all the Ar^{+17} impurity to accumulate in the core, there is not enough Ar^{+17} left outside for the Hirex diagnostic to make the measurements. Therefore, the Hirex measurements do not extend out past $r/a = 0.65$ during the ITB, which also approves the existence of an ITB.

Because of the reduced radial electric field after the ITB formation, the reduced E×B Doppler shift is not enough to separate the core and edge turbulence in the frequency domain below 250 kHz; thus, the broadband turbulence (propagating in the ion direction in the H-mode) is mixed together with the edge localized QC modes (propagating in the electron direction). Since the intensity of the broadband turbulence is weaker than that of the QC mode, it will be overwhelmed and the PCI diagnostic cannot resolve its direction of propagation.

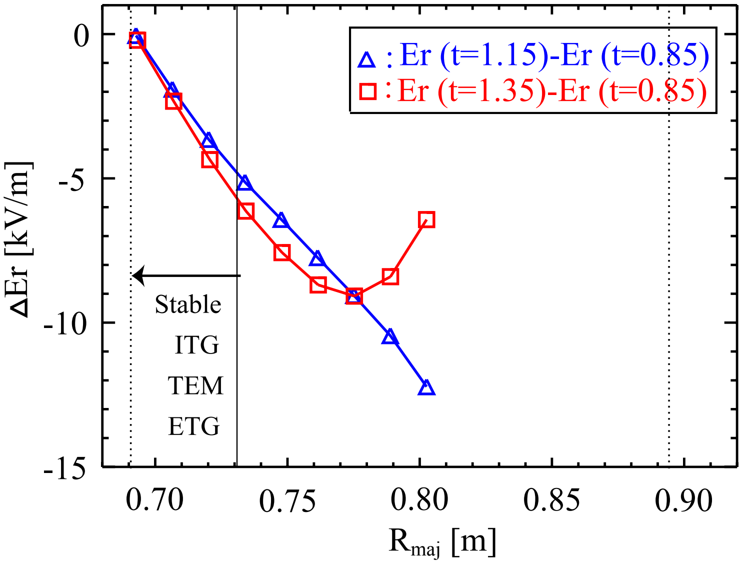

Figure 6-8: Change of the radial electric field profile after the ITB forms, where the blue triangles correspond to the ITB with only off-axis ICRF heating and the red squares correspond to the ITB after adding on-axis ICRF heating. Two vertical dashed lines are the magnetic axis and last closed flux surface (LCFS), respectively.

6.4 Gyrokinetic Simulation of Turbulent Transport

To further explore the nature of turbulence and the drive mechanism of thermal transport, we have used GYRO to simulate turbulence and transport. While GYRO can include electromagnetic effects, the electrostatic approximation is assumed for all the simulations here, since electromagnetic effects are found to be negligible in low-β plasmas ($\beta_T \lesssim 0.3\%$).

In our simulation, the input file is prepared from the output of TRANSP[89] using the data translator (trgk) developed at PPPL. Both linear stability analysis and nonlinear (local and global) simulation has been performed. The key plasma parameters used the gyrokinetic analysis are defined as follows:

$$a / L_{Ti} = -\frac{a}{T_i}\frac{dT_i}{dr}, \;\; a / L_{Te} = -\frac{a}{T_e}\frac{dT_e}{dr}, \tag{6.5}$$

$$a / L_{n_i} = -\frac{a}{T_i}\frac{dT_i}{dr}, \;\; a / L_{n_e} = -\frac{a}{T_e}\frac{dT_e}{dr}, \tag{6.6}$$

$$\rho_s = \frac{c_s}{\Omega_i}, \tag{6.7}$$

where $c_s = (T_e / m_i)^{1/2}$ is the ion sound speed, $\Omega_i = eB_\phi / m_i$ is the ion cyclotron frequency, and m_i is the ion mass.

The ion temperature profile is taken to be same as the electron temperature profile (Fig. 6-2b), since the electrons and ions are strongly coupled due to collisions at such high electron density. The TRANSP analysis also calculates an ion temperature profile which is consistent with the neutron measurement[110]. The calculated ion temperature is close to the electron temperature, which validates the assumption of $T_e = T_i$. Although the Hirex diagnostic can also measure the ion temperature profile, the measured profile does not extend out past $r / a = 0.65$ as discussed in Sec. 6-3. However, the measured ion temperature inside $r/a = 0.65$ is close to the electron temperature, which also validates the assumption of $T_e = T_i$.

6.4.1 Linear Stability Analysis

Linear stability calculation shows that the ion temperature gradient (ITG) mode is the most unstable mode and the trapped electron modes (TEM) are typically stable in the plasma core ($0.3 < r/a < 0.8$) before and during ITB formation, as shown in Fig. 6-9. As an example, the calculated growth rate and frequency spectra covering the wavenumber range of $0.1 < k_\theta \rho_s < 0.8$ are shown in Fig. 6-10, where the simulation parameters are taken at $r/a = 0.6$ in the non-ITB H-Mode plasmas with $a/L_{Ti} = a/L_{Te} = 2.15$ and $a/L_{ni} = a/L_{ne} = 0.16$. The growth rate spectrum typically peaks at $k_\theta \rho_s \sim 0.4$, The frequency of the unstable modes is proportional to $k_\theta \rho_s$ and the modes propagate in the ion diamagnetic direction.

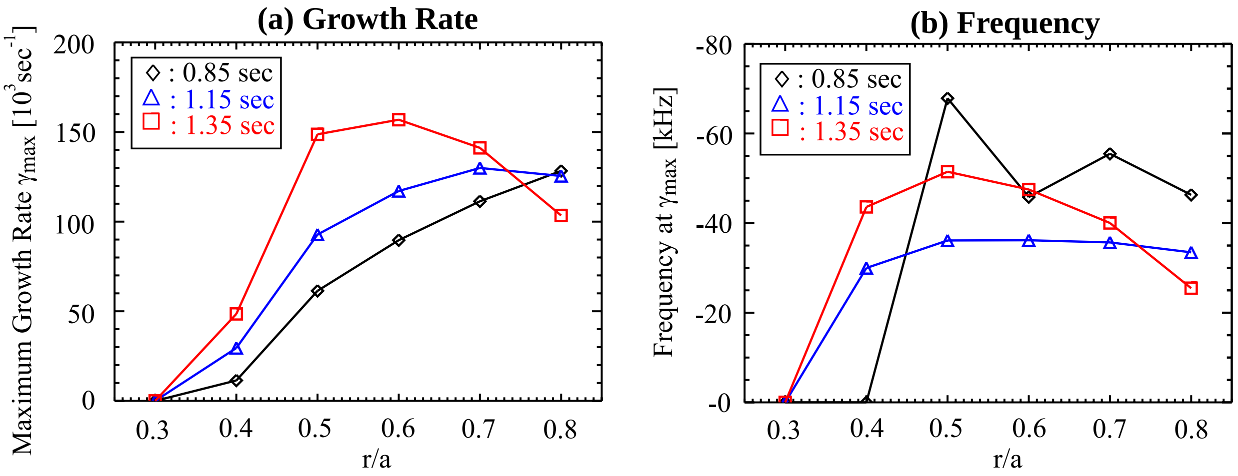

Figure 6-9: Profiles of the maximum growth rate (a) and the frequency at the maximum growth (b), where black diamonds correspond to the plasma before the ITB onset, blue triangles correspond to the ITB plasma with only off-axis ICRF heating, and red squares correspond to the ITB plasma after adding on-axis ICRF heating.

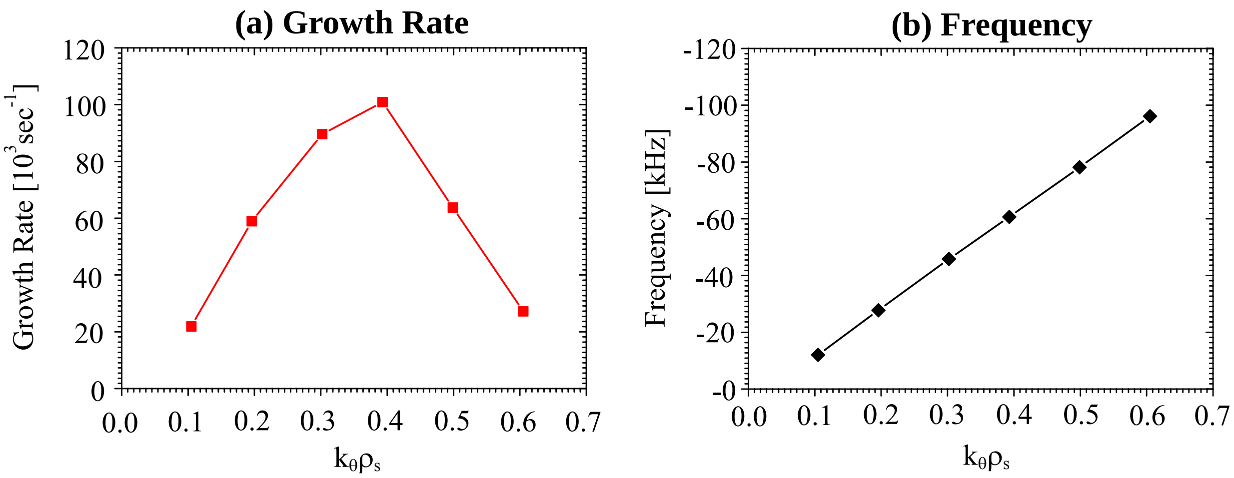

Figure 6-10: Growth rate (a) and frequency (b) spectra of the ITG mode. The parameters in the linear analysis are taken at $r/a = 0.6$ in the non-ITB H-Mode plasmas, where $a/L_{Ti} = a/L_{Te} = 2.15$, $a/L_{ni} = a/L_{ne} = 0.16$.

To study the impact of varying the density and temperature gradient on the mode frequency and growth rate, we have carried a 21×21 linear runs in the plane of a/L_n - a/L_T. The ion temperature T_i is assumed to be same as the electron temperature T_e and the ion density is also assumed to be the same as the electron density n_e, i.e. $T_i = T_e$ and $n_i = n_e$; thus no impurity species is included. These 21×21 linear runs cover $0.0 \le a/L_n \le 4.0$ and $0.0 \le a/L_T \le 4.0$ with an even grid size. The results are summarized in Fig. 6-11. There are three distinct zones on the diagrams:

1. for $a/L_n \lesssim 1$ and $a/L_T \lesssim 1$, both ITG and TEM are stable;
2. for $a/L_n \lesssim 0.45\times a/L_T + 1.0$ and $a/L_T \gtrsim 1.0$, ITG is the most unstable mode;
3. for $a/L_n \gtrsim 0.45\times a/L_T + 1.0$ and $a/L_T \gtrsim 1.0$, TEM is the most unstable mode.

In principle, the TEM can be destabilized when the density is steep. However, for the measured density gradient ($a/L_n = 0.16$ at $r/a = 0.6$ in the non-ITB plasma and $a/L_n = 0.8$ at $r/a = 0.6$ in the ITB plasma), the TEM remains stable even after reducing a/L_T until the ITG mode is completely stabilized.

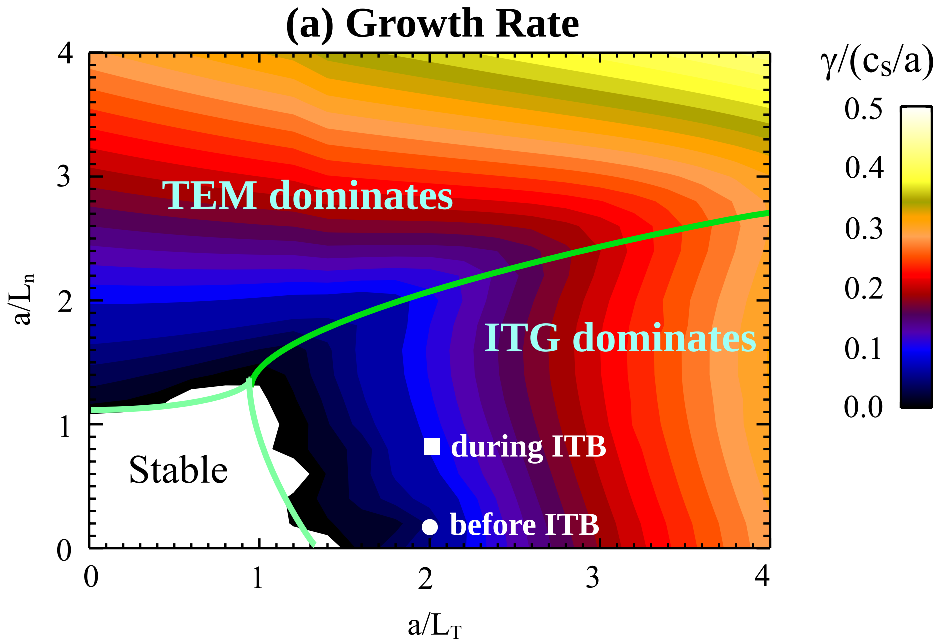

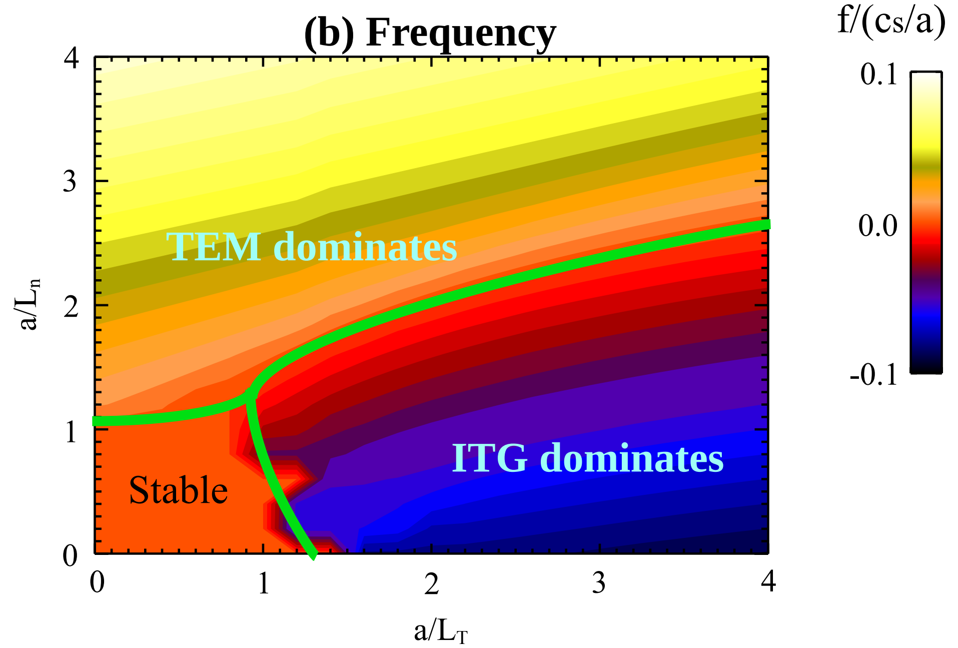

Figure 6-11: Contour plots of the growth rate (a) and the frequency (b) in the a/L_n - a/L_T plane. The linear stability calculation is performed at $k_\theta \rho_s \sim 0.4$. The other parameters are taken from $r/a = 0.6$ in the non-ITB H-Mode plasma. Both the frequency and the growth rate are shown in the scale of $c_s/a = 8.8\times10^5$ sec^{-1}. The experimental measurements of a/L_n and a/L_T before ITB and during ITB are also marked on the contour plot of the growth rate.

We have also carried out a detailed linear stability analysis in the electron temperature gradient (ETG) regime. The analysis covers the poloidal wavenumber in the range of $1.0 \lesssim k_\theta \rho_s \lesssim 50$. The calculated wavenumber and frequency spectra are shown in Fig. 6-12, where the growth rate spectrum peaks at $k_\theta \rho_s \sim 25$ and the frequency is linearly proportional to $k_\theta \rho_s$. Since the electron Larmor radius ρ_e is $1/60$ of the ion Larmor radius $\rho_i = \rho_s$ when $T_i = T_e$, the growth rate spectrum of the ETG mode peaks at $k_\theta \rho_e \sim 0.4$ while the growth rate spectrum of the ITG mode peaks at $k_\theta \rho_i \sim 0.4$. Therefore, the ETG mode is essentially similar to the ITG mode with electrons and ions interchanged. In addition, the frequency of the most unstable ETG mode with the maximum growth rate is $\sim \omega_{*e} / 2\pi \sim 3\ \text{MHz}$ while the frequency of the most unstable ITG is $\sim \omega_{*i} / 2\pi \sim -55\ \text{kHz}$, where ω_{*i} and ω_{*e} are the ion and electron diamagnetic frequency, respectively. The frequencies from the linear stability analysis of the ITG and ETG roughly follow the analytical calculation in Chapter 2. Furthermore, as shown in Fig. 6-13, the ETG mode becomes stable after reducing a / L_{Te} below ~ 1.4, which is very similar to the fact that the ITG mode becomes stable after reducing a / L_{Ti} below ~ 1.3 (see Fig. 6-11). Further analysis at other radii shows that the ETG remains unstable across the domain of $r / a > 0.4$.

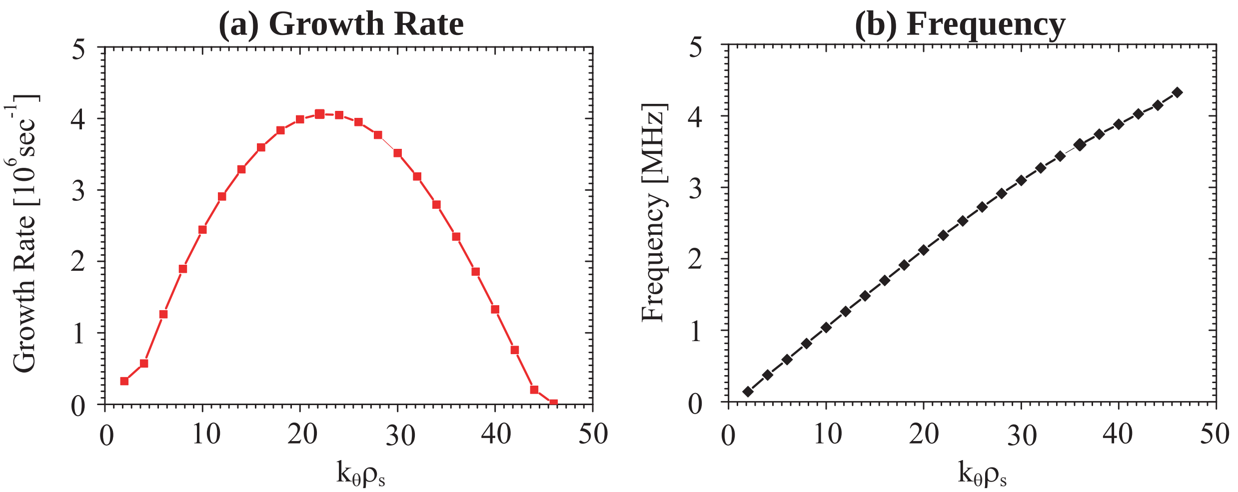

Figure 6-12: Growth rate and frequency spectra of ETG. The parameters in the linear analysis are taken at $r/a = 0.6$ in the non-ITB H-Mode plasmas.

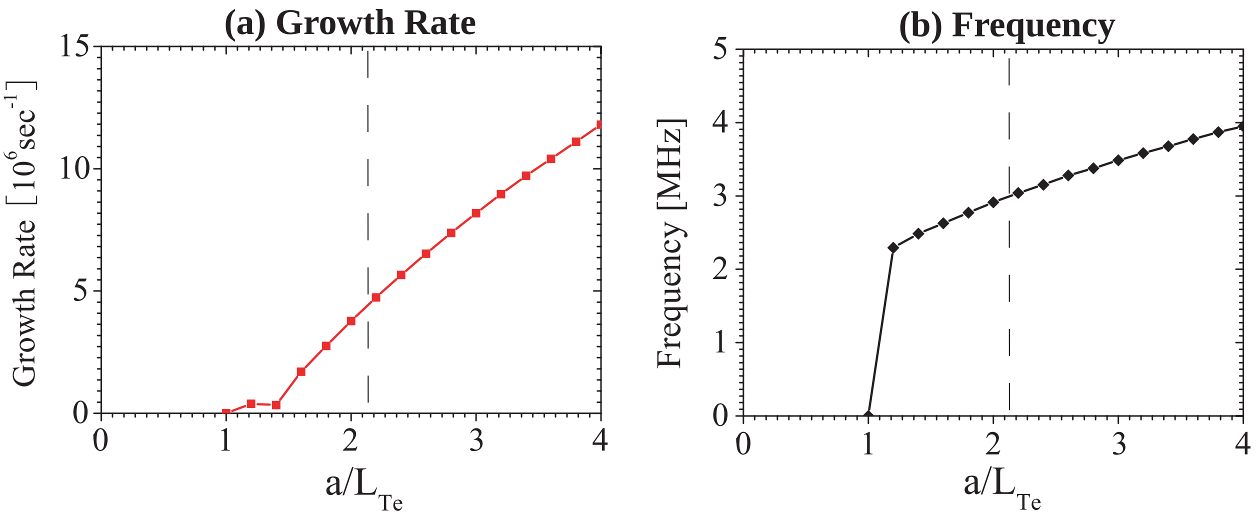

Figure 6-13: Growth rate (a) and frequency (b) of the ETG mode at $k_\theta\rho_s \sim 25$ vs. a/L_{Te}, where the dashed line marks the experimental measured a/L_{Te}.

The above linear stability analysis reveals the most unstable mode; however, it does not contain the necessary physics to saturate turbulence and resolve the induced thermal diffusivities in the fully developed nonlinear state. Although an estimated thermal diffusivity can be obtained through the quasilinear theory, the nonlinear simulation is necessary for a quantitative prediction of turbulence and transport, which is also essential in the code validation.

6.4.2 Nonlinear Simulations

To simulate turbulence and associated transport, we have performed extensive nonlinear gyrokinetic simulations. All simulations are done with the real mass ratio ($m_i / m_e \approx 3600$) and kinetic electrons. Time integration is done with a fourth-order Runge-Kutta algorithm on the nonlinear terms combined with a second-order implicit-explicit scheme on linear electron physics. A standard 128-point velocity space discretization is used, which includes 8 points in pitch angle, 8 points in energy, and 2 signs of velocity. The uncertainty of analyzing the electron thermal diffusivity χ_e and the ion thermal diffusivity χ_i separately is large when T_i is close to T_e;[122] hence, we only discuss the effective thermal diffusivity χ_{eff} here.

Seven nonlinear simulations (five local and two global simulations) with no equilibrium E×B shear and no parallel velocity were performed for each case. Our nonlinear GYRO simulations include N_n modes with a toroidal separation of Δn. Unless otherwise specified, the global simulations in this chapter include 16 modes evenly spaced between $0.0 \lesssim k_\theta \rho_s \lesssim 0.8$ at $r / a = 0.6$ and cover the plasma domain of $0.4 \lesssim r / a \lesssim 0.8$, while the local simulations include 12 modes evenly spaced between $0.0 \lesssim k_\theta \rho_s \lesssim 0.8$.

The comparisons between the experimentally measured and simulated thermal diffusivities are shown in Fig. 6-14: (a) before the ITB onset; (b) during the ITB. The simulated turbulent transport agrees well with experiments in non-ITB plasmas, while it is larger than experimental measurements in ITB plasmas with only off-axis ICRF heating.

Convergence studies are tedious but necessary in the nonlinear simulations. Here, we have performed two types of convergence studies on the mode numbers and domain sizes. As shown in Fig. 6-14(a), two global simulations with different set of modes ($N_n = 28$, $\Delta n = 5$ vs. $N_n = 16$, $\Delta n = 10$) agree well with each other. As also shown in Fig. 6-14(b), global simulations with different box sizes ($480\rho_s$ vs. $320\rho_s$) match well in the overlapped domain $0.4 < r/a < 0.68$.

To compare the global and local simulations, we have also perform five local simulations at $r/a = 0.4$, 0.5 , 0.6 , 0.7 , and 0.8 for the plasmas before the ITB onset and during the ITB, respectively, as shown in Figs. 6-14a and 6-14b. Our studies also show robust consistency between nonlinear global and local flux-tube simulations at almost all radial positions.

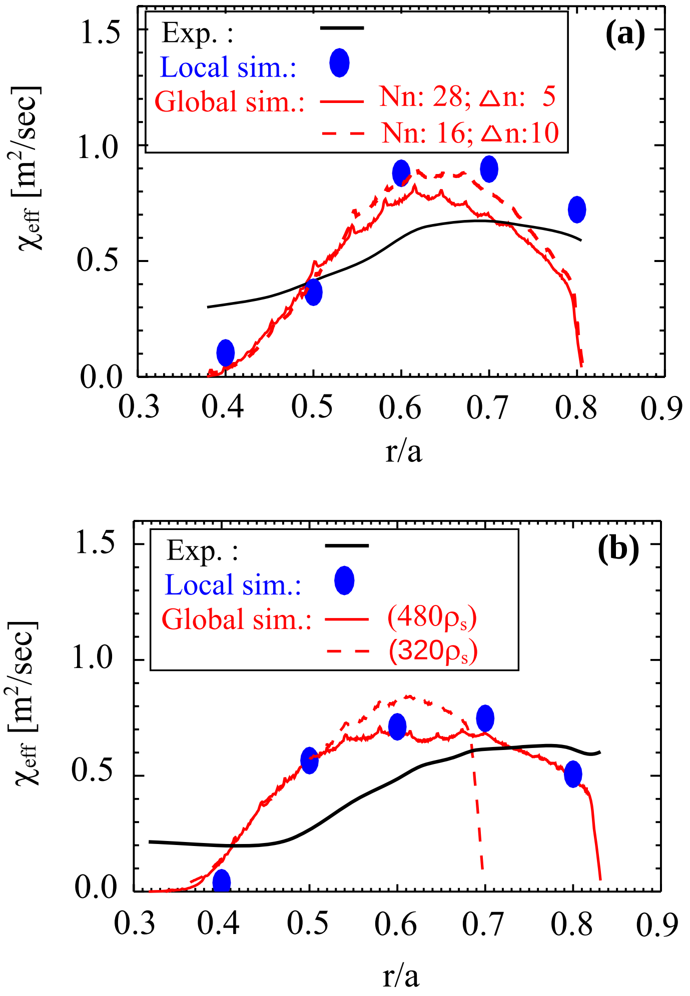

Figure 6-14: Comparison of experimental and nonlinearly simulated thermal diffusivities: (a) before the ITB onset, where two global simulations covering different set of modes ($N_n = 28$, $\Delta n = 5$ vs. $N_n = 16$, $\Delta n = 10$) and five local simulations are shown; (b) during the ITB with only off-axis ICRF heating, where two global simulations with different domain sizes ($480\rho_s$ vs. $320\rho_s$) and five local simulations are shown.

As an example, the effective diffusivity spectrum from the local nonlinear simulation at r/a of the H-Mode plasma before the ITB onset is shown in Fig. 6-15, where the simulating parameters are the same as those used in the linear stability analysis as shown in Fig. 6-10. The non-linear spectrum of the ITG mode peaks $k_\theta \rho_e \sim 0.25$ while the linear spectrum peaks at $k_\theta \rho_s \sim 0.4$. The nonlinear spectral downshift of the ITG mode is generally attributed to the nonlinear toroidal coupling effect, which causes the transfer of energy to modes with low toroidal mode numbers and damps the modes with high toroidal mode numbers, thereby resulting in the spectral downshift.

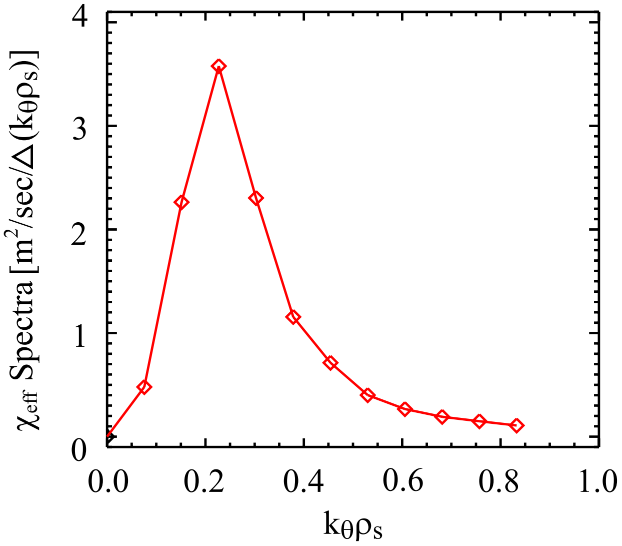

Figure 6-15: Effective diffusivity spectrum of the ITG mode from a local nonlinear simulation. The simulating parameters are taken at $r/a = 0.6$ in the non-ITB H-Mode plasmas, where $a/L_{Ti} = a/L_{Te} = 2.15$, $a/L_{ni} = a/L_{ne} = 0.16$.

To further investigate the discrepancy in ITB plasmas, we have studied the impact of varying the ion temperature gradient, as is done in other studies[123]. Decreasing a/L_{Ti} by 15% from the baseline parameter, as shown in Fig. 6-16, is sufficient to reduce the simulated effective thermal diffusivity χ_{eff} to the experimental level at r/a=0.6.

It is also well known that E×B shear can also suppress the simulated transport.[112] Simply speaking, E×B shear reduces the thermal transport through reducing the radial correlation of turbulent eddies or modifying the phase between potential and density/temperature perturbations.

In a nonlinear global simulation, GYRO can include an artificial E×B shear rate, which is defined as

$$\gamma_E = \left(\frac{r}{q}\right)\frac{\partial\left(q\mathrm{v}_{E\times B}/r\right)}{\partial r}. \tag{6.8}$$

We have used global GYRO to nonlinearly examine the impact of E×B shear on the turbulent transport. As shown in Fig. 6-17, adding a ~30 kHz E×B shear rate lowers the simulated effective thermal diffusivity χ_{eff} to the experimental level. Considering the fact that experimental uncertainty of the ion temperature gradient (a/L_{Ti}) measurements is above 20% and that E×B shear rates (γ_E) are not yet well measured in Alcator C-Mod, the discrepancy between the experimentally measured and simulated transport in the ITB plasma can be attributed to the experimental uncertainty.

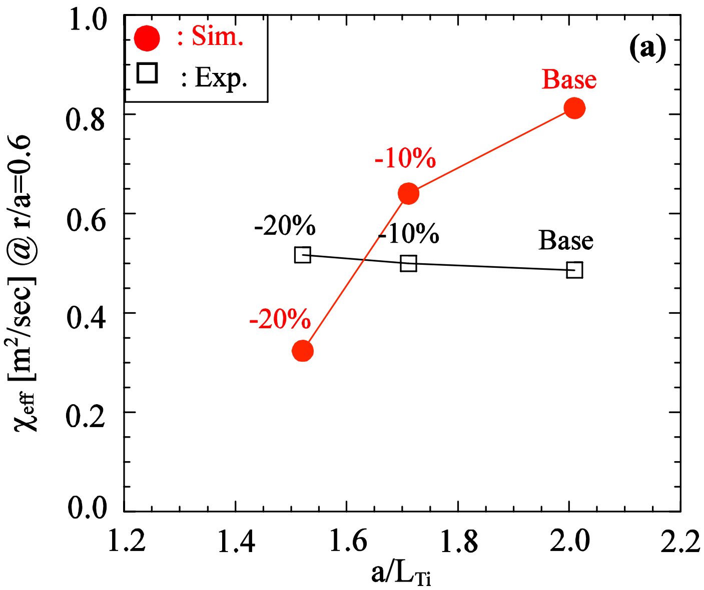

Figure 6-16: Impact of varying a correction factor applied to the measured ion temperature gradient in the ITB plasma with only off-axis ICRF heating, where the a/L_{Ti} of the base case is taken from the smoothed temperature profiles as shown in Fig. 6-2(b).

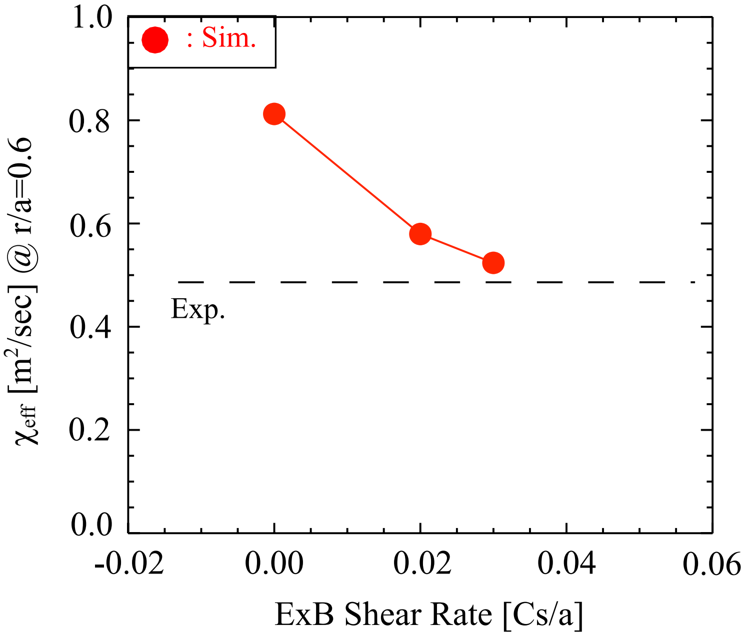

Figure 6-17: Effect of the E×B shear on turbulent transport in the ITB plasma with only off-axis ICRF heating, where the E×B shear rate γ_E is in the scale of $c_s / a = 9 \times 10^5 \text{ sec}^{-1}$.

The impact of varying density gradients on turbulent transport has also been studied. The result is shown in Fig. 6-18, where it is found that the density gradient variation has a weak impact on turbulent transport. The simulated transport can only be reduced to the experimental level and the TEM becomes significant after increasing the a / L_n by at least a factor of two, which is outside the experimental error bars based on Thomson Scattering data such as shown in Fig. 6-2(a). Thus, for the measured temperature and density profiles, significant thermal transport contribution from the TEM is not likely.

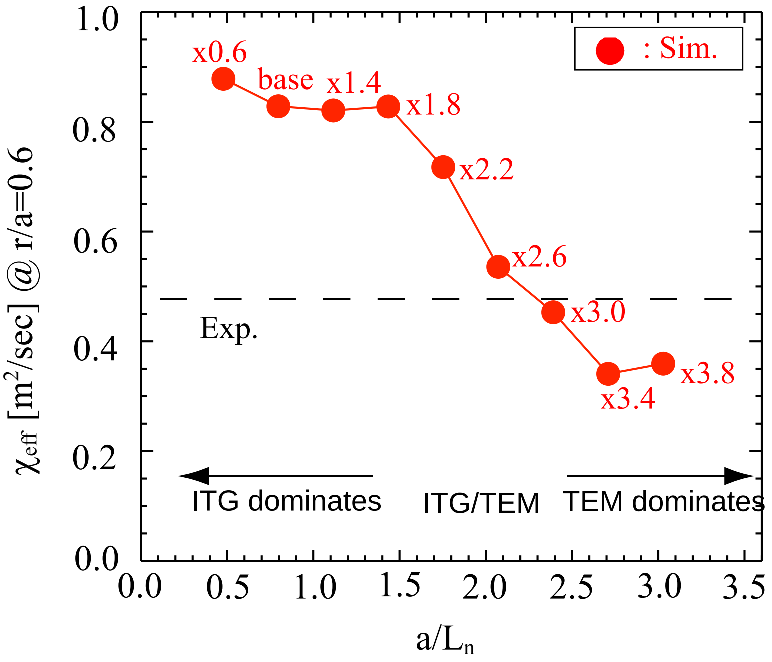

Figure 6-18: Impact of varying a correction factor applied to the measured density gradient on turbulent transport in the ITB plasma with only off-axis ICRF heating, where the a / L_n of the base case is taken the smoothed electron profile as shown in Fig. 6-2(a).

Although the TEM is unlikely to contribute significant thermal transport, it is meaningful to compare the effective thermal diffusivity spectra from nonlinear simulations at various density gradients. As shown in Fig. 6-19, the peak and the width of nonlinear spectra vary as the density gradient changes. To quantity the variation, a Gaussian fitting is used to fit the simulated spectra. The fitted center k_0 and width k_w are shown in Fig. 6-20. As shown in Fig. 6-20(a), as the density gradient increases, the peak of the nonlinear spectrum shifts toward the larger $k_\theta \rho_s$, where it peaks at $k_\theta \rho_s \sim 0.25$ when the ITG mode is the dominant turbulence and peaks at $k_\theta \rho_s \sim 0.5$ when the TEM is the dominant turbulence. The change of the width of the nonlinear spectra is not as uniform as that of the peak. As shown in Fig. 6-20(b), the width decreases from $k_\theta \rho_s \sim 0.1$ to $k_\theta \rho_s \sim 0.08$ when the density gradient increases and the TEM becomes significant.

After the TEM becomes the dominant turbulence, the width increases from $k_\theta \rho_s \sim 0.08$ to $k_\theta \rho_s \sim 0.14$.

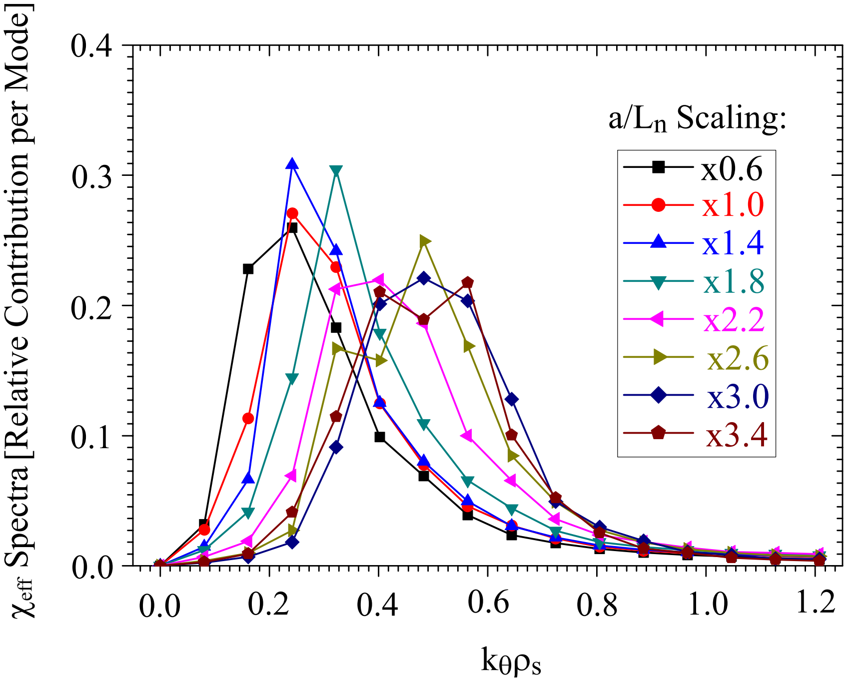

Figure 6-19: Effective diffusivity spectra at various scaling of the measured density gradient.

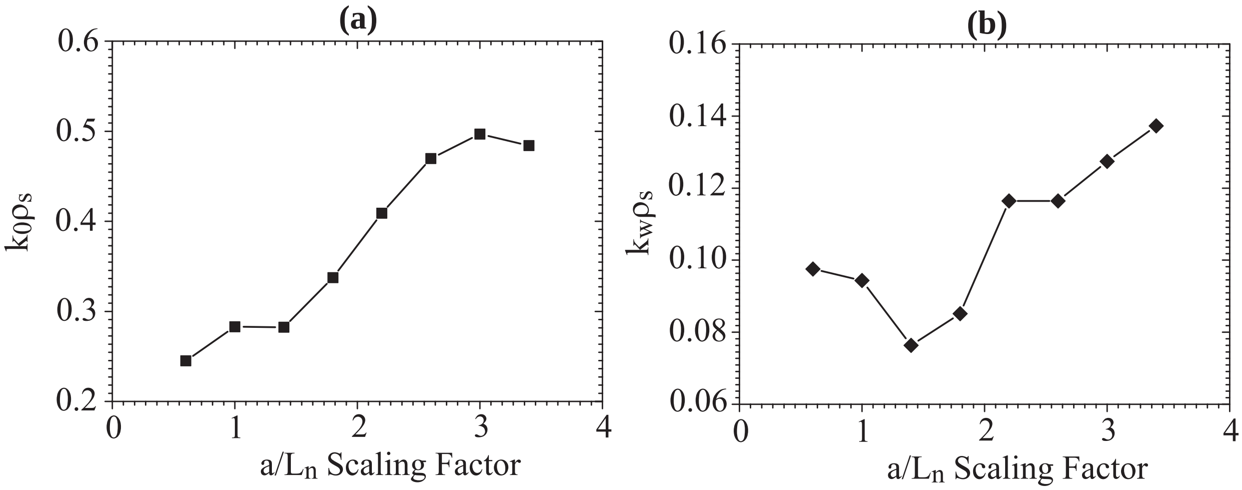

Figure 6-20: (a) k_0 vs. a/L_n scaling; (b) k_w vs. a/L_n scaling, where k_0 and k_w of the center and width of the Gaussian fitting.

Regarding transport studies in the ETG range, we have not had access to computer capabilities that are necessary for nonlinear GYRO simulation of such turbulence. In addition, recent GYRO simulations for DIII-D plasmas indicated that high-k ETG turbulence could account for only 10% of the total electron transport.[113] Significant contribution from the ETG turbulence is unlikely in the presence of the strong ITG turbulence in the H-Mode regime. It is interesting that $\chi_e \approx \chi_i$ can be produced nonlinearly from the ITG turbulence in H-Mode high density plasmas even when TEM modes are linearly stable. This fact has already been noted by Waltz and Candy in their previous GYRO simulations.[85]

6.5 Comparison between Fluctuation Measurements and GYRO Predictions

Besides thermal transport, nonlinear GYRO simulations also predict turbulence. The direct and quantitative comparison between experimentally measured and simulated turbulence in C-Mod is rather difficult. This is partially caused by the limited diagnostic capability and access. For example, PCI measures line-integrated density fluctuations with an instrumental limit primarily in the wavenumber response. The synthetic PCI discussed in Chapter 4 analyzes the density fluctuation output of the GYRO global nonlinear simulation and emulates the experimental PCI measurements by line-integrating the density fluctuations, i.e., $\int \tilde{n}(z)dz$. Thus, it allows for a direct and quantitative comparison between numerical simulation and experimental measurements.

The synthetic PCI frequency/wavenumber diagram in the non-ITB plasma is shown in Fig. 6-21(a). A flat $v_{E\times B}$=4.0 km/sec has been added to account for the unmeasured Doppler shift. To emulate the top view configuration of the masked phase plate, a weight function $w(z)$ is added when performing line integral of density fluctuations, i.e., $\int w(z)\tilde{n}(z)dz$. Comparing the synthetic PCI from Fig. 6-21(a) with the experimental measurement in Fig. 6-5(a), the intensity of the simulated turbulence is lower than the experimental measurement in the frequency below 300 kHz, where the PCI measurements begin to be dominated by the edge turbulence. However, as shown in Fig. 6-21 (b), the fluctuation spectrum measured by PCI above 300 kHz agrees well with the ITG turbulence in GYRO simulation within experimental uncertainty, including the direction of propagation, wavenumber spectrum, and absolute intensity. GYRO only simulates one time point, where the equilibrium profiles are fixed, while the experimental measurements cover 0.1 sec. The variation of the density and temperature profiles within 0.1 sec will broaden the experimental measurements. Therefore, the synthetic PCI spectra appear to be narrower in wavenumber than the experimental spectra. Moreover, in the synthetic PCI analysis, a flat $v_{E\times B}$ is introduced to account for the unmeasured Doppler shift. The potential variation of $v_{E\times B}$ along the integration chord will also cause a different Doppler shift for the turbulence with the same wavenumber, thereby broadening the experimental spectra.

After the ITB formation, the core and edge turbulence is mixed together on PCI due to the reduced E×B Doppler shift in the core; thus, as shown in Fig. 6-22, the synthetic PCI spectra (the base case simulation with no reduction of the ion temperature gradient or E×B shear suppression), where $v_{E\times B}$=2.0 km/sec has been added for the Doppler shift, shows weaker fluctuation intensity than the PCI measurements (Fig. 6-6(a)) which also include contributions from the plasma edge.

These comparisons show that, when there is sufficient E×B Doppler shift, the fluctuation measurements by PCI are consistent with the ITG turbulence, as expected for H-Mode plasmas before the ITB formation. The higher wavenumber part of the core turbulence is shifted toward higher frequencies by Doppler shift and is separated from the edge fluctuations. Under this circumstance, the measured fluctuation spectrum in the higher frequency band (above 300 kHz in the H-Mode plasma before the ITB formation) is dominated by core fluctuations and agrees with simulations. However, when the E×B Doppler shift is reduced, as in the ITB plasma, the core and edge turbulence overlaps. Consequently, although simulation in the core predicts weaker fluctuation intensity than the experimental measurements, the latter could be intensified by significant contribution from the plasma edge and it may well dominate the longer wavelength spectrum ($k_\theta \rho_s < 1$).

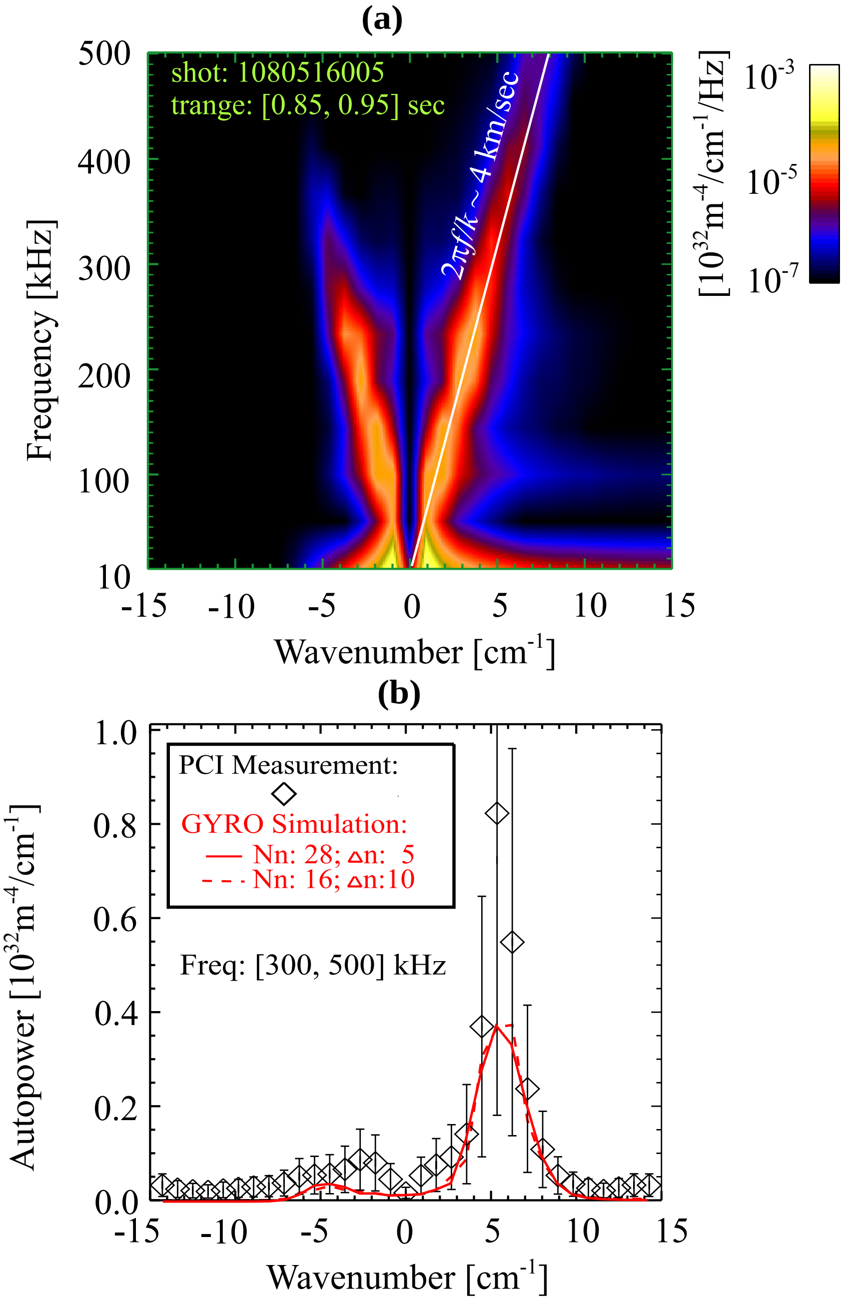

Figure 6-21: (a) Synthetic PCI frequency/wavenumber spectra in the H-Mode plasma before the ITB formation. A system response function has been implemented to emulate the top view configuration of the masked phase plate. (b) Comparison of the synthetic and experimental PCI wavenumber spectra integrated in the frequency range of 300-500 kHz.

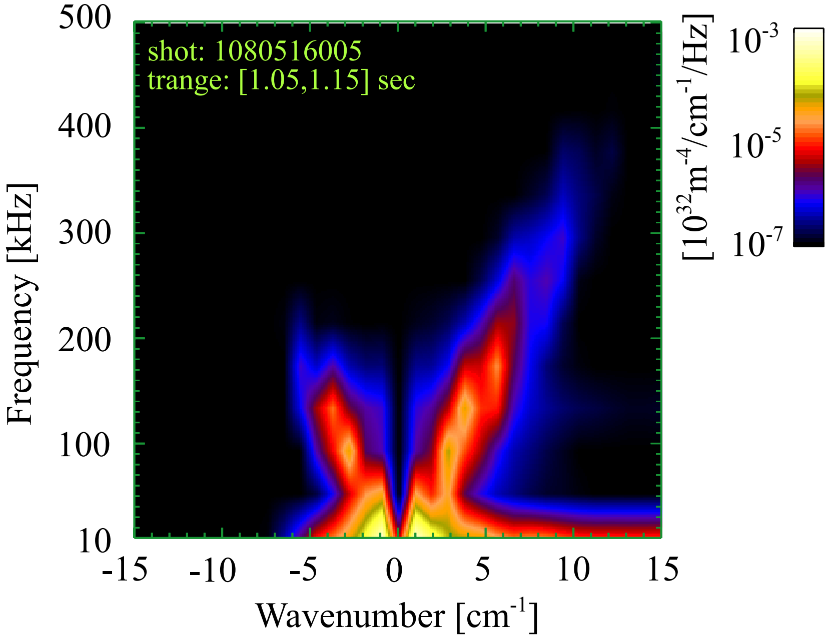

Figure 6-22: Synthetic PCI frequency/wavenumber spectra in the ITB with only off-axis ICRF heating.

6.6 Conclusions

In this chapter, we have presented studies of turbulence and transport in the Alcator C-Mod H-Mode plasmas. The studies have included both experimental measurements of turbulence with the upgraded PCI diagnostic and numerical simulations of turbulence and transport with GYRO. Good agreement is obtained in the thermal transport between code simulations and experiments after reducing the measured ion temperature gradient by ~15% and/or adding the E×B shear suppression, all within the experimental uncertainty. We have also compared the simulated level of turbulence from GYRO with the experimental measurements through a synthetic PCI diagnostic. The simulated fluctuations agree with experimental measurements. Before the ITB formation, the fluctuations above 300 kHz are measured to be core-localized (r/a<0.85) and agree with the ITG spectrum in nonlinear GYRO simulations, including the direction of propagation, wavenumber spectrum, and absolute intensity, all within an experimental uncertainty. The fluctuation below 300 kHz is dominated by the edge turbulence and shows stronger fluctuation intensity than the GYRO simulation of the core. After the ITB formation, the reduced E×B Doppler shift causes a downshift of the core turbulence in frequency, which makes the core turbulence and edge turbulence spectrum overlaps on the PCI. Consequently, GYRO simulation in the core shows overall weaker fluctuation intensity than experiments which also include contributions from the plasma edge, which may well dominate at sufficiently low frequencies.

Chapter 7

Experimental Studies of Coherent MHD Modes

In addition to the broadband drift-wave type of turbulence, the upgraded imaging configurations have also enhanced the capability of the phase contrast imaging (PCI) diagnostic to study the coherent MHD modes. In this chapter, we will discuss several new features of the quasi-coherent (QC) mode observed by the upgraded diagnostic which has not ever reported previously. The remainder of this chapter is organized as follows: Section 7.1 presents the measurements of damping effect of the X-point on the QC mode; Section 7.2 presents the measurements of mode coupling between the QC mode and the other MHD modes.

7.1 Damping Effect of the X-point on the QC mode

The QC mode has been studied extensively in Alcator with different diagnostics, including phase contrast imaging, reflectometer, scanning Langmuir probes, and magnetic probes.[54,118] The previous experimental studies show that the QC mode is edge-localized and propagating in the electron diamagnetic direction. In addition to the experimental studies, the QC mode has also been numerically studied with the BOUT code.[124] The numerical simulation shows that the QC is a resistive X-point mode driven unstable mainly by the magnetic curvature. The BOUT simulation also shows that the resistive X-point mode is essentially electromagnetic at the outboard midplane and transitions to the electrostatic resistive mode near the X-point.[125] The upgraded PCI diagnostic with a broadened beam allows us to experimentally study the QC mode near the X-point. In this section, the experimental measurement of the damping effect of the X-point on the QC mode is presented.

The experiments were carried out with the reverse field upper single null (USN) configuration, which has a lower L-H power threshold and allows for a wider range of the major radial position of the X-point than the typical lower single null (LSN) configuration under the normal field. The major radial position of the X-point ($R_{\text{X-point}}$) is moved toward the high field side (HFS) gradually by changing the triangularity. The magnetic configurations for the considered three plasmas are shown in Fig. 7-1, where the major radii of the X-point are 55.9 cm, 53.9 cm, and 52.1 cm, respectively.

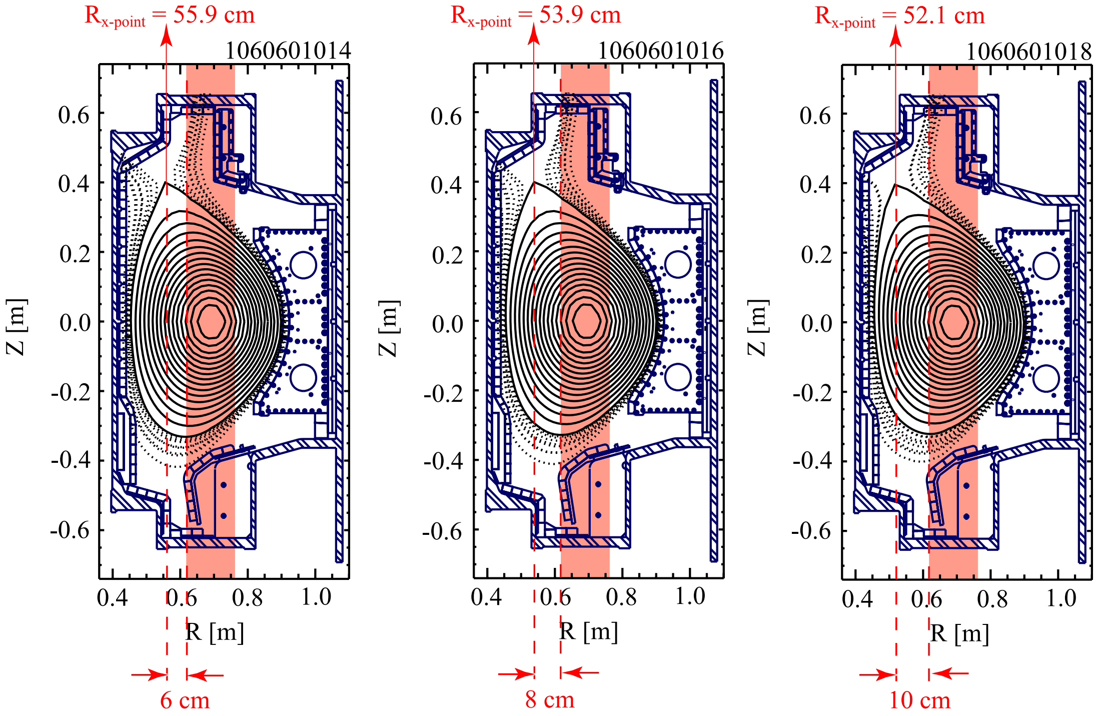

Figure 7-1: Magnetic equilibrium from EFIT for three considered plasmas, where the major radii of the X-point ($R_{\text{X-point}}$) are 55.9 cm, 53.9 cm, and 52.1 cm, respectively. The corresponding distance along the major between the X-point and the most left chord of the PCI laser beam is 6 cm, 8 cm, and 10 cm, respectively.

The PCI diagnostic is configured with the widest beam size, covering the major radius in the range of 62-72 cm. To characterize the fluctuation level of the QC mode, a normalized intensity (P_N) is defined as follows,

$$P_N \equiv \frac{1}{f_2 - f_1}\frac{2}{P(f_1)+P(f_2)}\int_{f_1}^{f_2} P(f)\,df\,, \tag{7.1}$$

where P_f is the fluctuation intensity of the frequency spectra of the PCI measurements, f_1 and f_2 are the upper-bound and lower-bound frequencies of the QC mode. Each channel of the PCI diagnostic corresponds to one major radius and the 32 channels of the PCI diagnostic are sufficient to reveal the mode structure along the major radius of the observed turbulence. The mode structure of the QC mode is shown in Fig. 7-2, where the normalized intensity P_N of the QC mode is reduced toward the X-point. Moreover, the spatial location of the intensity reduction moves with the X-point.

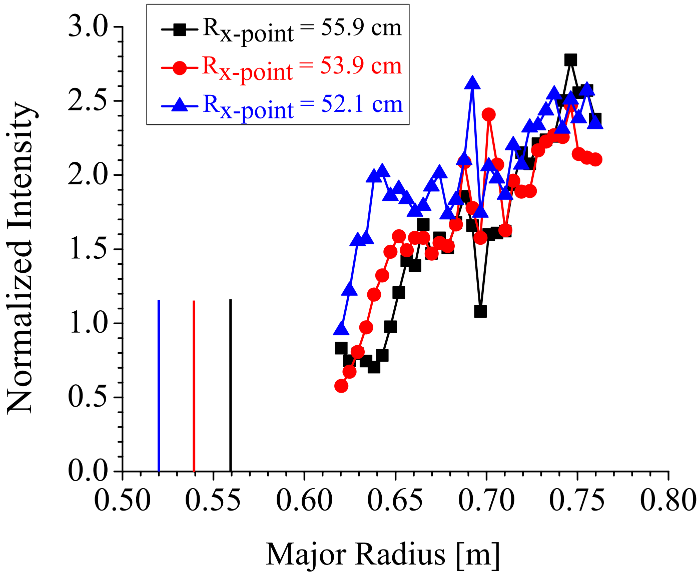

Figure 7-2: Spatial structure of the normalized intensity of the QC mode when the location of X-point moves along the major radius. The major radius coordinates of the X-point are also labeled with the vertical lines.

In addition to the damping effect of the X-point on the QC mode, the expanded beam enables the PCI diagnostic to investigate the spatial structure of the wavenumber of the QC mode. Here, 32 PCI channels are divided into 4 groups and each group contains 8 channels and corresponds to a different major radius. By performing Fourier decomposition within each group, some information of the spatial structure of the measured wavenumber can be obtained. As shown in Fig. 7-3, the wavenumber (k_R) of the QC mode increases toward the high field side (HFS). This measurement is consistent with the fact that the density fluctuations of the QC mode are field-aligned.

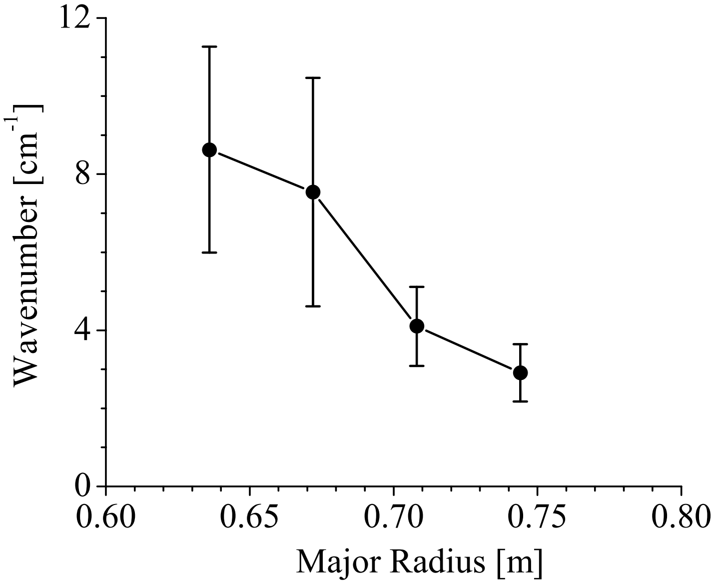

Figure 7-3: Spatial structure of wavenumber along the major radius.

7.2 Coupling between the QC mode and other MHD modes

The upgraded imaging system in the PCI diagnostic allows us to optimize the diagnostic for studying different types of turbulence with different wavenumbers. Because of the flexibility of adjusting resolvable wavenumbers, three coupled ($f_3 \sim f_1 + f_2$ and $k_{R3} \sim k_{R1} + k_{R2}$) semi-coherent modes have been detected with the medium-k setup ($k_{R\max} \sim 12\ \mathrm{cm}^{-1}$) where one coherent mode is the QC mode. Moreover, the second harmonic of the QC mode with frequency $f \sim 2f_{QC}$ and wavenumber $k_R \sim 2k_{RQC}$ is shown on the PCI measurements.

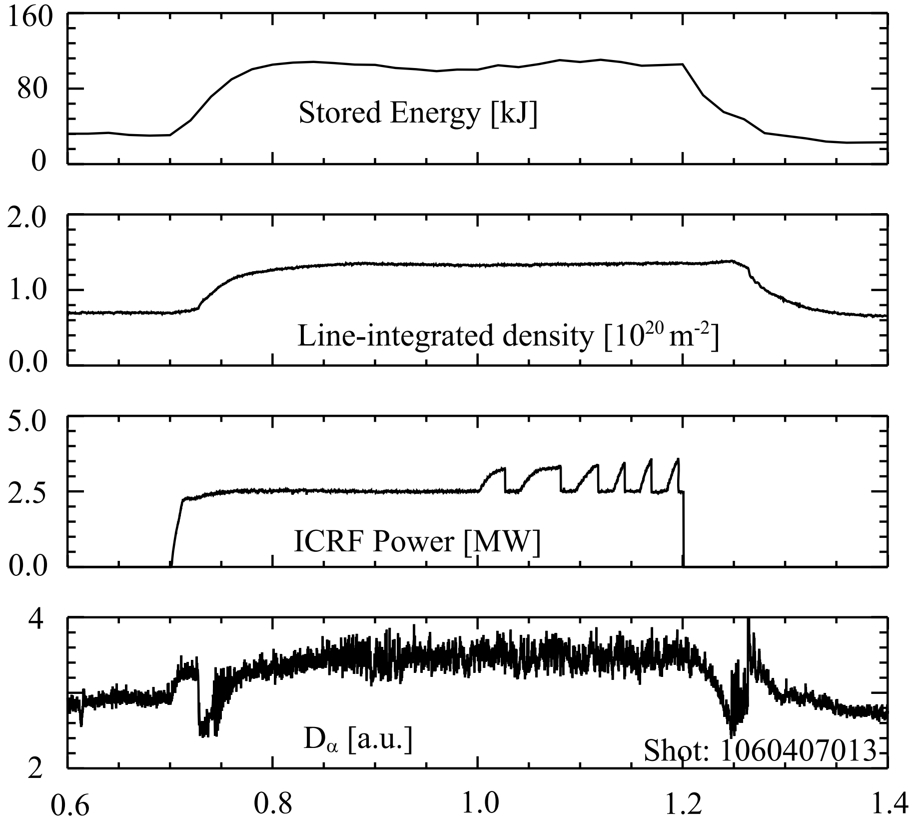

Figure 7-4: Plasma parameters for the studied discharge: (a) store energy; (b) line-integrated electron density; (d) ICRF power; (e) Dα light.

The time traces of the major plasma parameters of the considered discharge are shown in Fig. 7-4. At t=0.75 sec, the enhanced D_α H-Mode is fully developed, following application of the ICRF heating of 2.5 MW starting at t=0.7 sec. Both the density and the stored energy increase after the transition to the H-mode. The H-mode plasmas last for another 0.45 sec until the end of the ICRF heating pulse at t=1.2 sec. During the H-mode, the D_α emission is also enhanced.

The spectrogram of the measured fluctuation from the single PCI chord (channel 17) is shown in Fig. 7-5, corresponding to the plasma evolution shown in Fig. 7-4. When the EDA H-Mode develops at ~0.75 sec, the QC mode (~80 kHz) appears. The initial phase of the QC mode shows a frequency downshift from 200 kHz to 80 kHz. This frequency downshift might be due the change of the radial electric field during the L-H transition, which induces a variation of the Doppler shift in frequency and causes the change of the measured frequency. At the end of the frequency downshift at ~0.85 sec, a coherent mode at ~160 kHz appears and its frequency varies as the frequency of the QC mode varies and remains twice of the QC mode.

Besides the QC mode and its second harmonic, two other coherent modes with frequency ~530 kHz and 610 kHz also appear on the PCI measurement. The frequency difference of these two coherent modes matches the frequency of the QC mode, which indicates a mode coupling. The coherent mode at 530 kHz also shows a frequency downshift at the initial stage of the H-mode.

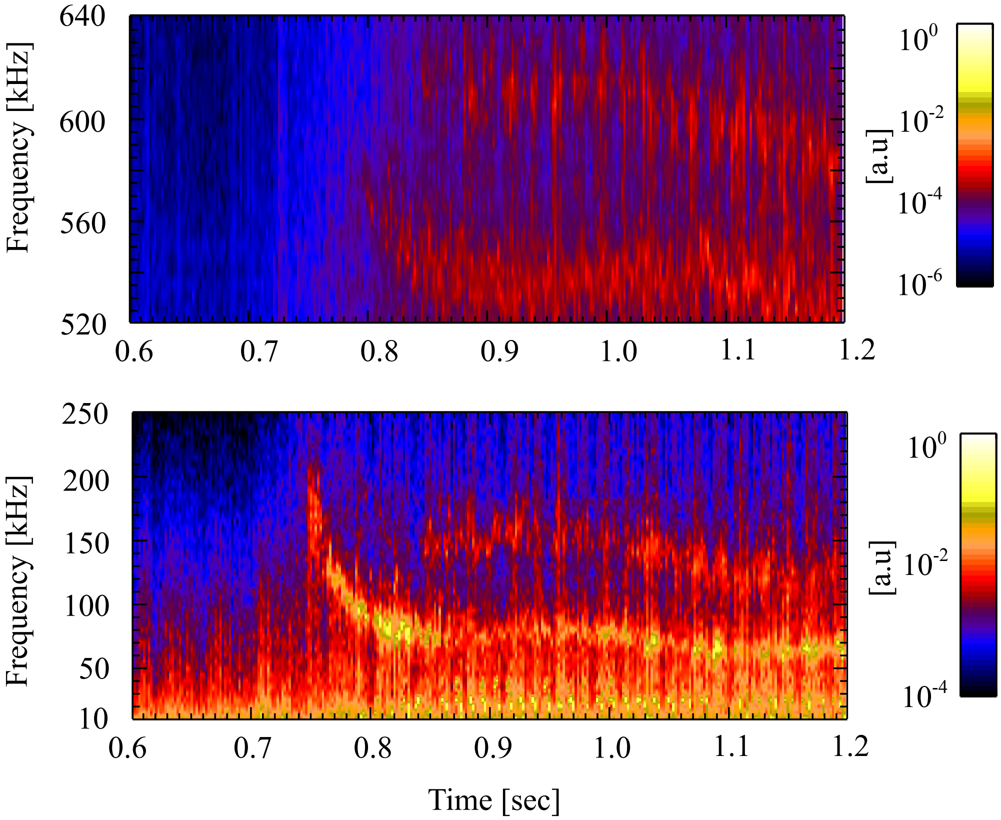

Figure 7-5: Spectrogram of a core PCI channel (17) vs. time. Time resolution is 10 ms and frequency resolution is 5 kHz. The spectrograms in the frequency range of 10-250 kHz and 520-560 kHz are shown in the different color tables so that the coherent modes are visible.

The frequency/wavenumber spectrum can be obtained through a two-dimensional Fourier transform. The spectrum is shown in Fig. 7-6, where the data is averaged over the time window 0.85-1.1 sec to reduce statistical uncertainty. Three coupled coherent modes (labeled as Mode 1, Mode 2, and Mode 3) are clearly shown on the frequency wavenumber spectrum, where the second harmonic of the QC mode is also visible and is labeled as Mode 4. To further quantify the wavenumber of these coherence modes, a Gaussian function,

$$P_{k_R} = P_0 + P\exp\left[-\frac{(k_R - k_0)^2}{2k_w^2}\right], \tag{7.2}$$

is used to fit the wavenumber spectra. The fitted peak P, center k_0, and width k_w are listed in Table 2, where the wavenumbers of three coherent modes also add up, i.e. $k_{R3} \sim k_{R1} + k_{R2}$.

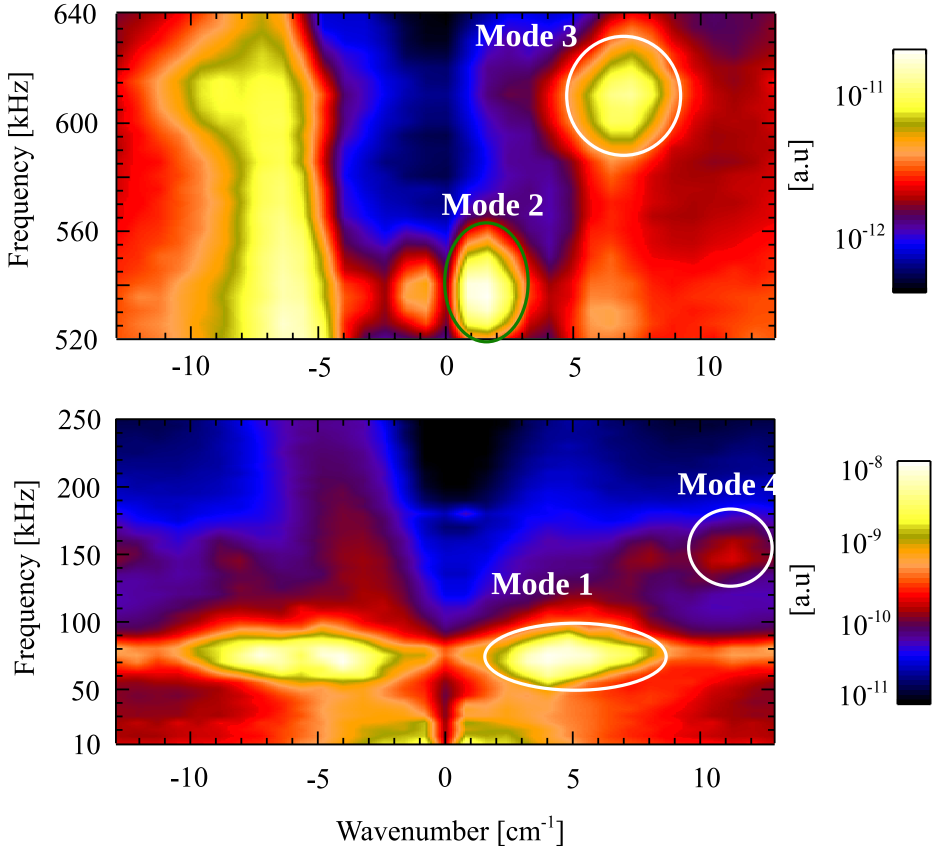

Figure 7-6: Frequency/wavenumber spectra of plasma fluctuations measured by PCI over 0.85 – 1.0 sec. The spectra in the frequency range of 10-250 kHz and 520-560 kHz are shown in the different color tables so that the coherent modes are visible.

Table 7-1: Gaussian fitting the wavenumber spectra of the coherent mode

	Freq. [kHz]	P [a.u.]	k_0 [cm^{-1}]	k_w [cm^{-1}]
Mode 1	[70, 90]	1.4×10^{-4}	4.1	1.1
Mode 2	[525, 545]	3.3×10^{-7}	1.3	0.7
Mode 3	[605, 625]	1.6×10^{-7}	6.4	0.8
Mode 4	[145, 165]	1.5×10^{-6}	10.2	0.7

7.3 Summary

In this chapter, we have discussed two new features of the edge-localized QC mode observed by the upgraded PCI diagnostic. The first feature is the damping effect of the X-point on the QC mode, where the intensity of the QC mode is reduced toward the X-point. Moreover, the spatial location of the intensity reduction moves with the X-point. The second feature is the coupling between the QC mode and other MHD modes. These new features may be useful in the future to further explore the intrinsic physics of the QC mode.

Chapter 8

Summary and Future Work

This chapter provides a brief summary of the main results of this thesis research. Some suggestions are also given for future upgrades of the phase contrast imaging (PCI) diagnostic. Finally, some possible topics of further turbulence and transport studies in Alcator C-Mod are proposed.

8.1 Summary

Extensive upgrades of the PCI diagnostic were carried out during this thesis research. The upgraded PCI system is capable of measuring density fluctuations with high temporal (2 kHz-5 MHz) and wavenumber (0.5-55 cm^{-1}) resolution. The localizing upgrade, by taking advantage of the magnetic pitch angle variation, has also enabled the PCI diagnostic to localize the short wavelength turbulence in the electron temperature gradient (ETG) range and resolve the direction of propagation (i.e., electron vs. ion diamagnetic direction) of the longer wavelength turbulence in the ion temperature gradient (ITG) and trapped electron mode (TEM) range. Moreover, the development of an improved calibration for the PCI system allows for the intensity of the observed fluctuations to be determined absolutely.

In additional to the experimental measurements with the PCI diagnostic, intensive linear stability analyses and nonlinear simulations with GYRO have been performed. The predicted fluctuations are directly and quantitatively compared against experimental measurements through a synthetic

PCI diagnostic method. The simulated thermal diffusivities are also compared with the TRANSP calculations.

Both L-Mode and H-Mode plasmas were examined through these numerical and experimental methods:

- The experiments in the L-Mode plasmas were carried out over the range of densities covering the "neo-Alcator" (linear confinement time scaling with density, electron transport dominates) to the "saturated ohmic" regime. The key role played by the ITG turbulence has been verified, including measurements of turbulent wave propagation in the ion diamagnetic direction. It is found that the intensity of the ITG turbulence increases with density, in agreement between simulation and experiment. The absolute fluctuation intensity agrees with simulation within experimental error. In the saturated ohmic regime, the simulated ion and electron thermal diffusivities also agree with experiments after varying the ion temperature gradient within experimental uncertainty. However, in the linear ohmic regime, GYRO does not agree well with experiments, showing significantly larger ion thermal transport and smaller electron thermal transport. Our study shows that although the short wavelength turbulence in the ETG range is unstable in the linear ohmic regime, the nonlinear simulation with $k_\theta \rho_s$ up to 4 does not raise the electron thermal diffusivity to the experimental level.

- The studies in H-Mode plasmas focus on plasmas before and during the internal transport barrier (ITB) formation in an enhanced Dα H-Mode plasma assisted with ion cyclotron resonance frequency (ICRF) heating. The simulated fluctuations from GYRO agree with experimental measurements in the ITG regime. GYRO also shows good agreement in thermal transport predictions with experimental measurements after reducing the ion temperature gradient (~15%) and/or adding E×B shear suppression, all within the experimental uncertainty.

Besides the drift-wave type broadband turbulence, the upgraded PCI system has also measured some new features of the quasi-coherent (QC) mode. These measurements include the damping effect of the X-point on the QC mode and the mode coupling between the QC mode and other MHD modes.

8.2 Future Work

In this section, we provide some suggestions regarding the diagnostic upgrades and research topics in turbulence and transport.

8.2.1 PCI Diagnostic Upgrade

The extensive upgrades in this thesis have greatly improved the performance of the C-Mod PCI diagnostic. Here, we give a few suggestions to further enhance the diagnostic performance.

Some hardware upgrade can be implemented on the localizing system in the C-Mod PCI diagnostic. Because of the slow rotating speed (5 RPM) of the rotatory stage used in the current C-Mod PCI localizing system, it is only possible to adjust the tilting angle of the masked phase plate to scan different parts along the chord between shots. A fast rotatory stage will allow for scanning different parts along the chord during a discharge. The DIII-D PCI localizing system uses a high speed motor (3000 RPM) designed and fabricated by Newmark Systems of Mission Viejo, CA , which can be adapted to the C-Mod PCI diagnostic.

Another limitation on the current localizing configuration is the small magnitude of the magnetic pitch angle along the vertical chord. Since the magnitude of the magnetic pitch angle along the tangential chord is at least ten times larger, one possible solution is to change the optical path and send the laser beam tangentially through the plasma.

Accurate focusing of the beam on the phase plate is essential to ensure the diagnostic performance of the PCI system. Mechanical vibrations during the plasma discharges cause some movement of the PCI probing laser beam, thereby shifting the focal spot position on the phase plate. In the current PCI configuration, the phase plate is remotely adjusted between shots so that the beam is always focused inside the central groove of the phase plate. A feedback system could be implemented as on DIII-D to automatically compensate the mechanical vibration.

8.2.2 Turbulence and Transport Studies

In this thesis research, the fluctuation measurements were obtained solely from the PCI diagnostic. Currently, there are two other fluctuation diagnostics under development on Alcator C-Mod. The correlation electron cyclone emission (CECE)[126] diagnostic detects the electron temperature fluctuations and the reflectometer[127] measures the localized density fluctuations. Future turbulence studies could also include correlation measurements between the density and temperature fluctuations.

Regarding future research topics, recent experiments on Alcator C-Mod observe strong toroidal flow and poloidal flow in D-^{3}He plasmas with ion cyclotron range of frequencies (ICRF) mode-conversion (MC) heating.[128] Initial analysis shows that this flow may be able to generate enough

E×B shear to suppress the ITG turbulence and improve the confinement. This topic can be further explored in future experiments and additional gyrokinetic simulations.

Another research topic is the anomalous electron transport, which remains poorly understood in the low-density ohmic plasmas. Currently, a more advanced gyrokinetic code (TGYRO)[129] is under development. TGYRO includes a feedback loop to obtain the steady-state profiles which give rise to particle and energy balance. TGYRO may be used to numerically explore the low-density ohmic plasmas after its release. However, more extensive and expensive ETG turbulence simulations will be necessary to more fully understand its role on electron transport under releastic experimental profiles. If necessary, the PCI system could be reconfigured to a cross-beam scattering diagnstoic to look for high-k_θ ($\gtrsim 60\ \mathrm{cm}^{-1}$) ETG modes[130-132], predicted to be linearly unstable but nonlinearly saturated at low levels.

Bibliography:

---

[1] C.M. Braams and P.E. Stott, "Nuclear Fusion: Half a Century of Magnetic Confinement Fusion Research", Institute of Physics Publishing, 1st edition, 1999.

[2] J. Wesson, "Tokamak", Oxford Science Publications, 3rd edition, 2004.

[3] http://www.ipp.mpg.de/ippcms/eng/pr/fusion21/magnet/index.html

[4] http://www.iter.org

[5] R. Goldston et al., "A plan for the development of fusion energy", J. Fusion Energy **21**, 61 (2002).

[6] ITER physics expert groups, "ITER Physics Basis", Nuclear Fusion **39**, 2137 (1999).

[7] F.L. Hinton and R.D. Hazeltine, "Theory of plasma transport in toroidal confinement systems", Rev. Mod. Phys. **48**, 239 (1976).

[8] P.W. Terry, "Validation in fusion research: Towards guidelines and best practices", Phys. Plasmas **15**, 062503 (2008)

[9] C Holland et al., "Validating simulations of core tokamak turbulence: current status and future directions", J. Phys.: Conf. Ser. **125**, 012043 (2008).

[10] http://www.psfc.mit.edu/research/alcator/index.html

[11] P.T. Bonoli et al., "Wave-particle studies in the ion cyclotron and lower hybrid ranges of frequencies in Alcator C-Mod", Fusion Sci. Technol. **51**, 401 (2007).

[12] P. N. Yushmanov, T. Takizuka, K.S. Riedel, "Scalings for tokamak energy confinement", Nucl. Fusion 30, 1999 (1990).

[13] A.J. Wootton et al., "Fluctuations and anomalous transport in tokamaks", Phys. Fluids B **2**, 2879 (1990).

[14] P.C. Liewer, "Measurements of microturbulence in tokamks and comparisons with theories of turbulence and anomalous transport", Nucl. Fusion **25**, 543 (1985).

[15] T.P. Crowley, "Rensselaer heavy ion beam probe diagnostic methods and techniques", IEEE Trans. Plasma Sci. **22**, 291 (1994).

[16] E.J. Powers, "Spectral techniques for experimental investigation of plasma diffusion due to polychromatic fluctuations", Nucl. Fusion **14,** 749 (1974).

---

[17] L.I. Rudakov and R.Z. Sagdeev, “On the instability of a nonuniform and rarefied plasma in a strong magnetic field”, Sov. Phys. Dokl. **6**, 415 (1961).

[18] B. Coppi, M. N. Rosenbluth, and R. Z. Sagdeev, “Instabilities due to temperature gradients in complex magnetic field configurations”, Phys. Fluids **10**, 582 (1967).

[19] M. Porkolab and G. S. Kino, “Observation of a new type of instability in a thermal plasma”, Phys. Rev. Lett. **15**, 752 (1965).

[20] M. Porkolab, “Plasma drift instabilities with phase velocities below the ion thermal velocity”, Physics Letters, Volume 22, Issue 4, 427 (1966).

[21] M. Porkolab, "Plasma instabilities due to ion temperature gradients", Nucl. Fusion **8**, 29 (1968).

[22] B. Coppi and F. Pegoraro, “Theory of the ubiquitous mode”, Nucl. Fusion **17**, 969 (1977).

[23] W. Horton, D. Choi, W. M. Tang, “Toroidal drift modes driven by ion pressure gradients”, Phys. Fluids **24**, 1077 (1981).

[24] B. Coppi et al., “Drift instability due to impurity ions”, Phys. Rev. Lett. **17**, 377 (1966).

[25] B. Coppi and G. Rewoldt, “New Trapped-Electron Instability”, Phys. Rev. Lett. **33**, 1329 (1974).

[26] Yi-Kang Pu, “Trapped electron modes and anomalous electron thermal energy transport”, PhD thesis, Massachusetts Institute of Technology, 1991.

[27] William Scott Daughton, “Electron diffusion in tokamaks due to electromagnetic fluctuations”, PhD thesis, Massachusetts Institute of Technology, 1998.

[28] D.R. Ernst et al., “Role of trapped electron mode turbulence in internal transport barrier control in the Alcator C-Mod Tokamak”, Phys. Plasmas **11**, 2637 (2004).

[29] D.R. Ernst, “Anatomy of toroidal drift modes”, GS2 Workshop, Princeton, January, 2003.

[30] W.M. Tang, G. Rewoldt, and L. Chen, “Microinstabilities in weak density gradient tokamak systems”, Phys. Fluids **29**, 3715 (1986).

[31] J.C. Adam, W.M. Tang, and P.H. Rutherford, “Destabilization of the trapped-electron mode by magnetic curvature drift resonances”, Phys. Fluids **19**, 561 (1976).

[32] W.M. Manheimer, “An introduction to trapped-particle instability in tokamaks”, Technical Information Center, Energy Research and Development Administration (1977).

[33] Y.R. Lin-Liu and R. L. Miller, “Upper and lower bounds of the effective trapped particle fraction in general tokamak equilibria”, Phys. Plasmas **2**, 1666 (1995).

---

[34] B.B. Kadomtsev and O.P. Pogutse, “Trapped particles in toroidal magnetic systems”, Nucl. Fusion **11**, 67 (1971).

[35] W. Horton, B.G. Hong, and W.M. Tang, “Toroidal electron temperature gradient driven drift modes”, Phys. Fluid **31**, 2971 (1988).

[36] F. Jenko and W. Dorland, "Prediction of significant tokamak turbulence at electron gyroradius sScales”, Phys. Rev. Lett. **89**, 225001 (2002).

[37] J. Candy et al., “The effect of ion-scale dynamics on electron-temperature gradient turbulence”, Plasma Phys. Control. Fusion **49**, 1209 (2007).

[38] T. Goerler and F. Jenko, “Scale separation between electron and ion thermal transport”, Phys. Rev. Lett. **100,** 185002 (2008).

[39] B. Coppi, C. Crabtree, P.H. Diamond, et al, “Interaction of drift-tearing (mesoscopic) modes with coherent and turbulent microscopic structures”, Paper TH/R2-19, Proceed. 21st International (I.A.E.A.) Conference on Fusion Energy, Chengdu, China (2006); MIT (LNS) Report HEP 06/10 (2006).

[40] B. Coppi, “Theoretical resolution of magnetic reconnection in high energy plasmas” in “Collective phenomena in macroscopic systems”, Page 59, World Scientific, 2007.

[41] C. Crabtree and B. Coppi, “Non-fluid micro-reconnecting modes and experimental observations”, ECA Vol.**32D**, P-2.023, 35th EPS Conference on Plasma Phys., Hersonissos, Crete, Greece (2008).

[42] C. Crabtree, B. Coppi, and K. Tummel, “Fluid theory of micro-reconnecting modes”, International Sherwood Fusion Theory Conference, Boulder, Colorado, USA (2008).

[43] C. Crabtree and B. Coppi, “Non-fluid micro-reconnecting mode”, Am. Phys. Soc. **53** (14), 70 (2008).

[44] F. Zernike, “Phase-contrast, a new method for microscopic observation of transparent objects: Part I”, Physica: **9**, 686, (1942).

[45] F. Zernike, “Phase-contrast, a new method for microscopic observation of transparent objects: Part II”, Physica: **9**, 974, (1942).

[46] H. Weisen, “The phase contrast method as an imaging diagnostic for plasma density fluctuations”, Rev. Sci. Instrum. **59**, 1544 (1988).

[47] H. Weisen et al., “Observation of long wavelength turbulence in the TCA Tokamak”, Plasma Phys. Control. Fusion, **28,** 1161, (1986).

---

[48] Stefano Coda, “An experimental study of turbulence by phase-contrast imaging in the DIII-D tokamak”, PhD thesis, Massachusetts Institute of Technology, 1997.

[49] Alexander Mazurenko, “Phase contrast imaging on the Alcator C-Mod tokamak”, PhD thesis, Massachusetts Institute of Technology, 2001.

[50] A. Marinoni, “Design of a tangential phase contrast imaging diagnostic for the TCV tokamak”, Rev. Sci. Instrum. **77**, 10E929 (2006).

[51] A.L. Sanin, K. Tanaka, and L.N. Vyacheslavov, “Two-dimensional phase contrast interferometer for fluctuations study on LHD”, Rev. Sci. Instrum. **75**, 3439, (2004).

[52] I.H. Hutchinson, “Principles of plasma diagnostics”, Cambridge University Press, 2nd edition, 2002.

[53] http://en.wikipedia.org/wiki/Nyquist%E2%80%93Shannon_sampling_theorem

[54] A. Mazurenko et al., “Experimental and theoretical study of quasicoherent fluctuations in enhanced Dα plasmas in the Alcator C-Mod Tokamak”, Phys. Rev. Lett. **89**, 225004 (2002).

[55] E. Nelson-Melby et al., “Experimental Observations of Mode-Converted Ion Cyclotron Waves in a Tokamak Plasma by Phase Contrast Imaging”, Phys. Rev. Lett. **90**, 155004 (2003).

[56] M. Porkolab et al., “Phase Contrast Imaging of Waves and Instabilities in High Temperature Magnetized Fusion Plasmas”, IEEE Trans. Plasma Sci. **34**, 229 (2006).

[57] N.P. Basse et al., “Characterization of core and edge turbulence in L- and enhanced Dα H-mode Alcator C-Mod plasmas*”,* Phys. Plasmas **12**, 052512 (2005).

[58] N. Tsujii et al., “Development of absolute calibration of the phase contrast imaging diagnostic and experimental tests in Alcator C-Mod”, Am. Phys. Soc. **52** (16), 215 (2007).

[59] S. Kado et al., “Improvement of the laser phase contrast method for measuring the spatial distribution of electron density fluctuations in Heliotron E”, Jpn. J. Appl. Phys. **34**, 6492 (1995).

[60] A. Truc et al., “"ALTAIR: An infrared laser scattering diagnostic on the Tore Supra tokamak”, Rev. Sci. Instrum. **63**, 3716, (1992).

[61] L. Lin et al., “Vertical localization of phase contrast imaging diagnostic in Alcator C-Mod”, Rev. Sci. Instrum. **77**, 10E918 (2006).

[62] J.R. Dorris, J.C. Rost, and M. Porkolab, “Localized measurement of short wavelength plasma fluctuations with the DIII-D phase contrast imaging diagnostic”, Rev. Sci. Instrum. to be published (2008).

---

[63] A. Fasoli et al., "Experimental characterization of drift-interchange instabilities in a simple toroidal plasma", Phys. Plasmas **13**, 055902 (2006).

[64] P.H. Rutherford and E.A. Frieman, “Drift instabilities in general magnetic field configurations”, Phys. Fluids **11**, 569 (1968).

[65] E.A. Frieman and L. Chen, “Nonlinear gyrokinetic equations for low-frequency electro-magnetic waves in general plasma equilibria”, Phys. Fluids **25**, 502 (1982).

[66] D.H. E. Dubin et al., “Nonlinear gyrokinetic equations”, Phys. Fluids **26**, 3524 (1983).

[67] W.W. Lee, “Gyrokinetic approach in particle simulation”, Phys. Fluids **26**, 556 (1983).

[68] W.W. Lee, “Gyrokinetic particle simulation model”, J. Comput. Phys. **72**, 243 (1987).

[69] T.S. Hahm, W.W. Lee, and A.J. Brizard, “Nonlinear gyrokinetic theory for finite-beta plasmas”, Phys. Fluids **31**, 1940 (1988).

[70] A.J. Brizard, “Nonlinear gyrofluid description of turbulent magnetized plasmas”, Phys. Fluids B **4**, 1213 (1992).

[71] H. Qin, W.M. Tang, and W.W. Lee, “Gyrocenter-gauge kinetic theory”, Phys. Plasmas **7**, 4433 (2000).

[72] A.J. Brizard and T.S. Hahm, “Foundations of nonlinear gyrokinetic theory”, Rev. Mod. Phys. **79**, 421 (2007).

[73] G.G. Howes et al., “Astrophyscial gyrokinetics: basic equations and linear theory”, Astrophys. J. **651**, 590 (2006).

[74] G.G. Plunk, E. Wang, and S. Cowley, “Rrevisiting Gyro-kinetics as a transport theory, I of II”, Am. Phys. Soc. **50** (8), 298 (2005).

[75] E. Wang, G.G. Plunk, and S. Cowley, “Rrevisiting Gyro-kinetics as a transport theory, II of II”, Am. Phys. Soc. **50** (8), 298 (2005).

[76] A.J. Brizard and T.S. Hahm, “Foundations of nonlinear gyrokinetic theory”, Rev. Mod. Phys. **79**, 421 (2007).

[77] G.G. Howes et al., “Astrophyscial gyrokinetics: basic equations and linear theory”, Astrophys. J. **651**, 590 (2006).

[78] F. Jenko and W. Dorland, “Nonlinear electromagnetic gyrokinetic simulations of tokamak plasmas”, Plasma Phys. Control. Fusion **43**, A141 (2001).

---

[79] F. Filbet and E. Sonnendrücker, “Comparison of Eulerian Vlasov solvers”, Comput. Phys. Commun. **150**, 247 *(*2003*)*.

[80] Z. Lin et al., “Global gyrokinetic particle simulations with kinetic electrons”, Plasma Phys. Control. Fusion **49**, B163-B172 (2007).

[81] Y. Chen and S. Parker, “Electromagnetic gyrokinetic δf particle-in-cell turbulence simulation with realistic equilibrium profiles and geometry”, J. Comput. Phys. **220**, 839 (2007).

[82] M. Kotschenreuther et al., “Quantitative predictions of tokamak energy confinement from first-principles simulations with kinetic effects”, Phys. Plasmas **2**, 2381 (1995).

[83] W. Dorland, F. Jenko, M. Kotschenreuther, and B.N. Rogers, “Electron temperature gradient Turbulence”, Phys. Rev. Lett. **85**, 5579 (2000).

[84] F. Jenko et al., “Electron temperature gradient driven turbulence”, Phys. Plasmas **7**, 1904 (2000).

[85] J. Candy and R.E. Waltz, “An Eulerian Gyrokinetic-Maxwell Solver”, J. Comput. Phys. **186**, 545 (2003).

[86] J. Candy and R. E. Waltz, “Anomalous transport scaling in the DIII-D Tokamak matched by supercomputer simulation”, Phys. Rev. Lett. **91**, 045001 (2003).

[87] http://fusion.gat.com/theory/gyro

[88] R.L. Miller et al., “Noncircular, finite aspect ratio, local equilibrium model”, Phys. Plasmas **5**, 973 (1998).

[89] R.J. Goldston et al., “New techniques for calculating heat and particle source rates due to neutral beam injection in axisymmetric tokamaks”, J. Comput. Phys. **43**, 61 (1981).

[90] D.R. Ernst et al., “Transitionless enhanced confinement and the role of radial electric field shear”, Phys. Plasmas **7**, 615 (2000).

[91] J.C. Rost et al., “Modeling and analysis of phase contrast imaging measurements”, Bull. Am. Phys. Soc. **52** (16), 334 (2007).

[92] R.R. Parker et al., “"Progress in tokamak research at MIT", Nucl. Fusion, **25**, 1127 (1985).

[93] P. Liewer, “Measurements of microturbulence in Tokamaks and comparisons with theories of turbulence and anomalous transport”, Nuclear Fusion, **25**, 543 (1985).

[94] D.L. Brower et al., “Observation of a high-density ion mode in tokamak microturbulence”, Phys. Rev. Lett. **59**, 48 (1987).

---

[95] C.L. Rettig et al., “Search for the ion temperature gradient mode in a tokamak plasma and comparison with theoretical predictions”, Phys. Plasmas **8**, 2232 (2001).

[96] K. Molvig, S.P. Hirshman, and J.C. Whitson, “Finite-βe Universal-Mode Turbulence and Alcator Scaling”, Phys. Rev. Lett. **43**, 582 (1979).

[97] B. Coppi, “Nonclassical transport and the principle of profile consistency”, Comments Plasma Phys. Cont. Fusion **5**, 261 (1980).

[98] R.R. Dominguez and R.E. Waltz, “Tokamak transport code simulations with drift wave models”, Nucl. Fusion **27**, 65 (1987).

[99] R.E. Waltz, R.R. Dominguez and F.W. Perkins, “Drift wave model tokamak ignition projections with a zero-dimensional transport code”, Nucl. Fusion **29**, 351 (1989).

[100] R.E. Waltz and R.R. Dominguez, “Note on detailed models for trapped electron transport in tokmaks”, Phys. Fluids **B 1**, 1935 (1989).

[101] R.R. Weynants et al., “Overview of radiative improved mode results on TEXTOR-94”, Nucl. Fusion **39**, 1637 (1999).

[102] M.Z. Tokar et al., “Evidence of suppression of ITG-instability in the radiatively improved mode in TEXTOR-94”, Plasma Phys. Control. Fusion **41**, L9 (1999).

[103] M.Z. Tokar et al., “Confinement mechanisms in the radiatively improved mode”, Plasma Phys. Control. Fusion **41**, B317 (1999).

[104] A. Kreter et al., “Evidence for reduction of the toroidal ITG instability in the transition from saturated to improved Ohmic confinement in the tokamak TEXTOR”, Plasma Phys. Control. Fusion **45**, 199 (2003).

[105] C. Angioni et al., “Relationship between density peaking, particle thermo-diffusion, ohmic confinement, and microinstabilities in ASDEX Upgrade L-mode plasmas” Phys. Plasmas **12**, 040701 (2005).

[106] G.D. Conway et al., “Observations on core turbulence transitions in ASDEX Upgrade using Doppler Reflectometry”, Nucl. Fusion **46**, S799 (2006).

[107] M. Greenwald et al., “Overview of the Alcator C-Mod program”, Nucl. Fusion **45,** S109 (2005).

[108] N.P. Basse et al., “Diagnostic systems on Alcator C-Mod”, Fusion Sci. Technol. **51**, 476 (2007).

---

[109] A. Ince-Cushman et al., “Preliminary results from the soft x-ray crystal spectrometer on Alcator C-Mod”, Rev. Sci. Instrum. **77**, 10F321 (2006).

[110] C.L. Fiore and R. L. Boivin, “Performance of the neutron diagnostic for Alcator C-Mod”, Rev. Sci. Instrum. **66**, 945 (1995).

[111] O. Sauter, C. Angioni and Y.R. Lin-Liu, “Neoclassical conductivity and bootstrap current formulas for general axisymmetric equilibria and arbitrary collisionality regime”, Phys. Plasmas **6**, 2834 (1999).

[112] J.E. Kinsey, R.E. Waltz, and J. Candy, “The effect of plasma shaping on turbulent transport and ExB shear quenching in nonlinear gyrokinetic simulations”, Phys. Plasma **14**, 102306 (2007).

[113] J. Candy, R.E. Waltz, M. Fahey and C. Holland, “The effect of ion-scale dynamics on electron-temperature-gradient turbulence”, Plasma Phys. Contr. Fusion **49**, 1209 (2007).

[114] R.E. Waltz, J. Candy, and M. Fahey, “Coupled ion temperature gradient and trapped electron mode to electron temperature gradient mode gyrokinetic simulations”, Phys. Plasma **14**, 056116 (2007).

[115] T. Goerler and F. Jenko, “Scale separation between electron and ion thermal transport”, Phys. Rev. Lett. **100**, 185002 (2008).

[116] D.R. Ernst et al., “Identification of TEM turbulence through direct comparison of nonlinear gyrokinetic simulations with phase contrast imaging density fluctuation measurements”, IAEA Fusion Energy Conference Chengdu, China, 16-21 October (2006), oral paper IAEA-CN-149/TH/1-3.

[117] C.L. Fiore et al., “Internal transport barriers in Alcator C-Mod”, Fusion Sci. Technol. **51**, 303 (2007).

[118] M. Greenwald et al., “Characterization of enhanced Dα high-confinement modes in Alcator C-Mod”, Phys. Plasmas **6**, 1943 (1999).

[119] J.E. Rice et al., “Double transport barrier plasmas in Alcator C-Mod”, Nucl. Fusion **42**, 510 (2002).

[120] C.L. Fiore et al., “Control of internal transport barriers on Alcator C-Mod”, Phys. of Plasmas **11**, 2480 (2004).

[121] J.W. Hughes et al., “Thomson scattering upgrades on Alcator C-Mod”, Rev. Sci. Instru., **74**, 1667 (2003).

[122] R.E. Waltz, Private communications (2008).

---

[123] C. Holland et al., “Validating simulations of core tokamak turbulence: Current status and future directions”, J. Phys.: Conf. Ser. **125**, 012043 (2008).

[124] X.Q. Xu et al., “Low-to-high confinement transition simulations in divertor geometry”, Phys. Plasmas **7**, 1951 (2000).

[125] J. Myra et al., “Resistive modes in the edge and scrape-off layer of diverted tokamaks”, Phys. Plasmas **7**, 4622 (2000).

[126] P. Phillips et al., “ECE temperature fluctuations associated with EDA H-Mode discharges in Alcator C-Mod”, Am. Phys. Soc. **51** (7), 243 (2006).

[127] A. Dominguez et al., “Density fluctuation studies using the upgraded C-Mod reflectometry system”, Am. Phys. Soc. **52** (16), 243 (2007).

[128] Y. Lin et al., “Observation of ion-cyclotron-frequency mode-conversion flow drive in Tokamak Plasmas”, Phys. Rev. Lett. **101**, 235002 (2008).

[129] J. Candy et al., “Progress on TGYRO: the steady-state gyrokinetic transport code”, Poster presented at the 21st US Transport Taskforce Workshop, 25-28 March 2008.

[130] Y. Takase et al., “Observation of parametric decay by use of CO2 laser scattering from a plasma””, Phys. Rev. Lett. **53**, 274 (1984).

[131] R. L. Watterson et al., “Spectrum and propagation of lower-hybrid waves in a tokamak plasma”, Physics of Fluids **28**, 2622 (1985).

[132] Y. Takase et al., “Observation of parametric instabilities in the lower-hybrid range of frequencies in the high-density tokamak”, Physics of Fluids **28**, 983 (1985).